Droplet Impact and the Transition to Splashing

Benjamin David Fudge

Wadham College

University of Oxford

A thesis submitted for the degree of

Doctor of Philosophy

Michaelmas 2022

Acknowledgements

First of all I would like to thank my supervisors Professor Alfonso Castrejón-Pita and Professor Radu Cimpeanu for their support and guidance over the many years. From the first summer internship offer eight years ago I could not have imagined being where I am now. It has been a privilege and honour to work with you both. I would also like to thank Professor Rafa Castrejón-Pita and Professor Arnaud Antkowiak for their collaborations which have greatly enhanced the work here and my PhD experience overall. Also I express my most sincere gratitude to all of the support staff at Oxford for making the work we do possible.

I would like to thank all of the Oxford Fluids Lab members for their companionship over the years, especially Tom for the collaborations in the lab and Jack for repeatedly coming into my office demanding some theory which did eventually come.

Spending eight years in Oxford is a long time but thankfully was spent with the best of people. I would especially thank Marcelo and Georgiana for their endless friendship over the years and for all of the adventures we have been on. I would also like to thank Joe for his endless wisdom even when used to beat me in Magic for months in a row and James for the many games of squash we played together. To Andrei for the peculiar outings around Oxford in the middle of the night or Cristi for your infectious enthusiasm for the most varied of reasons I am grateful.

Finally, and most importantly, I would like to thank my family for their endless, unconditional and unwavering support from the very first day to now and onwards. And of course to Andreea for always being by my side.

Abstract

Droplet impact onto a variety of surfaces is a familiar everyday experience: from a dripping tap to spray painting or droplets ejected during a sneeze. An underappreciated question, but often of great importance, is what happens to the droplet after impacting a surface, be it solid or another liquid. For sufficiently high speed impacts the droplet can break up into several smaller droplets in what we define as a splash. In the case of impact onto a liquid pool the pool itself can be sufficiently deformed such that it breaks up into droplets meaning there could be a splash originating from either droplet or pool.

Whether or not a droplet impact results in a splash is often a consequence of the very early time dynamics. What happens in these earliest times is of great importance to understanding and potentially even predicting the outcome of the impact. Whilst some insights have been found for the case of impact onto smooth flat solids the dynamics are much more intricate in the more complex cases considered here.

In this thesis we investigate the early time dynamics of droplet impact onto liquid pools, curved solids, and liquid films floating on pools using a combination of high speed imaging experiments, high resolution direct numerical simulations, and mathematical modelling. First we analyse the early time motion of the common interface between an impacting droplet and a liquid pool. Building upon previous results that only considered the case of identical liquids to a general multi-fluid case we find an explicit equation for the speed of the interface. Furthermore, we extend this to the case of a floating film on top of a deep pool, investigating the motion of both the upper droplet-film interface and the lower film-pool interface.

We then investigate the variation of the threshold to splash in two different cases. The first case is the impact of a droplet onto a deep immiscible viscous pool to examine how the splashing threshold depends on the pool viscosity. We identify two different regimes where the splashing threshold shows a different variation with the pool viscosity. Applying the earlier result (penetration speed) we explain the observations and derive an equation for the splashing threshold in the case of high pool viscosity, as well as the composition of the splashed liquid. Finally we investigate the impact of a droplet onto both concave and convex curved surfaces, finding a consistent change in the splashing threshold for both cases, and explaining these results in the context of recent theoretical models.

Contents

1 Introduction

Contents

1.1 Droplet Impact

Droplet impact is a phenomenon that can be experienced in everyday life such as a dripping tap or rainfall hitting the road, but despite its ubiquity its importance is often overlooked. Impacting droplets can spread diseases, both in plants and humans [1–3], affect the quality of an inkjet print [4–6], spread oil droplets from oil spills [7] or even provide clues at crime scenes [8]. Early research into droplet impact started with Worthington in the second half of the 19th century [9]. By synchronising a falling droplet with a marble, Worthington was able to produce a flash at the time of impact, akin to a modern stroboscope. This allowed sketches to be made of the impact dynamics, although modern reproductions have produced different results [6], with these as well as Worthington's images shown in Fig. 1.1 taken from Josserand and Thoroddsen (2016) [6]. The next big development in experimental research into droplet impact happened in the 1950s, when Edgerton

produced iconic high speed images of droplets impacting onto pools of milk showing the crown of liquid created during the impact [10]. Since then the power of high speed imaging has continuously improved [11] allowing images to be captured at hundreds of thousands if not millions of frames per seconds at sub micron resolution, enabling more detailed investigation than ever before.

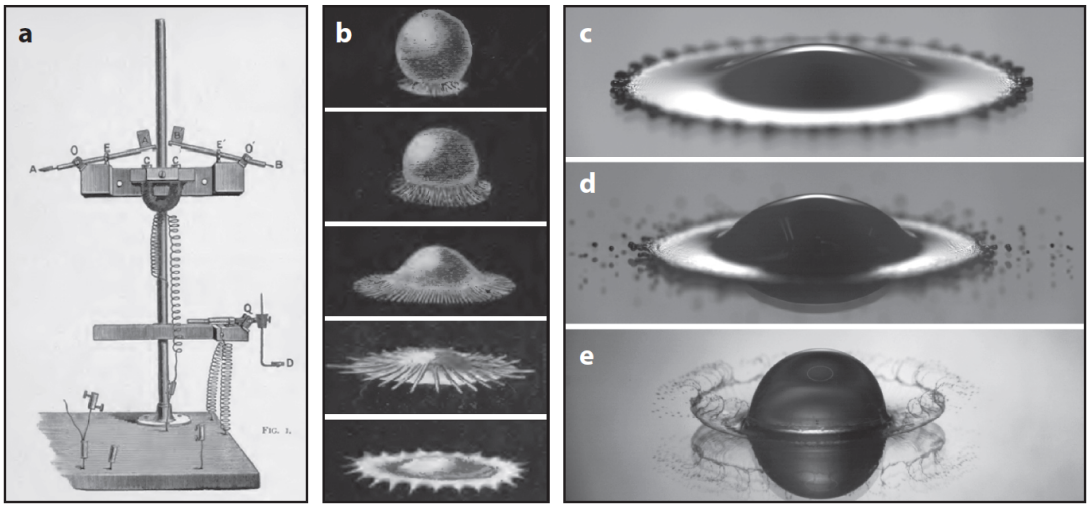

Figure 1.1: (a) Sketch of Worthington's apparatus for his droplet impact experiments and (b) Worthington's sketches of the results of the impact of mercury droplets onto a solid surface. (c) Modern reproduction of Worthington's experiment captured with a high speed camera. (d) Prompt splashing observed for the impact of a mercury droplet onto a superhydrophobic glass surface and (e) Corona splashing observed for the impact of an ethanol droplet on glass. Source: Josserand and Thoroddsen (2016) [6].

We can consider droplet impact onto several different types of surfaces, such as rough solids [12, 13], flexible cantilevers [14–17], inclined surfaces [18–20], curved surfaces [21–24], soft solids [25–27], deep pools [28–34], thin films [35, 36] or floating layers [7, 37–39]. These different impact scenarios can result in a plethora of different phenomena such as upwards Rayleigh jets [28–30], deep craters [31–34], liquid sheets [40–45], entrapped air bubbles [46–48] or microbubbles [45, 49, 50]. Each of these can depend on a variety of different parameters of both the impacting droplet such as diameter, speed, viscosity, obliqueness and the impacted surface such as stiffness or roughness for a solid surface or viscosity, depth or miscibility for a liquid surface. The main underlying questions about droplet impact addressed in many of these investigations include:

- What is the maximum spreading distance of the impacting droplet?
- What is the maximum crater depth during impact onto a liquid pool and what happens to this crater?
- Is there an entrapped air bubble beneath the impacting droplet and what is its volume?
- Does a jet form and in a multiple fluid case what is the composition of the jet?
- What is the motion of the common interface between an impacting droplet and liquid pool?
- Does the impact result in a splash and if so what are the distribution of sizes and speeds of the ejected droplets?
- What parameters do all of these phenomena depend on?

The task of answering all of these questions has been the focus of the research community for many years, with Josserand and Thoroddsen [6] providing a good summary of the research into some of these questions and more. In this work we will focus on how varying the impacted substrate properties (solid and liquid) such as the viscosity of a liquid pool or curvature of a solid surface affects the outcome of the drop impact, with the next section addressing in detail which of these questions we will attempt to answer.

1.2 Thesis Goal and Outline

The aim of this work is to explore the impact of droplets onto various substrates and to investigate how the properties of the substrate affect the impact dynamics and subsequent outcome. We will specifically investigate two different phenomena, the motion of the common interface between an impacting droplet and the liquid pool or film being impacted (presented in chapters 3 and 6) and whether the impact results in a splash (presented in chapters 4 and 5). It is presented as an integrated thesis as the main content is found in the form of publications.

Chapter 2 contains a review of the literature concerning droplet impact phenomena, focusing largely on the work that has been performed into the splashing threshold and how it can be varied (such as by surface roughness, ambient air pressure or substrate stiffness for example). We also present an overview of the literature on computational fluid dynamics (CFD) methods used to investigate these and other fluids problems.

Chapter 3 then presents the first paper, *Dipping into a new pool: the interface dynamics of drops impacting onto a different liquid*, where we investigate the speed of the common interface between a droplet and the deep immiscible pool of another liquid being impacted. Previously in this area for the impact of a droplet onto a pool of the same fluid, it has been considered that the common interface will move at half the impacting droplet speed [46, 47, 51, 52] and this result has been used elsewhere, in the context of impact onto soft solids for example [25, 53]. In this paper however for the first time we systematically investigate how this penetration velocity varies in the case of different droplet and pool fluids, specifically how the ratios of the pool to droplet density and viscosity affect this speed. We utilize both experiments and numerical simulations to vary both the density and viscosity ratios by an order of magnitude, and perform theoretical modelling via energy balance arguments in order to find an equation for the penetration velocity. We then validate with our data and further contextualise into the body of literature relevant to this topic in view of notable distinguished limits.

We follow this up in chapter 4 with the second paper, *Drop splashing after impact onto immiscible pools of different viscosities*, where we investigate the impact of a droplet onto a deep immiscible viscous pool and quantify how the splashing threshold varies with the pool viscosity across six orders of magnitude in the pool viscosity. Our results show that there is actually a non-monotonic relationship in the splashing threshold - it increases for small pool to droplet viscosity ratios ($\mu_p/\mu_d \lesssim 35$) and decreases thereafter. Interestingly, we in fact find a viscosity ratio for which we are unable to achieve splashing in either the laboratory experiments or the numerical simulations. Our results show how the composition of the splash

varies with the pool viscosity, where it is largely from the pool in the low viscosity cases and from the droplet in the high. We complement this with a quantitative investigation into the ejected jet composition, confirming our results as well as previous explorations in specific parameter regime subsets found in the literature. In the final part of this manuscript we use the results for the penetration velocity of the previous chapter to model the cushioning effect the viscous pool has on the impacting droplet. This enables us to explain the reduction in the splashing threshold observed at high pool viscosities, and thus provide an equation for the splashing threshold in excellent agreement with the experimental results.

In chapter 5 we continue to investigate droplet splashing phenomena with the paper *Droplet Splashing on Curved Substrates*. Here we study droplet impact onto both convex and concave surfaces, and how the curvature of these surfaces affects the splashing threshold. We find that for convex surfaces by increasing the curvature (i.e. impacting onto a smaller sphere) the splashing threshold increases whereas for concave surfaces the reverse is true (i.e. more curved lenses enhance splashing). We explain these results by using recent theory on the splashing threshold [54], which includes greater effects of the surrounding air. From this we model how the curvature of the substrate affects the lift force of the spreading lamella and thus its tendency to splash, resulting in a modified splashing parameter for curved surfaces. Finally we also investigate the effect of non-axisymmetry in impact on curved surfaces and how this can affect the splashing dynamics resulting in a spatial distribution of the splash.

For the final paper in chapter 6, *Drop impact onto immiscible films floating on deep pools*, we return to the topic of the penetration velocity, examining the impact of a droplet onto an immiscible film floating on a deep pool of the same fluid as the droplet. This scenario is of particular importance in real world applications where, for example, raindrops impacting an oil slick at sea can enhance the spread of the oil [7]. Here we investigate how the penetration velocity of both the upper drop-film interface as well as the lower film-pool interface vary with the film thickness. We expect limiting cases as the film thickness tends to zero, where it should behave as if it were a single fluid case, and as the thickness tends to infinity, where the

film itself should behave as a deep pool. Our results show how we can observe both an increasing or decreasing trend in the penetration velocity with the film thickness depending on the aforementioned limiting cases. We also find a limiting film thickness above which there is no further change in the penetration speed observed. We observe some deviation in the expected result for low film viscosities which we attribute to interactions between the upper and lower interfaces of the film. Finally we also investigate the motion of the lower film-pool interface and how its motion varies with both the film thickness as well as the film viscosity which we attribute to the delay in the impact motion being transferred through the film.

Finally in the last chapter we summarise all the results elaborated upon in this work, and the resulting main insights. We also identify future research avenues which can build upon the results here, and identify some of the unanswered questions that can inspire further work.

1.3 Publications

This work contains the following four papers:

- Fudge, B.D., Cimpeanu, R. and Castrejón-Pita, A.A. *"Dipping into a new pool: the interface dynamics of drops. impacting onto a different liquid"*. Physical Review E 104.6 (2021): 065102. Available at `https://journals.aps.org/pre/abstract/10.1103/PhysRevE.104.065102`
- Fudge, B.D., Cimpeanu, R., Antkowiak, A., Castrejón-Pita, J.R. and Castrejón-Pita, A.A. *"Drop splashing after impact onto immiscible pools of different viscosities"*. Published in revised format in Journal of Colloid and Interface Science 641 (2023): 585-594. Available at `https://www.sciencedirect.com/science/article/pii/S0021979723003995`
- Sykes, T.C., Fudge, B.D., Quetzeri-Santiago, M.A., Castrejón-Pita, J.R. and Castrejón-Pita, A.A. *"Droplet Splashing on Curved Substrates"*. Journal of Colloid and Interface Science 615 (2022): 227-235. Available at `https://www.sciencedirect.com/science/article/pii/S0021979722001564`
- Fudge, B.D., Cimpeanu, R. and Castrejón-Pita, A.A. *"Drop impact onto immiscible films floating on deep pools"*. Draft paper.

2
Literature Review

Contents

2.1 Splashing Threshold

As noted in the introduction, droplet impact can be of great importance in many applications. Specifically whether or not the impact results in a splash can be crucial. For example in the case of inkjet printing, if the impacting ink droplets splash on the substrate the print quality could be severely degraded [5]. The determination of the splashing threshold generally consists of finding the impact parameters that result in a splash (i.e. there is ejected fluid from the impacting droplet or liquid pool if there is one). The impacting droplet is characterised by its diameter D, impact velocity V_0, density ρ_d, viscosity μ_d and surface tension σ_d as demonstrated in Fig. 2.1. These parameters are combined into the non-dimensional groups of the Reynolds

number, defined as $\mathrm{Re} = \rho_\mathrm{d} \mathrm{D} \mathrm{V}_0 / \mu_\mathrm{d}$ representing the balance between inertia and viscosity, and the Weber number, defined as $\mathrm{We} = \rho_\mathrm{d} \mathrm{D} \mathrm{V}_0^2 / \sigma_\mathrm{d}$ representing the balance between inertia and surface tension. Sometimes the Ohnesorge number defined as $\mathrm{Oh} = \frac{\sqrt{\mathrm{We}}}{\mathrm{Re}} = \mu_\mathrm{d} / \sqrt{\rho_\mathrm{d} \mathrm{D} \sigma_\mathrm{d}}$ is used instead [6]. One can also include the effects of gravity, g by including the Froude number, defined as $\mathrm{Fr} = \mathrm{V}_0 / \sqrt{\mathrm{gD}}$. However for most impact problems this takes a sufficiently large value ($\gg 1$) and thus is often not of great importance [6]. The main task therefore is to find the values of these dimensionless groups (or some combination of the groups) for which splashing occurs, dependent on some parameters of the substrate such as density, viscosity or depth for a liquid pool or film or the stiffness, roughness or curvature etc. for a solid surface or other factors such as the inclination angle.

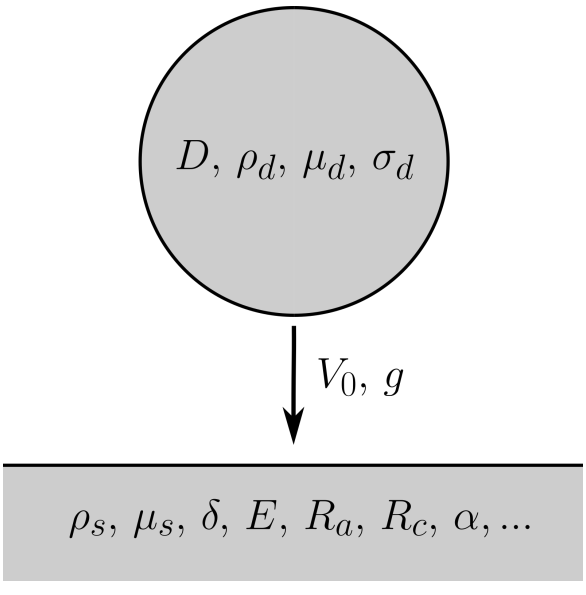

Figure 2.1: Schematic of droplet, with diameter, density, viscosity and surface tension D, ρ_d, μ_d and σ_d respectively impacting at speed V_0 accelerating due to gravity g onto a substrate. The substrate properties could include density ρ_s, viscosity μ_s or thickness δ for liquid pools or films or stiffness E, roughness R_a, radius of curvature R_c for solid surfaces at an inclination angle α.

The earliest work in this area was performed by Stow and Hadfield [12] and Mundo *et al.* [13] where they investigated the impact of droplets onto rough solid surfaces finding that the dimensionless grouping $(\mathrm{We}\sqrt{\mathrm{Re}})^\mathrm{n}$ needs to be greater than a certain threshold to splash. This dimensionless grouping is now commonly referred to as the splashing parameter [6, 18, 35, 55, 56] with the most common values of n being 1 and 1/2 (here in this work we will use $n = 1$ for splashing on viscous pools and $n = 1/2$ for splashing on spheres). Whilst these early investigations were purely experimental in nature with the splashing parameter coming from fitting to the results, there was no theoretical argument as to the underlying physical reasoning behind it. However, a theoretical

basis for the splashing parameter was later derived by Josserand and Zaleski [35], who considered how a splashing is predicated by the formation of a jet formed at the contact line, which eventually breaks up causing the splash. This was however originally derived for impact onto thin liquid films in their case. There are two competing factors: conservation of mass leading to the formation of the jet and surface tension opposing its formation. Requiring that the formation velocity from conservation of mass exceeds the Taylor-Culick retraction velocity leads to a requirement that the splashing parameter has to exceed a threshold value for splashing to occur.

Following on from these early works, several studies were performed in order to elucidate the splashing threshold for a variety of scenarios, such as introducing a tangential component of velocity by having oblique impacts [20, 57, 58] or moving surface [59]. In these cases a spatial variation in splashing could be observed where the side with a greater velocity relative to the surface, due to the additional tangential component, having an increased tendency to splash and the side with lower relative velocity less likely to splash. Other variants of splashing on solid surfaces include varying the impacting droplet properties such as through having an electric charge [60], polymer additives [61], by varying the surface properties such as its wetting properties quantified via the contact angle [62], or via the substrate stiffness [27]. In the latter case it was shown how a deformable substrate can lessen the maximum pressure at the contact area of the impacting droplet, slowing down the jet formation and thus its tendency to splash. This argument will later be extended and quantified in our work on impact onto viscous pools presented here in chapter 4. Another case of interest is the impact onto curved surfaces such as spherical particles. A significant amount of research has been conducted into finding how the maximum spreading distance of the droplet varies with the substrate curvature [63–67], although these are however generally away from the splashing regime. Some research has been conducted into finding the splashing threshold, although have presented conflicting results with some showing how the splashing threshold decreases with increasing curvature [21] (i.e. it is easier to splash

on smaller spheres) and others showing the reverse is true [24]. We do note however that in some of these cases the droplets were impacting continuously meaning that the sphere surface was not dry between each impact potentially affecting the result.

Potentially the most unexpected result was that of Xu *et al.* [68], where they discovered that the splashing threshold can be increased, and splashing even suppressed entirely, by reducing the pressure of the ambient gas, a factor that had been previously entirely overlooked. Figure 2.2 taken from Xu *et al.* (2005) [68] shows their results of the impact of ethanol droplets at constant speed onto a solid surface at varying surrounding gas pressure. For the top row at standard atmospheric pressure we can notice significant lifting off of the lamella from the surface and vigorous disintegration into droplets. For the lower pressures there is no longer any lamella liftoff and splashing only occurs at the higher pressure of 38.4 kPa and for pressures less than this there is no splashing at all. The mechanism suggested for this is that the breakup of the ejected jet causing the splash is preceded by the jet lifting upwards from the surface it is spreading over. For impact

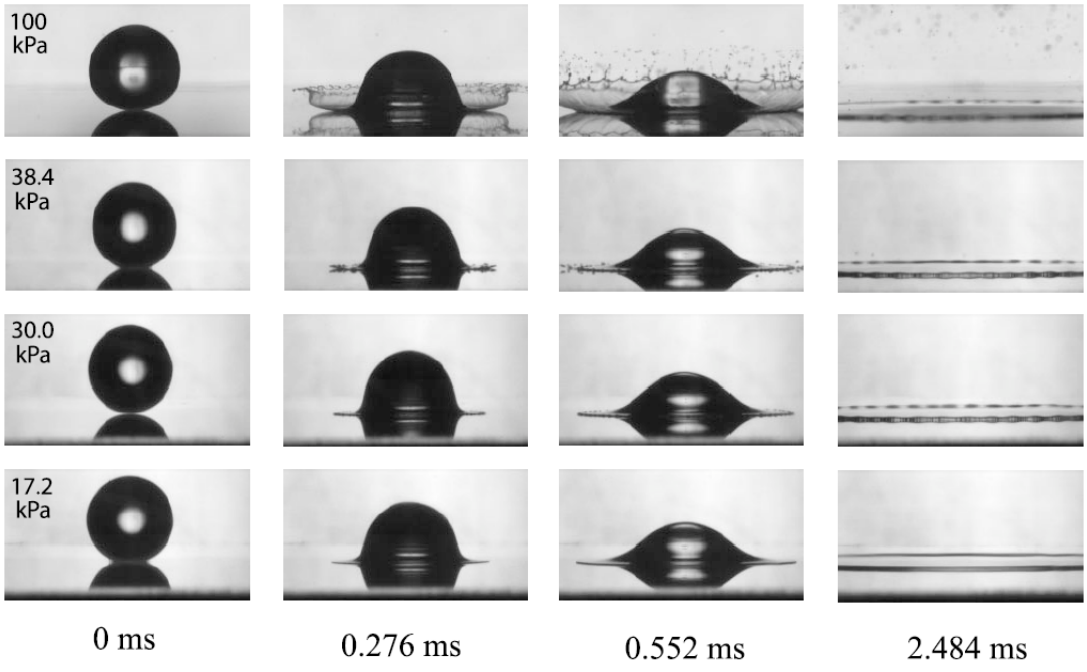

Figure 2.2: Time evolution of the impact of ethanol droplets at the same speed onto a smooth solid surface at varying gas pressure showing how the splashing can be reduced and even entirely suppressed as the pressure decreases. Source: Xu *et al.* (2005) [68].

onto another liquid this upwards motion can be caused by the displacement of the underlying fluid, but for the case of impact onto a solid surface this motion is caused by the surrounding gas. Therefore by varying the gas pressure this effect can be lessened, causing a reduction in the tendency to splash. Later theoretical work by Riboux and Gordillo [54] would greatly expand on this theory about the air motion leading to the lifting of the ejecta sheet, providing a theoretical model for the jet motion and the air's effect on it introducing a new splashing parameter including the air properties. This theory about the air having an effect on the splashing threshold will be further investigated in chapter 5, where we will examine how the surface geometry (specifically the curvature) affects the air motion and thus splashing threshold. This will enable us to resolve the conflicting results concerning splashing on spheres discussed above.

Investigation into splashing on impact onto other fluids is comparatively sparse however, especially for the case of differing fluids. One particular case of note is that of Kittel *et al.* [40], where they investigated the impact of silicone oil droplets onto thin films of silicone oils of varying viscosities. By systematically varying the viscosity ratio between the droplet and film they found that for viscosity ratios significantly different from unity the splashing threshold could be characterised by the properties of just one of the fluids. Specifically, they found that the splash was formed by the lower viscosity liquid and that by using a single splashing parameter based on the properties of the lower viscosity fluid in each case the splashing threshold could be well defined. This result was supported by the work of Marcotte *et al.* [41] where both experimentally and numerically they studied the impact of droplets onto pools of varying viscosity, finding that the formed jet consisted largely of the low viscosity fluid although the transition to splashing was not investigated therein.

2.2 Penetration Velocity

For the case of the impact of a droplet onto a solid surface the underside of the droplet deforms due to the pressure caused by the presence of the solid surface. Similarly, a solid object impacting onto a liquid pool will cause the deformation

of the pool surface. For the impact of a droplet onto a liquid pool however we would expect both the droplet and the pool to deform and their common interface (bottom of the drop and top surface of the pool) to move at a certain speed. One could consider that for limiting case of a very compliant pool (one with a low viscosity or density for example) the motion of the droplet would not be significantly affected and thus we would expect the common interface to move at the speed of the impacting droplet. Conversely, for a very non-compliant pool (one with a high viscosity or density) it will not undergo any significant motion and thus the common interface speed to be effectively zero. Consequently, we expect this common interface velocity to be somewhere between the zero and the impacting droplet speed.

The most often tackled scenario in this context is one where the impacting droplet and pool are of the same fluid. In this case intuitive arguments have been made that due to the symmetry of the problem between droplet and pool the common interface should move at half the impacting droplet speed [52]. This result was also arrived at theoretically through simple energetic balances [46, 51] with the results verified both experimentally [46, 47, 51] and numerically [69, 70]. Extension of this to cases where the droplet and pool differ are very sparse however. For the related case of impact onto soft solids the penetration velocity has been taken as half the droplet impact speeds for sufficiently soft solids and zero otherwise [53], or some smoothly varying function (although still bounded between one half and one) [25]. For the impact of a high viscosity droplet onto a pool Li *et al.* [71] found some deviation from the half impact speed value for same fluids but did not venture to find an explicit relation or model for it, noting that it would be non-trivial. Therefore there is a gap in the literature concerning the extension of the same fluid case to that of a general multi-fluid situation, which is the focus of chapter 3.

2.3 Computational Fluid Dynamics (CFD)

Alongside the development of high speed imaging techniques to experimentally explore droplet impact phenomena in greater detail, as previously expanded upon in the introduction, another key development in the research of fluid dynamics

problems has been the vast increase in computer power and the subsequent use of computational fluid dynamics (CFD) techniques to perform direct numerical simulations (DNS). The development of methodologies dedicated to multi-phase problems and the accurate tracking of the interfaces between phases in problems such as droplet impact [43, 47, 72, 73] or coalescence [74, 75] or the breakup of a liquid jet [76, 77] are of particular importance herein.

As noted in a review of the state of the art by Fuster *et al.* [78], multiphase droplet impact impact problems have several features such as "high surface tension, low viscosity, high density ratios, complex and evolving interface topologies and spatial scales ranging over several orders of magnitude", which make these simulations particularly difficult. The multiphase methods must be able to handle these difficulties in order to accurately track the interfaces between the phases to resolve the dynamics of the problem. Consequently in order to accurately provide solutions to such multiphase problems the following properties would be required:

- Robust representation of evolving, topologically complex interfaces - the case of droplet impact problems often involves coalescence and/or breakup and thus requires a method that can handle this;
- Accurate representation of surface tension, which requires accurate estimates of interface normals and curvature;
- Robust and accurate handling of large density and viscosity ratios, as a simple example a water droplet surrounded by air has a density ratio of $\sim$780 and a viscosity ratio of $\sim$55, both considerable values that need special attention;
- Efficient representation of evolving flow features of widely different characteristic spatial scales, for example millimetric size droplet impacts can result in air films on the order of micrometers.

Figure 2.3 taken from Fuster *et al.* (2009) [78] shows an example multiphase fluids simulation demonstrating these challenges. Herein an air bubble rupturing below the surface of a water pool producing an upwards jet that then breaks up into several smaller droplets. From the figure we can distinguish the large scale differences in the

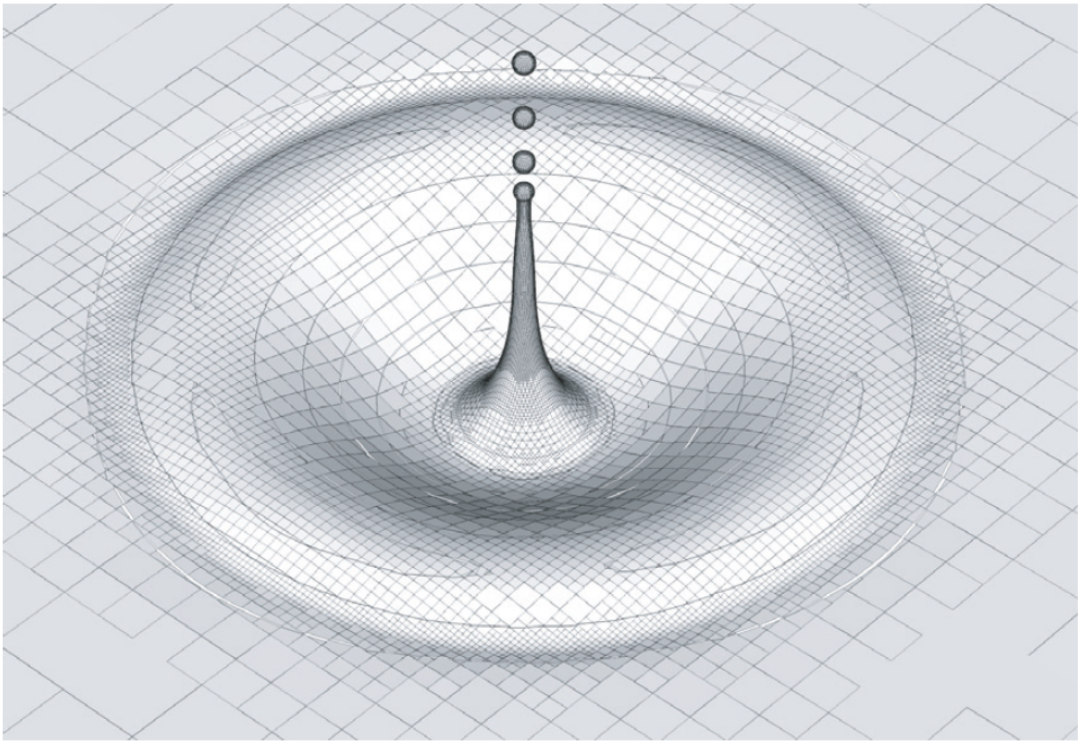

Figure 2.3: Example simulation of the jet produced by a bursting air bubble below the water surface highlighting the challenges of such multiphase flows such as large differences in resolution required, need to accurately resolve to curvature and breakup of the jet as well as the large density and viscosity ratios between the fluids. Source: Fuster *et al.* (2009) [78].

resolutions required from the flat pool surface at the edges to the thin jet tip itself. Furthermore, the breakup of the tip into droplets also needs to be carefully resolved in order to include the surface tension effects driving the breakup, as well as handling the large differences in density and viscosity between the pool and surrounding air.

2.3.1 Governing Equations

As is the case for any fluid dynamics problem the underlying governing equations are the Navier-Stokes (NS) equations as given in (2.1), where $D_{ij} \equiv (\partial_i u_j + \partial_j u_i)/2$ is the deformation stress tensor, ρ, μ and σ the density, viscosity and surface tension respectively, κ and $\mathbf{n}$ the curvature and normal vector of the interface respectively and δ_s the Dirac delta function that takes a value of 1 at the interface and 0 elsewhere such that the surface tension term only applies at the interface

and $\mathbf{F}$ is any other body force such as gravity:

$$\begin{gathered}\rho(\partial_t \mathbf{u} + \mathbf{u} \cdot \nabla \mathbf{u}) = -\nabla p + \nabla \cdot (2\mu \mathbf{D}) + \sigma \kappa \delta_s \mathbf{n} + \mathbf{F}, \\ \nabla \cdot \mathbf{u} = 0.\end{gathered} \tag{2.1}$$

For multiphase flow problems, on top of the standard fluid dynamics variables (such as pressure or velocity for example) required to solve these governing equations, an additional variable is required to distinguish the phases. For a two-phase case this can be a single scalar variable which takes a value of 1 in one of the phases and 0 in the other and a value between the two in interfacial regions [79, 80]. This extra variable (known as a volume of fluid or VoF field) then allows other properties (such as density or viscosity) to be expressed in terms of the VoF. For example if we denote the VoF variable f and the values of a variable X_1 and X_2 for phases 1 and 2 respectively, then we can express the variable as $X = fX_1 + (1 - f)X_2$. This allows us to formulate the momentum equation in the NS equations as one single equation for both phases when expressing the fluid properties in terms of this VoF variable. We then require an additional equation governing this VoF variable given by eq. (2.2), which is simply a conservation equation for the VoF field, which is a requirement that in addition to conserving the overall mass the mass of each phase must be conserved:

$$\partial_t f + \nabla \cdot (f \mathbf{u}) = 0. \tag{2.2}$$

This method can even be extended to other cases such as porous flow, where the VoF field represents the impermeability distinguishing the movable fluid from the immovable solid [81, 82].

2.3.2 Interfacial Tracking

The question then arises of how to track the interface between the two phases. One of the earliest methods is the marker method, first developed by Harlow and Welch in 1965 [83], whereby they were able to simulate dam breaking. The fluid cells inside the dam before breaking were marked, and their trajectories, and thus that of the overall fluid, were able to be tracked. One advantage of this method is

that it is able to resolve details finer than the grid resolution, as demonstrated in the thin liquid bridge shown in Fig. 2.4 taken from Scardovelli and Zaleski (1999) [79] as the marker spacing can be smaller than the cell size. This method however fails to accurately resolve the features if there is a significant difference in density or viscosity between the two phases, as the finite size of the grid will not be able to capture the varying scales in the velocity and pressure fields [79]. Another advantage of this method is that the interface can be represented by a polynomial fitted to the marker points, thus allowing accurate predictions of the interface curvature required for calculating the surface tension term as discussed above [84].

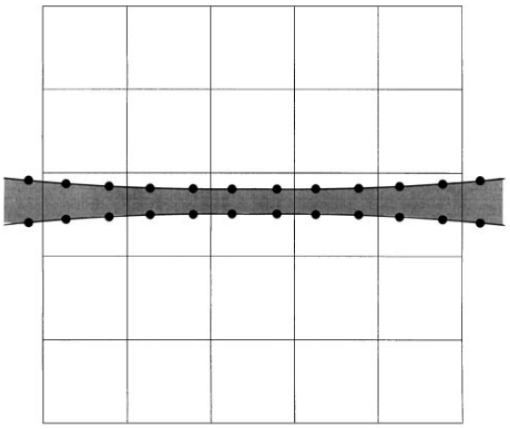

Figure 2.4: Example demonstration of a marker method of interface tracking showing how features, such as thin bridges, smaller than a grid cell in size can still be captured with this method. Source Scardovelli and Zaleski (1999) [79].

A second commonly used technique is the level set method, first introduced by Osher and Sethian [85] in 1988, whereby the interface is defined in terms of a higher dimensional function. Specifically the function finds the signed distance from each cell to the interface. This distinguishes the different phases with positive and negative values of the distance function and thus the zero value of the function corresponds to the interface position [86]. At each time step the level set function is then advected with the flow [87]. This method is advantageous as the explicit definition of the level set function allows for convenient calculation of interface curvature and normals required for implementing surface tension and topological transitions are handled naturally as they automatically evolve as the zero contour of the level set function. Figure 2.5 from Gibou *et al.* (2018) [86] shows a demonstration of this method with the level set function being the red surface and the zero plane in blue. Consequently the interface between the two phases, shown by the dark blue lines, is seen to naturally coalesce as the level set function moves downwards from left to right in the figure as time advances. The

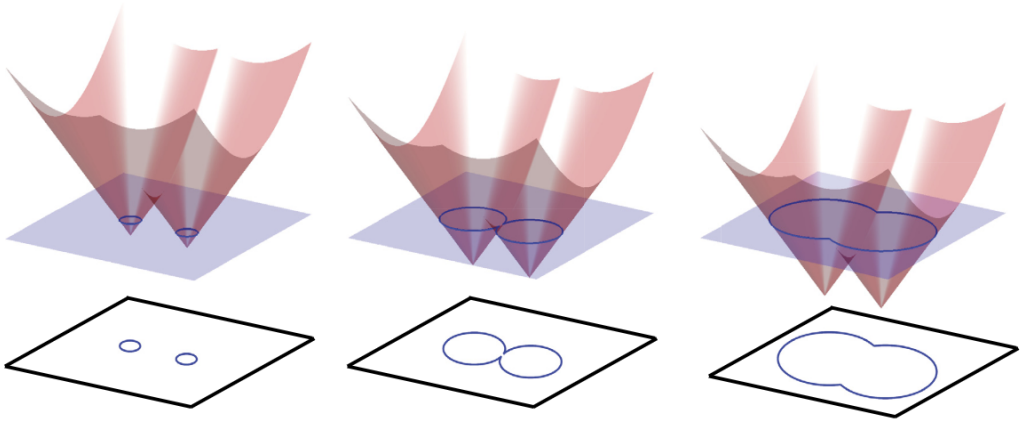

Figure 2.5: Demonstration of the level set method whereby the red surface represents the level set function with the zero plane represented in blue. Consequently the different phases correspond to the surface of the level set function above and below the blue plane with the interface being the blue contour. With the advancement of time from left to right the level set function can be seen to move down and the coalescence of the two individual interfaces occurring automatically. Source: Gibou *et al.* (2018) [86].

disadvantage of the level set method however is that, after the advection stage, the distance function needs to recalculated in each time step, therefore adding to its complexity as well as introducing errors in volume conservation [86, 87].

The final method that we will discuss here, and the one used by the Basilisk solver utilised in this work, is the VoF method. Before progressing to the detailed VoF functionality description, it is worthwhile introducing the software platform which will act as the infrastructure methodology for the respective technique used throughout the present thesis. Basilisk is an open-source partial differential equation solver [88] developed as the successor to Gerris [89, 90]. It is widely customisable and provides capability to handle numerous fluid dynamics problems, from small scale droplet impact to tsunami modelling. It has been widely adopted by the fluid dynamics research community, with many examples of papers published using the framework available on its website [91]. Fundamental studies involving multi-fluid systems with interfaces have been a particular point of strength of the package [92], which is why the package is an ideal choice in terms of implemented methodology for interfacial flow aspects, which we elaborate on further. The aforementioned VoF method is so named as it actually uses the underlying VoF field to reconstruct the

interface, and thus has the advantages of not requiring any extra fields using one that is already in use, naturally conserves mass due to the VoF field being governed by a conservation equation and naturally handles topological transitions [79]. The main task therefore of this method is how to capture the interface from the VoF field.

Figure 2.6 (a) taken from Tryggvason *et al.* (2011) [80] shows an example interface cutting through several cells as well as the values of the VoF field in each of the cells from which we reconstruct the interface. One of the simplest methods of reconstruction is the simple line interface construction (SLIC), as demonstrated in Fig. 2.6 (b) whereby the interface within each cell is represented as a straight line which is parallel to one of the cell edges [79, 80]. This has the advantage of being very simple but results in large scale jumps in the interface between cells of the order $\mathcal{O}(h)$, where h is the cell size, severely limiting its accuracy [79]. A

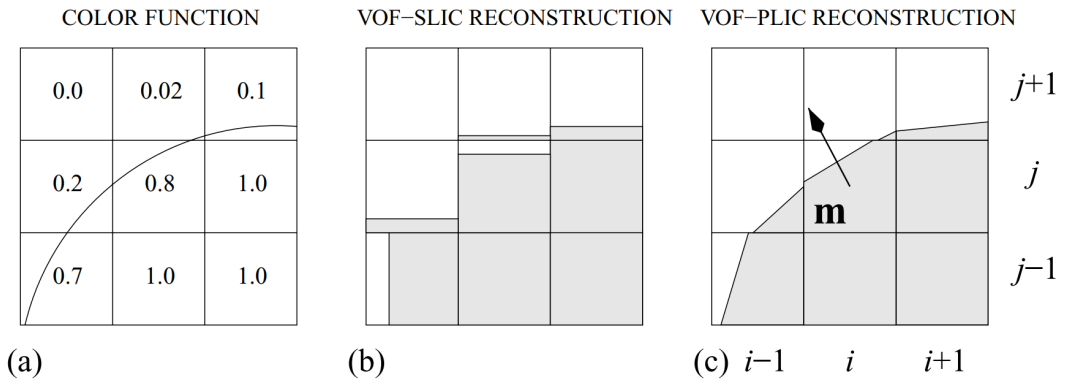

Figure 2.6: Demonstration of interface capturing methods for the VoF method. (a) The actual interface as well as the values of the VoF field in each cell. (b) Reconstruction using the simple line interface construction (SLIC) where in each cell the interface is represented by a straight line aligned with one of the cell edges and (c) Reconstruction using the piecewise linear interface construction (PLIC) where each interface section is represented by a straight line with normal direction **m**. Source: Tryggvason *et al.* (2011) [80].

second, and more accurate, method of interface reconstruction is using a piecewise linear interface construction (PLIC) [79, 80] method. In this case the interface within each grid point is still taken as a straight line segment, but can be at any orientation unlike the SLIC method as shown in Fig. 2.6 (c). Whilst in this case the interface is still not continuous between cells the errors are much smaller than

in the SLIC case and depend on the local curvature as well as the cell size [80]. This results in acceptable levels of accuracy [79, 80] whilst still being sufficiently easy to compute. Each interfacial segment is then described by the vector equation $\mathbf{m} \cdot \mathbf{x} = \alpha$ where $\mathbf{m}$ is the normal to the interface, $\mathbf{x}$ the position vector and α a scalar constant to be determined. The normal vector can be found by using finite differences to find gradients in the VoF field in the neighbouring cells [80, 93]. Once this is known the value of α can be found by geometrical considerations knowing the required volume fraction in the cell [79, 94]. After the interface is reconstructed for each interfacial cell, the VoF field is then advected in each time step by the velocity field as described in Popinet (2009) [90].

2.3.3 Spatial Discretisation and Adaptive Mesh Refinement

Another challenge of multiphase flows is the changing geometry of the configuration, for example for a single phase flow within a channel of fixed geometry the channel boundaries can be made to be higher resolution to ensure that the flow is well resolved. However for droplet impact problems there are interfaces between several different phases and/or solids (e.g. droplet-air, droplet-pool or pool-solid). Furthermore these interfaces will also be moving in time and thus one cannot know a priori where the regions of high resolution are required. The solution to this is to use adaptive mesh refinement (AMR), whereby the resolution of the grid is varied both spatially and temporally in order to focus grid points in the area of interest and thus greatly cut down on the computational cost of the simulations. Figure 2.7 taken from Popinet (2003) [89] shows an example non-uniform mesh used in Basilisk and its predecessor Gerris. Here the mesh adopts a quadtree structure in 2D (or octree in 3D) where each square (cube in 3D) cell cell can be further split into four (eight in 3D) children cells. The entire domain is taken as resolution level zero and each splitting of the cells corresponds to an increase in the resolution level by one. Consequently, and as shown in the tree diagram on the right hand side of Fig. 2.7, the example mesh consists of one level zero cell, four level one cells (the four quadrants), eight level two cells (the left half of the domain), four level three and

four level four cells. Furthermore we consider a cell to be a "leaf cell" if it does not have any higher level children, for example the two level one cells on the right side of the domain are leaves whereas the two level one calls on the left are not.

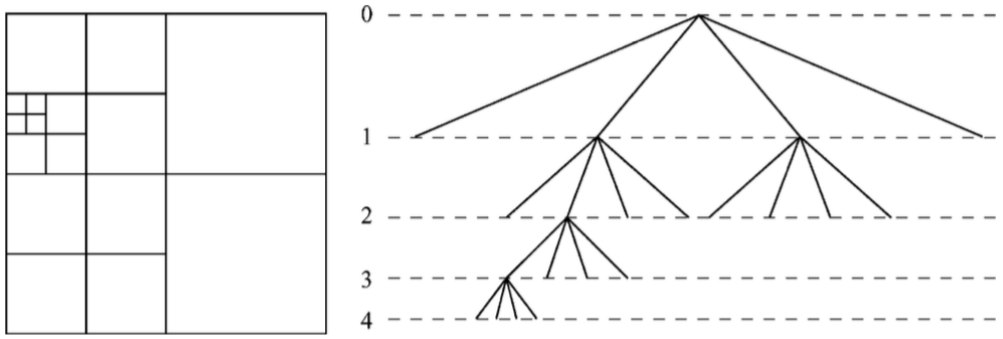

Figure 2.7: Example tree structure in Gerris/Basilisk showing the various levels of the cells (left) as well as the relationship between parent and children cells (right). Source: Popinet (2003) [89].

An advantage of the tree structure utilised here is that cells which are close in the spatial domain are also stored close together within the computer memory even when the resolution changes [95]. This allows for efficient access of data between neighbouring cells required to perform calculations such as finite differences for approximating derivatives. The quad/octree structure also allows efficient access to data of all cells for given refinement levels as well as all leaf cells [89], vital when performing operations on each level sequentially such as when adapting the mesh. Further details concerning the tree structure such as the indexing method to efficiently access neighbouring cells or extension to multiple cores can be found at [95, 96].

Now that we have shown how we are able to vary the cell resolution in space we turn our attention to how the mesh can also adapt in time. This enables us to concentrate computational effort on areas of high importance, such as at the interfaces between phases, whilst devoting fewer resources to less important areas such as the bulk of slowly moving fluids. The adaptivity process is described in detail in [89] whilst we will outline the main ideas and features behind the method here as well as some extensions to the methods used in this work. For

this process we need to identify two different groups of cells, one of under resolved cells that need to be split into children and another of over resolved cells that can have their children removed. In order to do this we require a criterion to decide whether a cell is sufficiently resolved or not. In Basilisk and Gerris this is done by selecting parameters (such as velocity or vorticity) and quantifying how the value of these parameters varies with changing resolution. This is done by successively up sampling the parameter to a higher resolution and down sampling it again and comparing it to its previous value. Further details concerning the sampling procedure to determine the error as well as the refinement method itself can be found at [97, 98]. Defining the difference between the original value and the sampled variable just described as χ, we define a maximum acceptable value of this difference, denoted as ζ. This threshold value can take different values for each parameter considered. We then subsequently refine (increase the resolution by adding four children cells) or coarsen (decrease the resolution by removing its children) for each cell according to the criteria in eq. (2.3):

$$\begin{cases} \text{refine if } \chi > \zeta, \\ \text{coarsen if } \chi < 2\zeta/3, \\ \text{no change otherwise.} \end{cases} \tag{2.3}$$

Thus it is possible for a cell to remain at its current resolution if $2\zeta/3 < \chi < \zeta$ for each considered parameter. Note that we only consider leaf cells for refinement or the parents of leaf cells for coarsening, i.e. a cell's resolution cannot change by more than one resolution level at a time. Furthermore, Basilisk allows for the definition of maximum and minimum resolutions such that a cell at the maximum level cannot be refined further and one at the minimum level cannot be coarsened. Whilst by default these maximum and minimum resolution levels are constant throughout the simulation domain, one development used here is to use an modified version of the adaptivity algorithm [99] allowing for spatial variation for these maxima and minima. The reason for this is that in certain situations we require a specific region of the domain to be at a higher resolution in order to resolve certain features such as the entrapped air bubble below an impacting droplet. Knowing where this will occur, we can therefore use the modified adaptivity method to have these regions

of interest at a higher level of resolution without having the rest of the domain at an unnecessarily high, and thus computationally inefficient, resolution level. One final modification is that we can also temporally vary the maximum resolution level, this is of great use where we know that after a certain time a higher level of resolution is no longer needed. For example whilst the initial dynamics of an impacting droplet need a sufficiently high resolution level, the later time motion is in general much less delicate and can therefore be ran at a lower resolution again saving computational effort. The combination of these various adaptivity techniques allows for much more efficient simulations producing great improvements in the number of grid points required and thus the time to run the simulations. For example if we consider a 2D simulation at a maximum resolution level of 12, a uniform grid with 2^{12} grid points in each dimension would have a total of 16,777,216 grid points, while a typical simulations using adaptive meshes has of the order of $\sim$100,000 grid points, an improvement of over a factor of 100. Consequently Basilisk allows us to perform high-resolution direct numerical simulations examining the most detailed of phenomena in a very efficient way. This enables in depth parametric investigations across several parameters of interest not otherwise feasible.

2.3.4 Three-Phase Method and Verification

Much of the work presented here pertains to the impact of droplets onto pools of another fluid, investigating how differences in the properties between the different liquids affect the outcome (the penetration velocity or splashing threshold and characteristics, for example). Consequently, this is a three-phase situation as we have the distinct droplet and pool, as well as the surrounding air requiring a three-phase setup. One approach, and the one used in the work here, is to assign a VoF field to each of the three phases [100, 101] and thus at each interface there are in fact two VoF interfaces, one from each of the phases. Consequently the interfacial tensions need to be assigned to each of the VoFs such that the overall result is correct for each interface. The solution to this is that for each of the phases i, j and k the surface tension coefficient σ_i is set to be equal to $(\sigma_{ij} + \sigma_{ik} - \sigma_{jk})/2$ where

σ_{ij} is the interfacial tension coefficient between phases i and j. From this definition we can identify that at the interface where phases i and j meet, the sum of the surface tension coefficients σ_i and σ_j is in fact equal to σ_{ij}, the required result. Furthermore we note that we now express the fluid properties in terms of all three VoF fields as an extension to that given above (i.e. we can express variable X as $X = f_1X_1 + f_2X_2 + f_3X_3$). The advantage of this method is that other than some minor checks to make sure that the three VoF field sum to unity, this implementation requires very little modification to the standard Basilisk solver. This is due to the fact that Basilisk does not make any assumptions as to the number of interfaces when applying the surface tension, and thus handles each phase automatically as long as the tensions are defined as above. Other methods exist such as using two interfaces to distinguish the three phases, however this requires careful attention of which phases are at the interface to use the correct interfacial tension [102].

With a three phase methodology in place, a key test of its validity is to verify that it correctly resolves the triple contact point and the three interfacial tensions. The most common way to carry out this test is via a liquid lens setup [43, 103], as demonstrated in Fig. 2.8 (a) whereby an initially spherical droplet is placed halfway in a liquid pool surrounded by air. Due to the effect of the interfacial tensions the droplet then deforms to assume a lens shape. By considering the three interfacial tensions at the triple contact point at equilibrium, one can form a closed triangle, called a Neumann triangle, from which the angles between the three tension forces can be found and thus the equilibrium shape [103, 104]. We note that this requires the three tensions obey the triangle inequality, otherwise the droplet can either continuously spread and wet the surface, be encapsulated in the pool or sit on top of it. Referring to the tensions and angles in Fig. 2.8 (b) for a phase i out of i, j and k the angle inside phase i is given by

$$\theta_i = \cos^{-1}\left(\frac{\sigma_{\mathrm{jk}}^2 - \sigma_{\mathrm{ij}}^2 - \sigma_{\mathrm{ik}}^2}{2\sigma_{\mathrm{ij}}\sigma_{\mathrm{ik}}}\right). \tag{2.4}$$

For the example shown in Fig. 2.8 the interfacial tensions take the values of σ_{dp}/σ_{da}=0.8 and σ_{pa}/σ_{da}=1.2 and consequently the theoretical droplet, pool and air

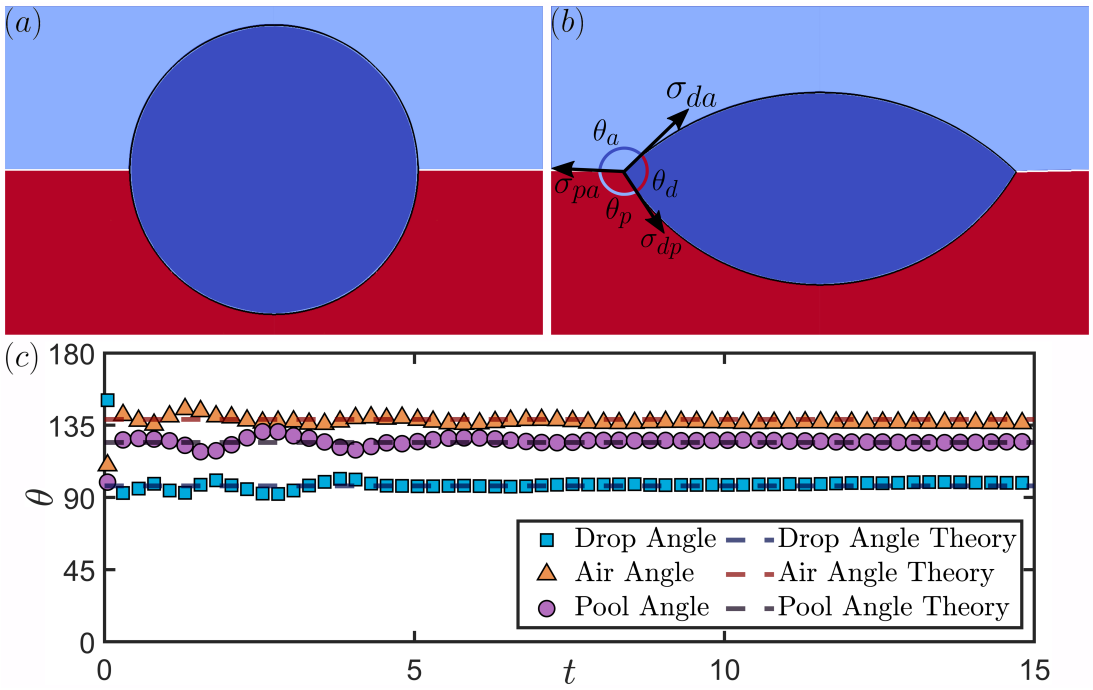

Figure 2.8: Liquid lens example showing the initial spherical droplet (a) and the steady state lens shape (b). For the case shown here the interfacial tensions are given by σ_{dp}/σ_{da}=0.8 and σ_{pa}/σ_{da}=1.2 denoted by the arrows where the subscripts d, p and a refer to the droplet, pool and air respectively. Note that the tensions are not drawn to scale. The subsequent theoretical droplet, pool and air angles as defined in the right hand image are given by θ_d=99.1°, θ_p=124.4° and θ_a=136.5° respectively whereas the simulation values are θ_d=100.7°, θ_p=122.7° and θ_a=136.1° respectively all ±0.5°, a very good agreement with a less than 2% difference at most. (c) The time evolution of the angles showing an initial transient before converging to a constant value in good agreement with the theory.

angles from (2.4) are given by $\theta_{d,\text{Theory}}$=99.1°, $\theta_{p,\text{Theory}}$=124.4° and $\theta_{a,\text{Theory}}$=136.5° respectively. Analysing the simulation results to extract the angles gives values of $\theta_{d,\text{Sim}}$=100.7°, $\theta_{p,\text{Sim}}$=122.7° and $\theta_{a,\text{Sim}}$=136.1° all values ±0.5° which is very good agreement with the theoretical values. Figure 2.8 (c) also shows the temporal evolution of the interfacial angles from which we observe initial oscillations in the angles as the droplet deforms from its initial spherical shape before converging to constant angles predicted by the theory. One potential explanation for the discrepancy could be the inclusion of gravity in the simulations, which has been shown to have an effect on the equilibrium shape [105], but is not included in the theoretical prediction. This procedure has been repeated for various combinations of interfacial tensions and has been found to be robust across a wide range of

parameters, provided that none of the angles become too close to 0° or 180°, a known limitation of the solver used here [106]. Further verification tests are performed such as finding the location of the triple contact point and comparing it to theoretical predictions [103].

We also perform a second comparison, this time between simulations and experiments, to verify the three-phase code. For this comparison we measure the spreading distance of a 1.4 mm diameter FC-770 droplet impacting onto a 1000 cSt silicone oil pool at 1.72 ms^{-1}. We note that this corresponds to a typical impact scenario seen later in chapter 4. Figure 2.9 shows the result of the comparison of the spreading distance (as defined in the inset) normalised by the impacting droplet diameter. In this case, $t = 0$ corresponds to the theoretical time of impact if neither the droplet or pool deformed and the initial gap at early time corresponds to before the droplet spreading is measurable. From the plot we can observe excellent agreement between the experiment and simulation, with the differences potentially attributable to uncertainty in the measurement of the diameter and velocity of the impacting droplet.

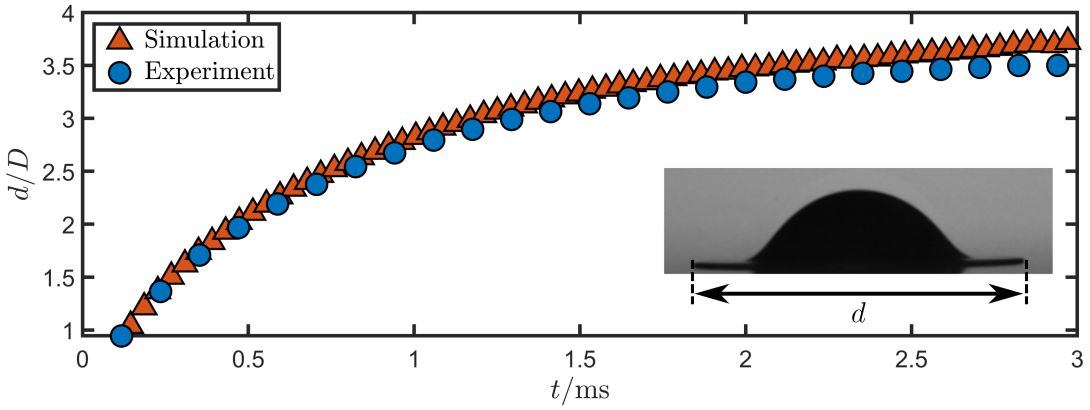

Figure 2.9: Comparison of the spreading distance between experiment and simulation for the impact of a 1.4 mm diameter FC-770 droplet onto a 1000 cSt silicone oil pool at 1.72 ms^{-1} (corresponding to Re = 3100, We = 500, Fr = 14.7) with the spreading distance as defined in the inset. Here $t = 0$ corresponds to the theoretical time of impact if neither the droplet or pool deformed. Note the dark area underneath the centre of the droplet in the inset is its reflection in the pool.

This result, combined with the above liquid lens case, provides enough confidence that our three-phase setup is able to accurately capture the dynamics in both static

and non-static cases for three-phase problems. Furthermore, it can be applied to complement our experimental campaign, as well as provide deeper understanding into aspects not achievable in the experiments.

One aspect not fully addressed here is the dynamics of the air film, particularly when it becomes very thin. We note that the maximum resolution in the work here is $\mathcal{O}(0.5\,\mu\text{m})$, whereas the mean free path of air is $\approx 70\,\text{nm}$ [107], an order of magnitude smaller. Thus we will assume that the continuous assumption of the gas flow used here is valid. Furthermore, we note that in the case of impacts onto deformable substrates, it has been shown that, due to the substrate deformability, the assumption of gas imcompressibilty also used here is valid [108, 109].

2.4 Summary of Review

This concludes the review of selected aspects of the literature produced by the research community into droplet impact and splashing over the course of the last century and a half. We have discussed the development of experimental high speed imagining techniques and how it has allowed study in greater detail than ever before into progressively more striking phenomena in fluid dynamics. Focusing specifically on the area of droplet impact and transition to splashing we have explored the first systematic investigations into the splashing threshold and the splashing parameter. This has then been extended to finding the splashing threshold in a variety of different circumstances such as soft solids, curved surfaces or thin films. For the specific area of droplet impact onto liquid pools we also examined the small amount of literature concerning the motion of the common interface between the pool and droplet, although this has been largely limited to the cases of same fluid impacts. Finally, we considered the development of computational fluid dynamics methods to perform simulations of droplet impact phenomena, focusing on the developments to deal with the specific difficulties in the area, such as tracking the interfaces between phases and the case of three-phase simulations.

3

Penetration Velocity of Droplet Impact onto a Pool of another Fluid

Contents

3.1 Introduction

In this chapter we present the paper *"Dipping into a new pool: the interface dynamics of drops impacting onto a different liquid"*, published in Physical Review E, where we investigate the motion of the common droplet-pool interface following impact. Previous work in this area has largely focused on the case of same droplet and pool fluids, but for the first time here we introduce a general multi-fluid system. Combining high speed imaging experiments with direct numerical simulations we quantify the effect of differing densities and viscosities between the droplet and pool, showing significant deviations from the half impact speed previously found for same fluid impact. In order to accurately account for differing fluid properties

between the droplet and pool in the presence of the surrounding air we implement a fully three-phase simulation setup and extensively test it.

We extend upon the simple energetic model derived for same fluid cases to a general multi-fluid formulation, taking into account the differing kinetic energies as well as the viscous dissipation in the pool. Consequently we derive an equation for the penetration velocity in terms of both the density and viscosity ratios and impacting droplet parameters. The resulting model shows very good agreement with both the experimental and numerical results as well as those previously reported in the literature.

Furthermore as part of this work, and as detailed in Appendix B, we develop a novel algorithm for tracking the common interface of the pool and droplet, accounting for any entrapped air film or bubble allowing for accurate measurement of the interfacial velocity. This tracking method proves to be robust even for cases where there is significant differences in the droplet or pool properties, causing strong displacement of the bubble into either phase. This method has been tested on and is applicable to both experimental and numerical results, and could prove to be of great use in scenarios where the (potentially unavoidable) entrapped bubbles could affect the analysis of results.

3.2 Publication: Fudge, Cimpeanu and Castrejón-Pita, *"Dipping into a new pool: the interface dynamics of drops impacting onto a different liquid"* PRE 2021

Dipping into a new pool: The interface dynamics of drops impacting onto a different liquid

Ben D. Fudge,[1,*] Radu Cimpeanu,[2,3,4,†] and Alfonso A. Castrejón-Pita[1,‡]

[1]*Department of Engineering Science, University of Oxford, OX1 3PJ Oxford, United Kingdom*
[2]*Mathematics Institute, University of Warwick, Coventry CV4 7AL, United Kingdom*
[3]*Mathematical Institute, University of Oxford, Oxford OX2 6GG, United Kingdom*
[4]*Department of Mathematics, Imperial College London, London SW7 2AZ, United Kingdom*

(Received 8 April 2021; revised 14 July 2021; accepted 16 November 2021; published 6 December 2021)

When a drop impacts onto a pool of another liquid, the common interface will move down at a well-defined speed for the first few milliseconds. While simple mechanistic models and experiments with the same fluid used for the drop and pool have predicted this speed to be half the impacting drop speed, this is only one small part in a rich and intricate behavior landscape. Factors such as viscosity and density ratios greatly affect the penetration speed. By using a combination of high-speed photography, high-resolution numerical simulations, and physical modeling, we disentangle the different roles that physical fluid properties play in determining the true value of the postimpact interfacial velocity.

DOI: 10.1103/PhysRevE.104.065102

I. INTRODUCTION

Drop impact onto a pool—of the same or a different liquid—is of great interest due to its occurrence in a wide range of natural and technological situations. Raindrop impact onto leaves [1] and oil spills in oceans [2] or paint drops onto wet coatings [3] and inkjet printed drops onto liquid layers [4,5] are just a few examples of this ubiquitous phenomenon.

Just prior to impact, the underside of the drop and the top of the pool deform as a result of pressure build-up due to the gas between these compliant surfaces. This may lead to the entrapment of a gas film or disk which either collapses into a bubble, splits up and forms bubble rings, or ruptures into microbubbles [6–8]. Nevertheless, the drop-pool interface will continue to move downwards at a well-defined velocity. This penetration velocity is crucial in estimating the volume of the entrapped bubbles postimpact onto liquid pools, films [9,10], and soft solids [11–13].

The impact of a drop onto a different liquid has been studied in the context of the contraction of the air layer caught between two different liquids [14], the formation and subsequent collapse of thin hemispherical air sheets [15] and liquid craters [16,17] on impact, splash dynamics and composition of the ejecta sheet when varying the pool's viscosity [18,19], thickness [20,21], and density [22]. A simple energetic model proposed by Tran *et al.* [9] postulates that the penetration speed is half that of the impacting drop when the drop and pool consist of the same liquid. Hendrix *et al.* [23] arrived at the same result intuitively by noting that in a liquid-liquid impact there are two deformable surfaces and thus the velocity should be halved. This was conjectured to hold for impact onto sufficiently soft substrates but that it would probably depend on the target stiffness [11,13]. While impact onto pools of different liquids is ubiquitous in nature and has been studied before in the context of splashing [19] and liquid lenses [21], the role that the liquid properties play on the penetration speed when the drop and the pool do not consist of the same liquid has not been considered in great detail before, with previous investigations [24] highlighting that the relationship would be nontrivial.

In this paper, we investigate the impact of drops onto deep pools of another liquid for a wide range of density and viscosity ratios. We apply a combination of high-speed imaging and high-resolution direct numerical simulations (DNS) to extract the speed at which the center of the drop-pool interface moves on impact.

II. EXPERIMENT

As shown in Fig. 1(a), drops are generated by a stainless steel needle by the action of syringe pump and fall under gravity and impact onto a 20-mm-deep pool below, filled with a range of liquids. These impacts are captured by two high-speed cameras in a shadowgraphy configuration. One camera (Miro 310Lab) acquires images of the impacting drop at 20 000 frames per second, from which its diameter and impact velocity are extracted. The second camera (Phantom v2512) records the deformation of the pool at 100 000 frames per second, from which the interface velocity is extracted. Different combinations of working fluids are used to achieve a range of density and viscosity ratios, as shown in Table I, where σ_a denotes the fluid-air interfacial tension. Further details on the drop-pool surface tension coefficients are provided in Sec. III. In order to concentrate on the effects of the physical property variation (in particular contrast in density and viscosity between the impacting drop and the pool), we have selected our fluids to be immiscible in both experiments

*benjamin.fudge@wadham.ox.ac.uk
†radu.cimpeanu@warwick.ac.uk
‡alfonso.castrejon-pita@wadham.ox.ac.uk

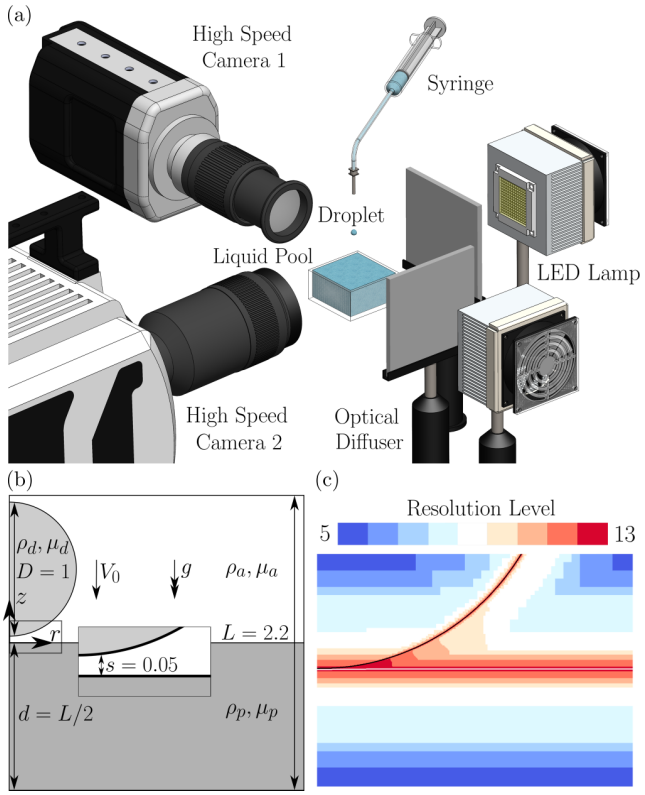

FIG. 1. (a) Diagram of the experimental setup. Two cameras observe the drop impact above and below the surface of the pool. (b) Sketch of the axisymmetric simulation domain in its initial state. (c) Zoomed-in view showing the adaptive mesh refinement, achieving spatial resolutions down to 0.5 μm.

and throughout the theoretical exploration. This preserves the sharpness and natural description of the interface location that allows us to compute the relevant metrics. The setup also remains consistent in cases when surface tension coefficients between droplet and pool are set to zero, thus reducing to same-fluid impact.

III. DIRECT NUMERICAL SIMULATIONS

High-resolution simulations are performed using the open-source software Basilisk [25–27]. Figure 1(b) illustrates the simulation setup, with a typical axisymmetric run amounting to $\mathcal{O}(10^5)$ computational cells, down to a resolution of 0.5 μm (corresponding to ∼1860 gridpoints per diameter), while making extensive use of adaptive mesh refinement and parallelization capabilities. Furthermore, as we are interested in investigating the effects of varying the properties of two different liquids in the presence of a surrounding gas, a full three-phase implementation is used. This allows us to independently vary the fluid properties while tracking the interfaces of each phase separately.

TABLE I. Properties of fluids used in the experiments.

Fluid	ρ (kg m^{-3})	μ (cP)	σ_a (mNm^{-1})
5 cSt silicone oil (SO)	916	4.6	19.7
20 cSt silicone oil (SO)	953	19.1	20.8
Water	1000	1.0	72.0
Fluorinert FC-40	1855	4.7	16.0
5 cP water-glycerol (W-G)	1053	4.9	68.9

The simulation setup itself consists of a drop of nondimensional size 1 within a domain of size 2.2, with the drop center initially 0.55 units above the pool surface (i.e., an initial separation of 0.05D). The domain size is found to be sufficiently large that the domain boundaries do not affect the simulation results, specifically the bottom boundary. The drop nondimensional density and initial velocity are both set to be 1, and the nondimensional viscosity, surface tension, and acceleration due to gravity are set to produce the correct simulation values of the Reynolds number Re_d, the Weber number We_d and the Froude number Fr_d (as defined in Sec. IV). For the particular choice of 5 cP water-glycerine solution impacting onto the Fluorinert FC-40 liquid, the interfacial tensions are $\sigma_{\mathrm{da}} = 72$ mNm^{-1}, $\sigma_{\mathrm{pa}} = 16$ mNm^{-1}, and $\sigma_{dp} = 52$ mNm^{-1}. For all other cases they are set to replicate the tension coefficients for the 5 cSt silicone oil combination namely $\sigma_{\mathrm{da}} = \sigma_{\mathrm{pa}} = 19.7$ mNm^{-1}, $\sigma_{\mathrm{dp}} = 0$ mNm^{-1}. The air and liquid pool nondimensional properties are set according to the ratios of the physical values to those of the drop. Additional detailed information on the computational framework, including the three-phase implementation, validation, and dedicated post-processing techniques, is provided in Appendix A.

IV. EXPERIMENTAL VALIDATION

A comprehensive set of runs is conducted with drop property-based dimensionless grouping definitions, namely the Reynolds number $\mathrm{Re}_d = \rho_d V_0 D/\mu_d = 52.25\text{-}1110.2$, Weber number $\mathrm{We}_d = \rho_d V_0^2 D/\sigma_{\mathrm{da}} = 3.3\text{-}53.4$, Froude number $\mathrm{Fr}_d = V_0/\sqrt{gD} = 2.7\text{-}11.4$, and the modified Ohnesorge number [10] $\mathrm{Oh}_e = \mu_d/\sqrt{\rho_d \sigma_{\mathrm{da}} e} = 0.091\text{-}3.695$, where ρ_d and μ_d denote the constant density and viscosity of the drop, respectively, V_0 its impacting velocity, D its diameter, σ_{da} the constant surface tension coefficient between the drop and the surrounding air, and e is the mean thickness of the air film, as defined in Reference [10]. Similarly, ρ_p and μ_p refer to the density and viscosity of the pool. A modified Reynolds number based on the drop density and pool viscosity $\overline{\mathrm{Re}} = \rho_d V_0 D/\mu_p = 3.27\text{-}3344$ will also become useful when modeling and describing the observed phenomena in Sec. V. The velocity of the drop-pool interface at the center of impact is denoted by V, giving the normalized penetration velocity $\bar{V} = V/V_0$. In this paper we focus on understanding the effect of varying the viscosity ratio $\mu_r = \mu_p/\mu_d$ and density ratio $\rho_r = \rho_p/\rho_d$ between the pool and the impacting drop, respectively, on the penetration velocity $\bar{V}$.

Figure 2 shows simulation and experimental snapshots for a 2.56-mm drop of a 5 cP water-glycerol solution impacting a FC-40 pool. Overlaid images for over and under the liquid surface demonstrate excellent agreement, confirming the accuracy of the three-phase numerical approach. Furthermore, we conduct a systematic comparison of numerical simulations and experiments by quantitatively investigating the temporal evolution of the interface displacement, D_p. Details of the image analysis technique utilised to account for irregularities

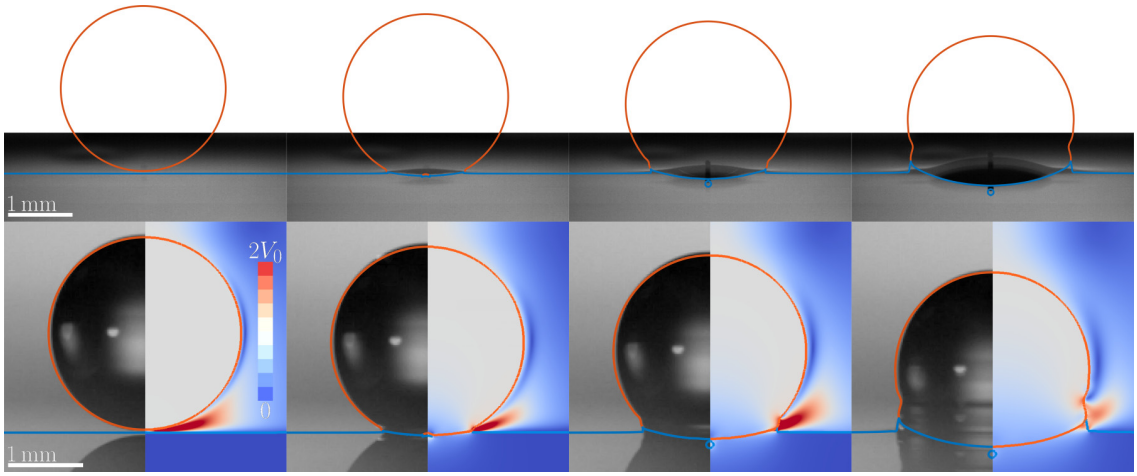

FIG. 2. Comparisons between an experiment and direct numerical simulation for a 2.56-mm diameter drop of a 5 cP water-glycerol solution impacting a FC-40 pool at 0.502 ms^{-1} with $Re_d = 274.1$ ($\overline{Re} = 285.8$), $We_d = 9.4$, $Fr_d = 3.2$ at −0.079, 0.171, 0.393, and 0.837 ms after impact from left to right corresponding to dimensionless times −0.015, 0.034, 0.078, and 0.166, respectively. Top row: View from underside of the pool surface; bottom row: left-half side, view above pool; and right-half side, simulation results showing the magnitude of the velocity field. Interface contours are extracted from the numerical data.

in the interface are presented in Appendix B. Figure 3 shows the temporal evolution of the pool depth for three different sets of experiments and simulations: (i) drop and pool are of the same liquid (5 cSt SO drop impacting on a 5 cSt SO pool, $\rho_r = 1$, $\mu_r = 1$), (ii) liquids have approximately the same density but different viscosities (20-cSt SO drop on 5 cSt SO pool, $\rho_r = 0.964$, $\mu_r = 0.24$), and (iii) liquids have approximately the same viscosity but different densities (5 cP W-G solution drop on FC-40 pool, $\rho_r = 1.762$, $\mu_r = 0.95$). For the 5 cSt SO drop onto the same liquid case we also compare our findings against experiments presented in Ref. [9] at much lower acquisition speeds. This setup enables cross-validation against state-of-the-art results, while also providing a first glimpse into multiliquid systems with substantially different properties. It readily becomes clear that varying liquid properties has a substantial effect on the penetration velocity.

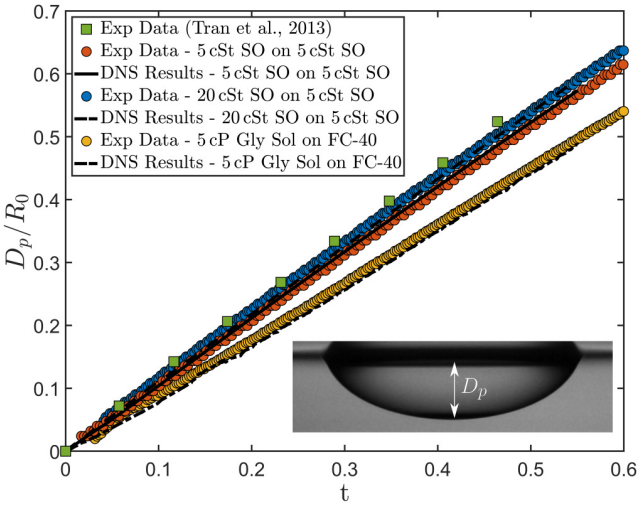

FIG. 3. Displacement of the center of the drop-pool interface for experiments and numerical simulations for three cases: ● drop and pool are of the same liquid [$Re_d = 197.7$ ($\overline{Re} = 197.7$), $We_d = 26.6$, $Fr_d = 4.5$, $\bar{V} = 0.503 \pm 0.002$], ● liquids have approximately the same density but different viscosities ($\mu_r = 0.24$ and $Re_d = 58.4$ ($\overline{Re} = 243.3$), $We_d = 29.7$, $Fr_d = 3.9$, $\bar{V} = 0.537 \pm 0.003$), and ● liquids have approximately the same viscosity but different densities ($\rho_r = 1.76$ and $Re_d = 274.1$ ($\overline{Re} = 285.8$), $We_d = 9.4$, $Fr_d = 3.2$, $\bar{V} = 0.469 \pm 0.005$). ■ represent experimental data from Ref. [9], for conditions similar to ●. Different lines show the numerical results.

V. MATHEMATICAL MODELLING

In order to better understand these effects, we develop a general model for nonmatching liquids inspired by the energy considerations first described by Tran *et al.* [9] for the case of identical drop and pool liquids. Before impact, we consider a spherical cap with density ρ_d, volume Ω, and velocity V_0, with preimpact kinetic energy given by $E^0_\Omega = \rho_d \Omega V_0^2/2$. At a time t after impact, we assume this volume takes the shape of a hemisphere of radius R_p and thus $\Omega = 2\pi R_p^3/3$ moving at the penetration velocity V, with kinetic energy $E^t_\Omega = \rho_d \Omega V^2/2$. At this time, the pool has been displaced and its motion assumed to be confined to a cylinder with radius R_p and height $2R_p$ (and hence volume 3Ω) moving at the penetration velocity V, with kinetic energy $E^t_P = 3\rho_p \Omega V^2/2$ (the same result is obtained by assuming a radial flow field in the pool [28]). Equating the preimpact (E^0_Ω) and postimpact ($E^t_\Omega + E^t_P$) kinetic energies and solving for the normalized penetration velocity we obtain the inviscid model $\bar{V} = 1/\sqrt{1+3\rho_r}$. Note that for the case $\rho_r = 1$ (i.e., drop and pool of equal density), we recover the oft used result of $\bar{V} = 1/2$ [9,10,12,13].

The viscous energy dissipation rate per unit volume in axisymmetric coordinates is given by $\epsilon_\mu(r,z) = 2\mu[(\frac{\partial V_r}{\partial r})^2 + (\frac{V_r}{r})^2 + (\frac{\partial V_z}{\partial z})^2] + \mu(\frac{\partial V_r}{\partial z} + \frac{\partial V_z}{\partial r})^2$, where V_r and V_z are the radial and axial velocities, respectively [29]. This indicates that viscous dissipation scales as $\mu V^2/D^2$, where the drop

diameter is taken as the reference length scale. The viscous dissipation in the pool (up to time t), E_μ^t, can be expressed as $\epsilon_\mu \Omega_\mu \tau$, where ϵ_μ, Ω_μ, and τ represent the viscous dissipation rate per unit volume, volume over which the viscous dissipation occurs and the characteristic time for the impact, respectively. Taking $\epsilon_\mu \sim \frac{\mu_p V^2}{D^2} = k_1 \frac{\mu_p V^2}{D^2}$, $\Omega_\mu = k_2 \Omega$, and $\tau = \frac{D}{V_0}$, where k_1 and k_2 are dimensionless constants, we can now write $E_\mu^t = \frac{C \mu_p \Omega}{2 D V_0} V^2$, where $C = 2k_1 k_2$ is a dimensionless constant. Including this term in the original energy balance results in $V_0^2 = V^2 + 3\rho_r V^2 + C \frac{\mu_p}{\rho_d D V_0} V^2$. By using Re_d and viscosity ratio, μ_r, we find the penetration velocity

$$\bar{V} = \frac{1}{\sqrt{1 + 3\rho_r + \frac{C}{\mathrm{Re}_d}\mu_r}}. \tag{1}$$

By relaxing the assumptions about the postimpact flow field and replacing the prefactor of three in front of the density ratio with another fitting parameter (denoted A), we obtain a compact two-parameter model

$$\bar{V} = \frac{1}{\sqrt{1 + A\rho_r + \frac{C}{\mathrm{Re}_d}\mu_r}}. \tag{2}$$

This leads to a simple yet versatile tool to investigate the influence that both different viscosity and density ratios play in establishing the penetration velocity. The fixed values for the constants C and A are obtained by fitting the models to our entire dataset consisting of 54 numerical results. For the one-parameter model (1), the best fit value of C is 19.1537, while for the two-parameter model (2) the values of C and A are 24.3983 and 2.7096, respectively. For the conditions explored here, a typical value for $\frac{C}{\mathrm{Re}_d}$ is ∼0.25. At first glance this seems to imply that the effect of density on the penetration velocity is significantly greater than that of viscosity. We emphasize, however, that in real-world situations viscosity ratios much larger than density ratios are often encountered: Silicone oils can span seven orders of magnitude in viscosity, whereas density ratios rarely exceed a factor of 10.

It is possible to further simplify the modeling framework by noticing that the ratio of viscosities provides useful physical insight but artificially increases the number of dimensionless groupings in expressions (1) and (2), given that the simplified model does not depend on the droplet viscosity. A natural way to address this issue is to make use of the previously defined modified Reynolds number $\overline{\mathrm{Re}} = \rho_d V_0 D/\mu_p$, where the droplet density and the pool viscosity are used instead. This leads to an expression which, beautifully, only depends on two dimensionless parameters, ρ_r and $\overline{\mathrm{Re}}$, in the form

$$\bar{V} = \frac{1}{\sqrt{1 + A\rho_r + C\overline{\mathrm{Re}}^{-1}}}, \tag{3}$$

as a counterpart to the previous two-parameter model (2).

In the subsequent discussion we will refer to models (1) and (2) in order to first isolate the individual contributions of the studied physical property ratios (density and viscosity), ultimately summarising our insight using the compact toolkit provided by the updated expression (3).

VI. DISCUSSION

Figure 4 illustrates the penetration velocity against (a) the density ratio and (b) the viscosity ratio for our simulations, experiments, and proposed models (1) and (2) alongside inviscid-theory predictions [9]. For the simulations in each case the drop properties are held constant (corresponding to a $D = 1.9$ mm 5 cSt SO drop) while V_0, and ρ_r or μ_r are varied independently. For the numerical results, the penetration velocity for each impact event represents the velocity of the interface averaged over 0.1 dimensionless time from the moment of impact and this is equivalent to ∼300 to ∼600 μs. In some cases, for both experiments and numerical simulations, the penetration speed varied slightly due to the presence of entrapped bubbles or due to the rapid collapse of the trapped air film immediately after impact; however, these disturbances were short lived and our method (fully described in Appendix B) was found to be sufficiently robust to account for these features. Also included are experimental results for different combinations of fluids, with each point obtained from averaging at least 10 impact events (error bars are smaller than the symbols in some cases).

Figure 4(a) shows the theoretical models correctly display the overall trend for the experiments and simulations. The penetration velocity decreases as ρ_r increases as the pool becomes less compliant. For density ratios less than unity the inviscid model can be interpreted as an upper limit of the theoretically predicted penetration velocities, whereas both the one- and two-parameter models (1) and (2) correctly capture the observed variations with changes in the impact velocity (and thus Re_d). This is expected, as even when we consider the pool density becoming very small, the compliance induced by the pool viscosity still plays a role. For density ratios greater than 1, both new models, as well as the inviscid model, overpredict the penetration velocity. We hypothesize that the large density of the pool in these cases significantly affects the underlying modeling assumptions of the energy balance. By inspecting simulation data for these cases we notice that the motion within the pool is confined to a small region close to the drop interface, whereas the energetic balance assumes that the volume of the pool that moves is the same for all density ratios. Future modeling could therefore focus on how the pool motion depends on its density and thus more accurately quantify the kinetic energy associated with the pool motion. Another possible direction would be to adopt a conservation of momentum approach. Preliminary work has revealed potential benefits in describing high-density-ratio cases.

For the widely reported case in the literature of same drop and pool fluids (i.e., $\rho_r = 1$, $\mu_r = 1$), our experiments, numerical data and theoretical models confirm that the normalized penetration velocity is very close to the frequently used value of 0.5 (for all considered Re_d). Our results reveal, however, that changes in the physical properties of the liquids used lead to vastly different outcomes, with penetration velocities spanning 0.1–0.9 across the wide range of fluid properties considered here.

The effect of varying the pool to drop viscosity ratio while keeping the density ratio fixed is also comprehensively investigated, with the results presented in Fig. 4(b). We find that the

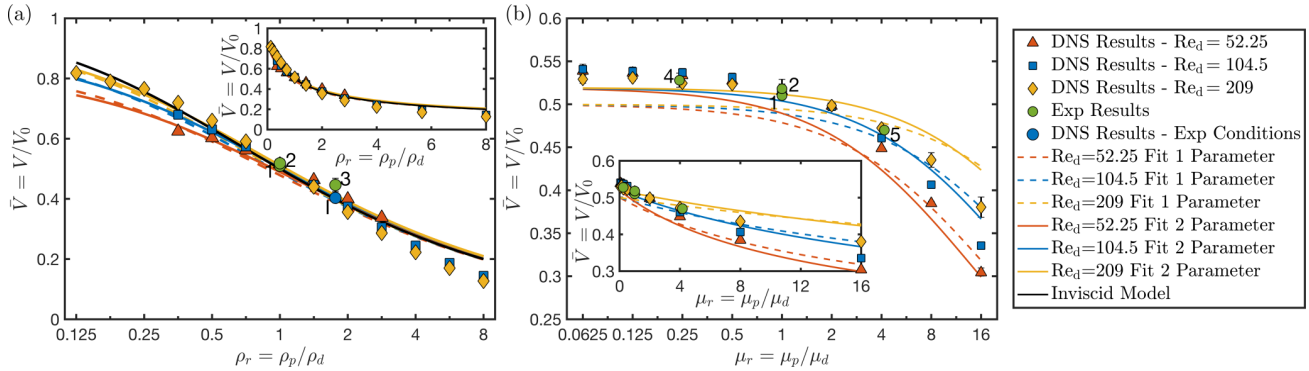

FIG. 4. Penetration velocity including simulations, experiments, and models for (a) fixed viscosity ratio and varying density ratio and (b) fixed density ratio and varying viscosity ratio. In each case the droplet corresponds to a $D = 1.9$ mm 5 cSt SO drop impacting at either 1.1, 0.55, or 0.275 ms^{-1}, with the pool density or viscosity varied to produce the correct ratio. Note the abscissa is logarithmic in the main figure and linear in the inset. Where error bars are not visible they are smaller than the symbol itself. The numbering of the experimental results (●) is consistent between (a) and (b) and are as follows: (1) 5 cSt SO drop on 5 cSt SO pool $\mathrm{Re}_d = 197.7$ ($\overline{\mathrm{Re}} = 197.7$), $\mathrm{We}_d = 26.6$, $\mathrm{Fr}_d = 4.5$; (2) water drop on water pool $\mathrm{Re}_d = 1110.2$ ($\overline{\mathrm{Re}} = 1110.2$), $\mathrm{We}_d = 6.6$, $\mathrm{Fr}_d = 2.7$; (3) 5 cP water-glycerol solution drop on FC-40 pool $\mathrm{Re}_d = 274.1$ ($\overline{\mathrm{Re}} = 285.8$), $\mathrm{We}_d = 9.4$, $\mathrm{Fr}_d = 3.2$; (4) 20-cSt SO drop on 5 cSt SO pool $\mathrm{Re}_d = 58.4$ ($\overline{\mathrm{Re}} = 243.3$), $\mathrm{We}_d = 29.7$, $\mathrm{Fr}_d = 3.9$; and (5) 5 cSt SO drop on 20-cSt SO pool $\mathrm{Re}_d = 201.9$ ($\overline{\mathrm{Re}} = 48.5$), $\mathrm{We}_d = 27.0$, $\mathrm{Fr}_d = 4.4$. The range $3.27 \leqslant \overline{\mathrm{Re}} \leqslant 3344$ is explored in panel (b). ● represents DNS run with same conditions of experimental point denoted by ●. Representative videos are presented as part of Appendix D.

effect of the viscosity ratio is comparatively smaller, being particularly minor for viscosity ratios less than 1. This is, however, entirely expected; as noted above, the coefficient of the viscosity ratio in the fitted models is an order of magnitude below its density ratio counterpart. The difference between the one- and two-parameter models (1) and (2) is most pronounced for low-viscosity ratios. In this regime the viscous contribution is small and therefore it is the density coefficient that determines the displacement velocity. While the two-parameter model (2) has increased accuracy, there is scope for improvement. Figure 5 shows the data plotted using the updated expression (3) based on the modified Reynolds number $\overline{\mathrm{Re}}$, which elegantly collapses the dataset onto this new dimensionless grouping. This result demonstrates the asymptotic behavior of $\bar{V}$ for large values of $\overline{\mathrm{Re}}$, further confirming the description above. For small viscosity ratios the majority of the viscous dissipation occurs within the drop rather than the pool (as discussed in more detail Appendix C)—an aspect deemed negligible in the models. Attempts to include this effect have, however, led to overfitting and ultimately loss of generality. Furthermore, previous work [30] into droplet impact onto solid surfaces has shown that, for low-speed impacts, the viscous dissipation due to the presence of the air layer can become significant. We have looked into this effect for the setup presented here, with more details also presented in Appendix C. Our results indicate that the contribution of the air toward the total viscous dissipation does not translate into a significant effect on the penetration velocity even for comparatively lower Reynolds numbers. While the presence of the gas may significantly affect the dynamics in droplet-solid impacts, the deformable nature of the impacted surface appears to mitigate these effects over the regimes and timescales of interest here.

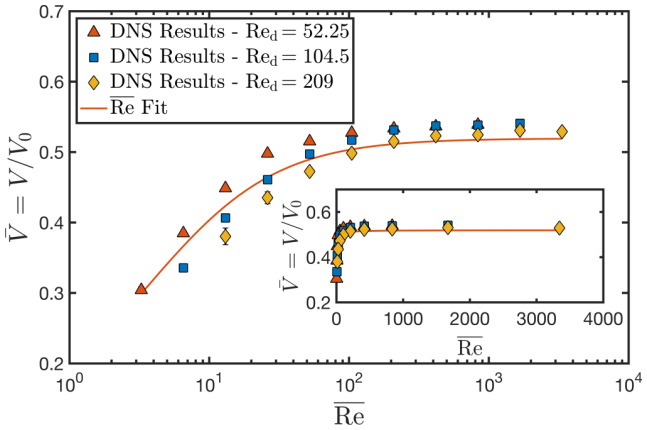

FIG. 5. The dataset from Fig. 4(b) showing the penetration velocity as a function of the composite Reynolds number $\overline{\mathrm{Re}}$ for density ratio $\rho_r = 1$. The inset represents the same plot with linear scale for the abscissa. While in this case the droplet-based Reynolds number Re_d is not relevant, the distinction between the points is retained in order to facilitate comparisons to Fig. 4(b).

We also revisit recent results in the literature in order to further contextualize the predictive power of our derived model. For the case of a 500-cSt SO drop impacting onto a 1-cSt SO pool (with $\mu_r \approx 0.002$, $\rho_r = 0.843$), Li *et al.* [24] report a normalized penetration velocity of 0.54 ± 0.02. While the exact Reynolds number for this case is not provided, the range of Re_d is given as $1145 < \mathrm{Re}_d < 8500$ and thus, combined with the very small viscosity ratio, we find it justifiable to consider the viscous term in the model when calculating $\bar{V}$ as being negligible. This is further supported by Fig. 4, where for very low viscosity ratios we found that the penetration velocity varies only weakly with μ_r. Thus substituting $\rho_r = 0.834$ in (1) and (2) and ignoring the viscous term we obtain $\bar{V} = 0.534$ and $\bar{V} = 0.554$, respectively, both of which are in good agreement with previously reported findings in this regime [24].

VII. CONCLUDING REMARKS

In this study we uncovered and systematically investigated the rich behavior of the impacting front between a drop and pool in the context of general multiliquid impingement scenarios. Motivated by the commonplace strong discrepancies in physical properties (density and viscosity) between the impactor and its target, we used high spatial and temporal resolution experimental methods to capture a previously unrecorded level of detail, as well as direct numerical simulations capable of discerning the delicate multiscale features within such challenging contexts. We constructed a theoretical model accounting for all of these parameters, building on previous simpler single-liquid inviscid approaches. We showed that both trends and quantitative predictions for the impacting front velocity can be encapsulated as part of a simple formula $\bar{V} \approx [1 + 2.71\rho_r + (24.3983/\mathrm{Re}_d)\mu_r]^{-1/2} \approx (1 + 2.71\rho_r + 24.3983\,\overline{\mathrm{Re}})^{-1/2}$, with predictive capabilities spanning three orders of magnitude in density and viscosity ratios, as well as a wide range of impact conditions described by $50 \leqslant \mathrm{Re}_d \leqslant 1110$ or $3.27 \leqslant \overline{\mathrm{Re}} \leqslant 3344$. This allowed us to unfold and explain a rich landscape of impact front behaviors, with significant departures from the typically used $\bar{V} = 1/2$ formula derived in single-liquid impingement scenarios. In particular, it allowed us to determine that the main contribution to the penetration velocity is the inertia due to the differing densities of the drop and pool. Furthermore, we have characterised the non-negligible decrease in the impact velocity found as the viscosity ratio between the pool and drop is larger than unity, while also theoretically and experimentally confirming that the penetration velocity does not change significantly should the pool viscosity be lower than that of the drop. The developed framework provides substantial insight into general multiliquid systems of interest for the first time, which is particularly relevant given that more often than not drops will impact different fluids—when painting, printing, and even cooking.

The raw data, as well as the code supporting the numerical findings of this study, are available from the corresponding author upon request.

ACKNOWLEDGMENTS

A.A.C.-P. was supported by a Royal Society University Research Fellowship URF/R/180016 and USA-CBET/UK-EPSRC Grant No. EP/S029966/1. B.D.F. was supported by a UK-EPSRC DTA Studentship (2118171). R.C. and A.A.C.-P. further acknowledge support from USA-CBET/UK-EPSRC Grant No. EP/W016036/1. The authors thank the anonymous referees, whose comments led to significant improvements of the presented work.

APPENDIX A: NUMERICAL SETUP AND VALIDATION

In what follows we provide relevant details on our DNS setup, as well as information on the typical computational effort required to ensure accurate and robust results in this context. We have developed our code as part of the Basilisk [25] package, an open-source second-order accurate in time and space partial differential equation solver, employing the volume-of-fluid (VOF) method for interfacial flows. With these simulations we are able to both validate against our own experimental results (as well as previous studies in the literature), complement them with flow information which is difficult to image or extract, as well as investigate a wider range of density and viscosity ratios that may not be experimentally feasible.

One of the strengths of this computational platform in the context of rapidly evolving multiscale interfacial flows rests in its ability to employ both adaptive mesh refinement (AMR) and parallelization capabilities. Figure 1(c) shows the snapshot of the flow demonstrating the spatial variance of the resolution level to be focused around the drop and pool interfaces. In this case the mesh is adapted based on changes in the magnitude of the velocity field and interface location. The saving from using AMR is considerable (by at least an order of magnitude in our context), reducing the number of degrees of freedom down to $\mathcal{O}(10^5)$, which is tractable using sufficient computational power. Up to 2500 CPU hours extending over 32 threads have been employed to ensure submicron resolution and a sufficient level of accuracy for robust results. Mesh independence, comparison to experimental data (elaborated on in Sec. IV), as well as early validation to the multifluid liquid lens literature [21,31] have been conducted to ensure the reliability and reproducibility of the numerical results. In regimes of interest it was generally found that a smallest computational cell size equivalent to approximately 2000 cells per drop diameter was required for robust behavior. Tests with up to 4000 cells per diameter were frequently conducted to affirm the quality of the results, with 8000 cells occasionally employed over early timescales in order to ascertain the level of detail needed for the most delicate simulations described by either larger impact velocities or stronger contrasts between physical properties of the impacting drop and the pool.

In order to measure the pool displacement velocity the simulation outputs the pool, air and drop interfaces every 0.001 simulation time (of a maximum simulation time of up to 0.6, corresponding to a physical time of between 1 and 4 ms). Numerically obtained drop interfaces are then postprocessed in MATLAB in order to extract the center line position of the interface as detailed below from which the penetration velocity is found.

Specifically for this problem we need to use a three-phase version as we need to be able to simulate the motion of the pool, drop, and surrounding air. In order to do this, instead of using the standard one VOF field used in a two-phase simulation (as performed previously in, e.g., Ref. [19]), we use three fields, one for each phase. Consequently, each fluid property (for example, density) is expressed in terms of these three VOF fields, and here we use the arithmetic mean for the density and the harmonic mean for the viscosity as this produces more stable results at large viscosity ratios. Furthermore, in the three-phase case, as there is a VOF for each fluid, this means that at each physical interface there are actually two VOF interfaces. Consequently, the surface tension coefficient for each VOF is set such that at each physical interface the surface tension coefficients of the two present VOFs sum to produce the correct interfacial tension. Specifically for phase i of phases i, j, and k the surface tension coefficient σ_i is set to be equal to $(\sigma_{ij} + \sigma_{ik} - \sigma_{jk})/2$; consequently, if, for example,

there was an interface between phases i and j then σ_i and σ_j would sum to σ_{ij}, the correct value.

As well as verifying the code with comparisons to experiments performed here and in the literature reported below the three-phase solver was also verified by simulating the case of a liquid lens whereby a spherical drop is initialized at rest in a pool and subsequently attains the shape of a lens due to the three different surface tension forces acting on it. The equilibrium values of the interface angles from these simulations are then extracted and compared to the theoretical ones showing good agreement and thus that the three-phase solver is performing as it should. A similar approach to verify a three-phase solver using liquid lenses was performed in Ref. [21].

APPENDIX B: INTERFACE VELOCITY CALCULATION

As the main aim of this work is to find the drop penetration velocity which to do so we need to track the displacement of the liquid-liquid interface as part of the impingement process. The technique used should be sufficiently robust to accurately discern the quantities of interest even in our more general setup with potentially vastly different density and viscosity ratios between drop and pool, which we show can introduce substantial variance in the dynamics. The presence of the air film between the pool and drop which ruptures during the impact contracting into a central bubble can make the tracking of the pool motion ambiguous.

Figure 6 shows the results of four different methods of tracking the pool motion and the effect that the bubble has. When tracking the top or the bottom of the bubble (which corresponds to the underside of the drop or the top of the pool, respectively) the contraction of the ruptured air film into a central bubble causes a large deviation from the overall pool motion resulting in a large disturbance to the measured velocity. One possible way to avoid this would be to track the midpoint of the bubble as one might assume that the deviations on the top and bottom would cancel out producing a smooth measure of the pool displacement. As is seen from Fig. 6, this produces an improved result, with only minor velocity deviations. However, looking at Fig. 7, we can see that when the density or viscosity ratios are far from 1 the bubble can become displaced either upwards into the drop or downwards into the pool. In these cases the bubble center point does not correspond to the drop-pool interface location and the motion of the bubble into the pool or drop can drastically affect the measured velocity.

For this reason we introduce a new way of finding the pool position by extracting points on the drop-pool interface sufficiently far away from the central bubble(s) and fitting a quadratic to these points to find where the interface would be in the absence of the entrapped bubble. Figure 7 shows the results of the proposed methodology for identical and different pool and drop densities and viscosities, from which it can be seen that this method produces excellent results even for significantly varying physical properties. As can be seen in the case of equal density and viscosity ratios, the fitting method and bubble midpoint produce very similar results but the greatly increased performance is seen for when these ratios are different and the bubble detaches and becomes encapsulated into the drop or the pool. The temporal results for one such fitting method can also be seen in Fig. 6, where there are no perturbations to the motion visible. Furthermore, as stated in Sec. VI, the penetration velocity was found by averaging the pool velocity over 0.1 dimensionless time units. During this interval, the instantaneous velocity remained constant to within ∼2% of the average velocity for the vast majority of analyzed scenarios (see negligible error bars in Fig. 4 as relevant proxy for the error magnitudes). The least-well-behaved result can be seen in Fig. 4(b) for a large viscosity ratio $\mu_r = 16$ and a more violent impact, in which case instantaneous velocities still remained within 4.5% of the average velocity reported. Simulations and experiments also agreed very well (as demonstrated in Fig. 2). The theoretical model, on the other hand, only offers a constant value for the penetration speed, as it is not a dynamic model and, as described in the text, offers information relevant to a short time after impact. Due to the available computational resources, the simulations ran for 0.6 dimensionless time units. As shown in Fig. 6, the penetration speed V/V_0 hardly changes from $t = 0$ to $t = 0.25$ (dimensionless time, equivalent to 800 μs for this particular case), consistent with the experimental values for most cases. As the bulk of the drop continues to penetrate, further viscous dissipation, buoyancy effects, drop and pool deformation,

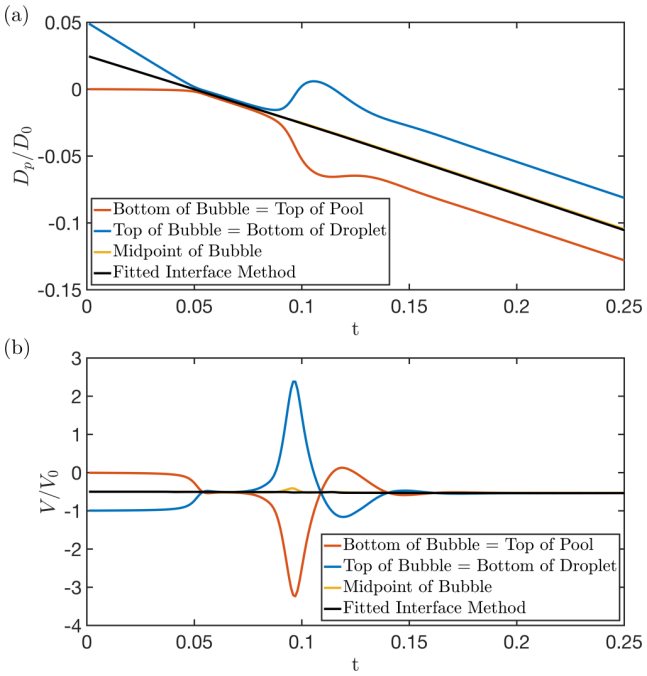

FIG. 6. (a) The front displacement and (b) velocity against simulation time for four different measurement techniques. In the case of tracking either the top or bottom of the bubble (corresponding the underside of the drop or the top of the pool, respectively) the contraction of the air film into a bubble produces large variations in the displacement and thus velocity. Following the middle of the bubble lessens this effect, but it is still visible in the velocity. By fitting a quadratic function to the profile of the underside of the drop (as demonstrated in Fig. 7), an accurate measure of the front motion can be found. In this case the simulation corresponds to the impact of a 5 cSt SO drop onto an identical pool with $\mathrm{Re}_d = 104.5$ ($\overline{\mathrm{Re}} = 104.5$), $\mathrm{We}_d = 26.724$, and $\mathrm{Fr}_d = 4.0$ at resolution level 12.

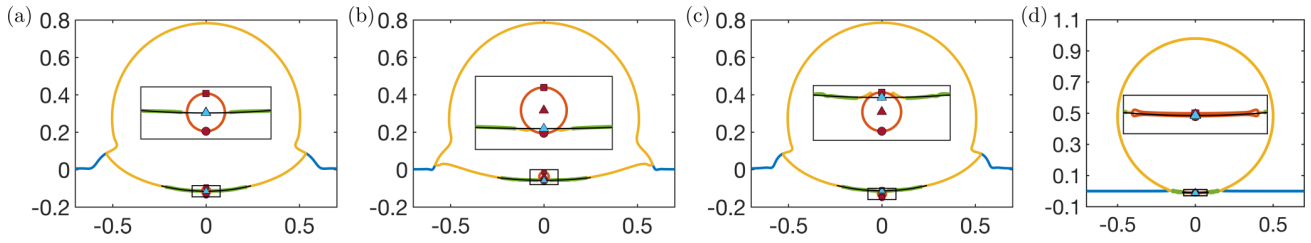

FIG. 7. Comparison of the different methods for tracking the interface position for (a) $\rho_r = 1$, $\mu_r = 1$, $t = 0.116$; (b) $\rho_r = 4$, $\mu_r = 1$, $t = 0.216$; (c) $\rho_r = 1$, $\mu_r = 0.5$, $t = 0.216$; and (d) $\rho_r = 1$, $\mu_r = 1$ at early times ($t = 0.016$) just after the rupture of the air film. In all cases the impact conditions are $\mathrm{Re}_d = 104.5$ [$\overline{\mathrm{Re}} = 104.5$ except (c) where $\overline{\mathrm{Re}} = 209.0$], $\mathrm{We}_d = 26.724$, and $\mathrm{Fr}_d = 4.0$ at resolution level 12. In each case the inset shows the bubble region in detail with the maroon square, triangle, and circle showing the bubble top, middle, and bottom, respectively and the cyan triangle the position of the interface by fitting a quadratic to the drop underside. The quadratic function is fitted to the points marked in green on the underside of the drop a sufficient distance away from the central bubble. The black line then shows the result of this procedure.

capillary waves, and effects due to the presence of the bottom of the pool, etc. will result in the penetration velocity eventually changing, a detail that is not captured here. We have tested this algorithm across our target parameter space and found it to be both reliable and efficient. The geometrical reconstruction procedure was found to be sensitive over short timescales only in extreme scenarios in which multiple topological changes such as coalescence and rupture events happen in very quick succession or are particularly rapid. These were observed in isolated cases toward the highest end of our tested impact velocities (e.g., water-glycerol drop dataset in Fig. 3), with the algorithm still providing meaningful insight into the target interfacial evolution even in these difficult conditions. The proposed fitted interface method proved to be an excellent tool for the target dynamics, which included complex scenarios in which oscillations in the bubble formed following the rupture of the trapped gas film were observed in the present exploration, while also being relevant to regimes investigated in other recent studies [10].

APPENDIX C: EFFECT OF VISCOUS DISSIPATION

When deriving the model accounting for the affect of viscosity we assumed that its effect was to cause a loss of energy due to the viscous dissipation in the pool which could be included in the energy balance. To produce a simple model we took a scaling argument for how the viscous dissipation depends on the parameters of interest. In order to verify this we will take the full equation describing the viscous energy dissipation and evaluate it numerically throughout the simulation to quantify the energy dissipation and how it varies with the pool to drop viscosity ratio.

Repeating the equation for the viscous energy dissipation rate per unit volume in axisymmetric coordinates from Sec. V as $\epsilon_\mu(r,z) = 2\mu[(\frac{\partial V_r}{\partial r})^2 + (\frac{V_r}{r})^2 + (\frac{\partial V_z}{\partial z})^2] + \mu(\frac{\partial V_r}{\partial z} + \frac{\partial V_z}{\partial r})^2$, where the subscripts r and z refer to the radial and axial coordinates respectively, we measure the total energy dissipated due to viscosity by integrating this equation over the entire volume and over time. A redimensionalization of the energy results would be based on the grouping $\rho_d D^3 V_0^2$ built on the reference physical values for drop density, diameter and initial velocity embedded in the simulation setup. It is, however, useful to retain a dimensionless viewpoint for the present comparisons. In addition, we can split the energy dissipation into the three different fluids in the system (drop, pool and air) to analyze how the different fluids contribute to the total dissipated energy for different viscosity ratios. We calculate these energies for viscosity ratios from 1/16 to 16 (and fixed density ratio of 1) for the intermediate impact velocity, with results summarised in Fig. 8. In each case the visualized dissipated energy is taken at $t = 0.6$ (the end of the simulation timescale), in order to provide a consistent reference which is independent of when the film rupturing occurs throughout the dataset. We also include an animation as part of the Supplementary Material [32] which illustrates the temporal evolution of the percentage energy dissipation (the inset in Fig. 8). It shows that after the initial early stage

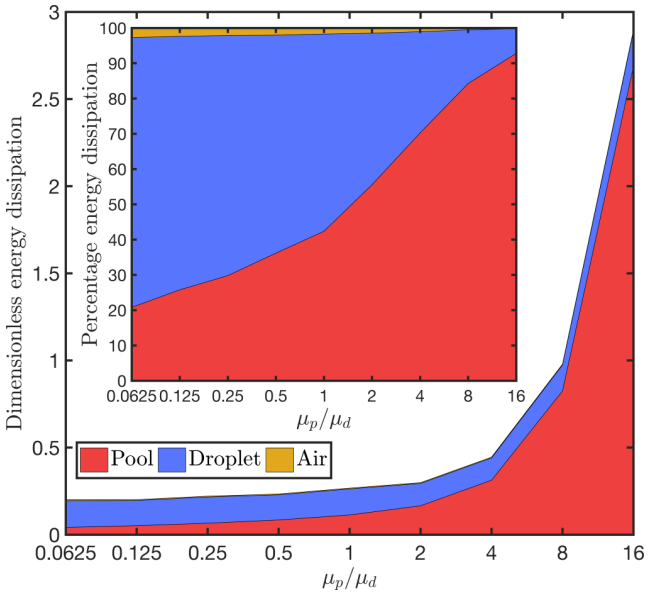

FIG. 8. Dimensionless viscous energy dissipation per phase against viscosity ratio for the intermediate impact conditions of $\mathrm{Re}_d = 104.5$ ($6.53 \leqslant \overline{\mathrm{Re}} \leqslant 1672$), $\mathrm{We}_d = 26.724$, and $\mathrm{Fr}_d = 4.0$ at resolution level 12. In each case the density ratio is 1 and the viscosity ratio varies. The values of the viscous dissipation are taken at $t = 0.6$. The inset illustrates the same data as a percentage of the total energy dissipated.

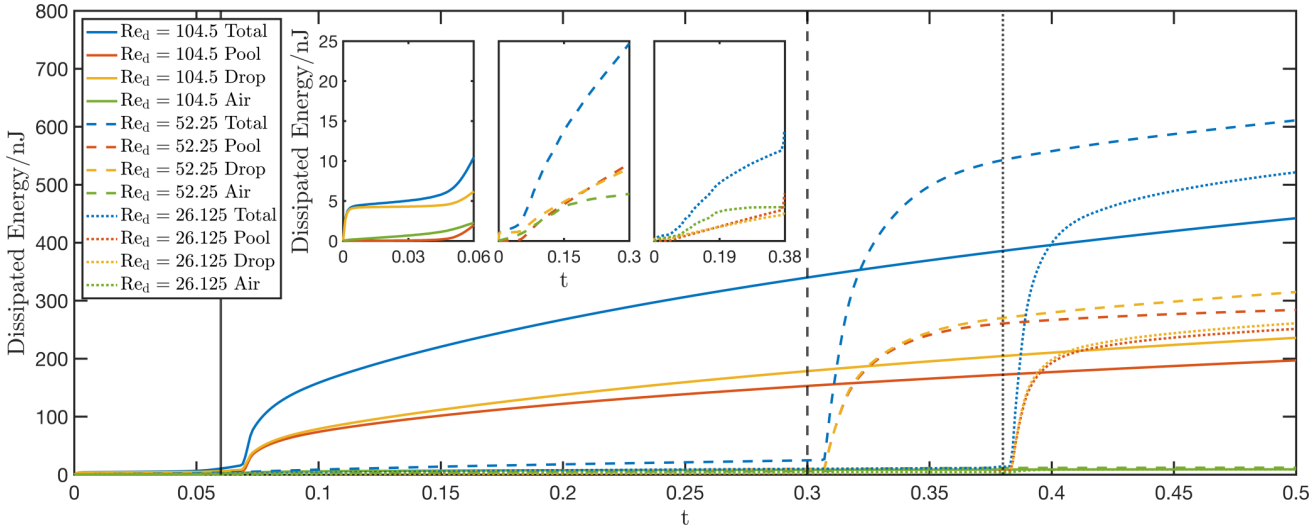

FIG. 9. Temporal evolution of the viscous energy dissipated per phase (by color) for three different impact velocities (solid line $\mathrm{Re}_d = 104.5$ ($\overline{\mathrm{Re}} = 104.5$), $\mathrm{We}_d = 26.724$, and $\mathrm{Fr}_d = 4.0$, dashed line $\mathrm{Re}_d = 52.25$ ($\overline{\mathrm{Re}} = 52.25$), $\mathrm{We}_d = 3.341$, and $\mathrm{Fr}_d = 2.9$ and dotted line $\mathrm{Re}_d = 26.125$ ($\overline{\mathrm{Re}} = 26.125$), $\mathrm{We}_d = 0.835$, and $\mathrm{Fr}_d = 1.4$) for the impact of a 5 cSt SO drop onto an identical pool at resolution level 12. The three inset plots show the energy dissipation for each impact velocity separately, up until the point that the air film ruptures in each case. The time at which this occurs is indicated by the vertical black lines in the main plot, with the impact velocities again indicated by the line style.

($t \approx 0.15$) the relative percentage dissipation in each phase is essentially unchanged.

First, we observe that the energy dissipation is largely constant in the drop and the air, as the viscosities of these phases are constant throughout the different simulations (however, different velocity fields within these phases will clearly affect the energy dissipated). We can clearly see the large difference in the energy dissipated in the pool across the different viscosity ratios from the inset and in particular that for less than unit viscosity ratios, the majority of the energy is dissipated in the drop. By contrast, for ratios greater than one, the majority of the energy is dissipated into the pool. We find that the energy dissipated in the pool for the most extreme ratios 0.0625 and 16 are 0.369 and 23.7 times the value for unit viscosity ratio, respectively.

We therefore identify a threshold level of pool viscosity below which the energy dissipation in the pool becomes negligible relative to the total amount of energy dissipated, only negligibly affecting the pool motion and penetration velocity. This corroborates with our findings on the penetration velocity as shown in Fig. 4(b), where we see that there is a threshold viscosity ratio below which the penetration velocity is unchanged.

We further investigate the influence of the viscous dissipation in the air, as it has been shown to be of importance for low speed impacts [30]. To do so, we consider the temporal variation in the energy dissipated per phase for three different impact velocities, the lower two from Fig. 4 and another one at a lower velocity (corresponding to $V_0 = 0.55$, 0.275, or 0.1375 ms^{-1}).

Figure 9 shows the temporal evolution of the viscous dissipation per phase for three different impact velocities, with the fluids being the same in all cases (i.e., $\rho_r = \mu_r = 1$). In the later postrupture times we observe that the viscous dissipation in the air is negligible for all impact speeds. Looking at the inset plots showing the dissipation before rupture, we notice that in the case of the lowest impact speed the dissipation in the air film is initially the most significant contribution, whereas for the higher impact speeds it is equal to or smaller than its counterparts. However, by $t \approx 0.19$, the energy dissipated in the air levels out, while we can see that the energy dissipated in the droplet and pool continue to rise. The same plateauing of the air dissipation is also visible for the middle impact speed. We note that this time is significantly before the rupture of the air film, and, by inspecting the variation of the pool motion at this stage, we find that the dissipation in the air has a negligible influence on the penetration velocity. One reason we believe that the air has a reduced effect here is the deformability of both droplet and pool surfaces.

Another approach to account for the viscous energy dissipation was recently presented by Tang *et al.* [28] and is extended here to account for different drop and pool fluids. Therein the viscous dissipation in the pool is assumed to occur within a thin boundary layer of thickness δ near to the pool interface with volume $\mathbb{V} = 2\pi R^2 \delta$. Within this region the derivative in the viscous energy dissipation rate per unit volume is approximated as V/δ and the viscous dissipation occurs over the impact time period $\tau = D/V$; this results in $E_\mu^t = C\mu_p(\frac{V}{\delta})^2 \mathbb{V}\tau$. Assuming a scaling for the boundary layer thickness of $\delta = \frac{R}{\overline{\mathrm{Re}}_{\mathrm{pen}}^{1/2}}$, where $\overline{\mathrm{Re}}_{\mathrm{pen}} = \rho_d V D/\mu_p = \bar{V}\overline{\mathrm{Re}}$ is the composite Reynolds number based on the penetration velocity V and pool viscosity μ_p, and substituting this result into the overall energy balance leads to

$$1 = \bar{V}^2 + 3\rho_r \bar{V}^2 + 12C\bar{V}^2 \overline{\mathrm{Re}}_{\mathrm{pen}}^{-1/2}$$
$$= \bar{V}^2 + 3\rho_r \bar{V}^2 + 12C\bar{V}^{3/2}\mu_r \mathrm{Re}_d{}^{-1/2}, \qquad \text{(C1)}$$

with the first expression above being the natural compact form taking into account the modeling assumption of the pool

viscosity being the key ingredient in the nondimensionalization, while the second expression (C1) makes the dependency on the relevant physical property ratios explicit, thus facilitating physical interpretation. We also note that while the expression involving $\overline{\mathrm{Re}}_{\mathrm{pen}}$ appears to be of the same form as the model in the main text and could thus also be rearranged to find an explicit definition for $\bar{V}$, this is not actually the case due to the variable of interest (the penetration velocity V) appearing inside the definition of $\overline{\mathrm{Re}}_{\mathrm{pen}}$. While Eq. (C1) bears similarities with the overall energy balance highlighted in Sec. V, the key difference is that the power of the normalised penetration velocity in the viscous term is now 3/2 rather than 2. Writing $\bar{V} = x^2$, the above energy balance can be written as $Ax^4 + Bx^3 - 1 = 0$ with $A = 1 + 3\rho_r$ and $B = 12C\mu_r \mathrm{Re}_d{}^{-1/2}$. This has the important consequence that there is no convenient explicit solution for $\bar{V}$ [unlike the results (1) and (2)]. It is, however, still possible to find the constant C by fitting the data to Eq. (C1) implicitly, meaning that $\bar{V}$ can be found for a given set of parameters by numerically solving the quartic equation. While this quartic could produce up to four possible solutions in all of the cases considered here there is only one positive real root for x, which is taken as the solution leading to $\bar{V}$.

APPENDIX D: ANIMATIONS

We provide detailed visualisation of one of the cases highlighted in the paper [32], focusing on key physical and numerical quantities such as the color functions underlying each of the fluids in our system, the magnitude of the vorticity, the velocity field norm as well as the grid resolution level.

The selected case is that of a 5 cP water-glycerol solution drop impacting on a FC-40 pool: $\mathrm{Re}_d = 274.1$ ($\overline{\mathrm{Re}} = 285.8$), $\mathrm{We}_d = 9.4$, $\mathrm{Fr}_d = 3.2$, $\rho_r = 1.762$, $\mu_r = 0.959$, $\rho_d = 1052.7\ \mathrm{kgm}^{-3}$, $\mu_d = 0.0049$ Pa s, $\sigma_{\mathrm{da}} = 72\ \mathrm{mNm}^{-1}$, $\sigma_{\mathrm{pa}} = 16\ \mathrm{mNm}^{-1}$, $\sigma_{\mathrm{dp}} = 52\ \mathrm{mNm}^{-1}$. The nondimensional simulation time of 0.4 units is equivalent to 2.04 ms. Direct numerical simulation animations show the velocity magnitude and vorticity and VOF fields and resolution level, respectively [32]. For the associated experimental video provided (captured at 100 000 fps but displayed at 80 fps), we use a 2.560-mm-diameter 5 cP water-glycerol solution drop impacting on a FC-40 pool at $0.502\ \mathrm{ms}^{-1}$ over a duration of 3.7 ms. This case corresponds to point 3 in Fig. 4(a) and is captured as a video [32].

We also include a video showing the temporal evolution of the relative viscous dissipation in each phase corresponding to the inset of Fig. 8 [32].

[1] S. Lejeune, T. Gilet, and L. Bourouiba, Phys. Rev. Fluids **3**, 083601 (2018).

[2] D. W. Murphy, C. Li, V. d'Albignac, D. Morra, and J. Katz, J. Fluid Mech. **780**, 536 (2015).

[3] A. Herczynski, C. Cernuschi, and L. Mahadevan, Phys. Today **64**(6), 31 (2011).

[4] M. A. Hack, M. Costalonga, T. Segers, S. Karpitschka, H. Wijshoff, and J. H. Snoeijer, Appl. Phys. Lett. **113**, 183701 (2018).

[5] E. Parry, D.-J. Kim, A. A. Castrejón-Pita, S. J. Elston, and S. M. Morris, Opt. Mater. (Amsterdam) **80**, 71 (2018).

[6] M.-J. Thoraval, K. Takehara, T. G. Etoh, S. Popinet, P. Ray, C. Josserand, S. Zaleski, and S. T. Thoroddsen, Phys. Rev. Lett. **108**, 264506 (2012).

[7] A. A. Castrejón-Pita, J. R. Castrejón-Pita, and I. M. Hutchings, Phys Rev E. **86**, 045301(R) (2012).

[8] M.-J. Thoraval, K. Takehara, T. Etoh, and S. Thoroddsen, J. Fluid Mech. **724**, 234 (2013).

[9] T. Tran, H. de Maleprade, C. Sun, and D. Lohse, J. Fluid Mech. **726**, R3 (2013).

[10] Z. Jian, M. A. Channa, A. Kherbeche, H. Chizari, S. T. Thoroddsen, and M.-J. Thoraval, Phys. Rev. Lett. **124**, 184501 (2020).

[11] J. Hendriks, C. W. Visser, S. Henke, J. Leijten, D. B. Saris, C. Sun, D. Lohse, and M. Karperien, Sci. Rep. **5**, 1 (2015).

[12] K. Langley and S. T. Thoroddsen, J. Fluid Mech. **878**, R2 (2019).

[13] K. R. Langley, A. A. Castrejón-Pita, and S. T. Thoroddsen, Soft Matter **16**, 5702 (2020).

[14] M.-J. Thoraval and S. T. Thoroddsen, Phys. Rev. E **88**, 061001(R) (2013).

[15] D. Beilharz, A. Guyon, E. Li, M.-J. Thoraval, and S. T. Thoroddsen, J. Fluid Mech. **779**, 87 (2015).

[16] U. Jain, M. Jalaal, D. Lohse, and D. Van Der Meer, Soft Matter **15**, 4629 (2019).

[17] H. Lhuissier, C. Sun, A. Prosperetti, and D. Lohse, Phys. Rev. Lett. **110**, 264503 (2013).

[18] H. M. Kittel, I. V. Roisman, and C. Tropea, Phys. Rev. Fluids **3**, 073601 (2018).

[19] F. Marcotte, G.-J. Michon, T. Séon, and C. Josserand, Phys. Rev. Lett. **122**, 014501 (2019).

[20] S. Shaikh, G. Toyofuku, R. Hoang, and J. Marston, Exp. Fluids **59**, 1 (2018).

[21] F. Yeganehdoust, R. Attarzadeh, I. Karimfazli, and A. Dolatabadi, Int. J. Multiphase Flow **124**, 103175 (2020).

[22] Y. Semenov, G. Wu, and A. Korobkin, J. Fluid Mech. **766**, 5 (2015).

[23] M. H. Hendrix, W. Bouwhuis, D. van der Meer, D. Lohse, and J. H. Snoeijer, J. Fluid Mech. **789**, 708 (2016).

[24] E. Q. Li, D. Beilharz, and S. T. Thoroddsen, Phys. Rev. Fluids **2**, 073602 (2017).

[25] S. Popinet, Basilisk, http://basilisk.fr.

[26] S. Popinet, J. Comput. Phys. **190**, 572 (2003).

[27] S. Popinet, J. Comput. Phys. **228**, 5838 (2009).

[28] X. Tang, A. Saha, C. K. Law, and C. Sun, Langmuir **34**, 2654 (2018).

[29] S. Wildeman, C. W. Visser, C. Sun, and D. Lohse, J. Fluid Mech. **805**, 636 (2016).

[30] J. De Ruiter, R. Lagraauw, D. Van Den Ende, and F. Mugele, Nat. Phys. **11**, 48 (2015).

[31] B. Wang, C. Wang, Y. Yu, and X. Chen, Phys. Fluids **32**, 012003 (2020).

[32] See Supplemental Material at http://link.aps.org/supplemental/10.1103/PhysRevE.104.065102 for the experimental and numerical videos and animations described in Appendices C and D.

Statement of Authorship for joint/multi-authored papers for PGR thesis

To appear at the end of each thesis chapter submitted as an article/paper.

The statement shall describe the candidate's and co-authors' independent research contributions in the thesis publications. For each publication there should exist a complete statement that is to be filled out and signed by the candidate and supervisor **(only required where there isn't already a statement of contribution within the paper itself).**

Title of Paper:	Dipping into a new pool: The interface dynamics of drops impacting onto a different liquid
Publication Status	▪ Published
Publication Details	Fudge, B.D., Cimpeanu, R. and Castrejón-Pita, A.A., 2021. Dipping into a new pool: The interface dynamics of drops impacting onto a different liquid. *Physical Review E*, *104*(6), p.065102.

Student Confirmation

Student name:	Benjamin David Fudge
Contribution to the paper	Lead Author, performed all experiments and numerical simulations, analysed and presented results, performed theoretical modelling, and writing and editing of manuscript
Signature: 	**Date: 09/12/2022**

Supervisor Confirmation

By signing the Statement of Authorship, you are certifying that the candidate made a substantial contribution to the publication, and that the description described above is accurate.

Supervisor name and title: Prof. Alfonso A. Castrejon-Pita

Supervisor comments: Benjamin D. Fudge led and carried out the research contained in this chapter/article. Other authors provided supervision and funds to carry out the research.

Signature:  **Date:09/12/2022**

4

Droplet Splashing on an Immiscible Viscous Pool

Contents

4.1 Introduction

This chapter showcases the paper *"Drop splashing on viscous immiscible pools"*, which is currently under review in the Journal of Colloid and Interface Science. In this paper we investigate the impact of a droplet onto deep immersible pools of silicone oils, with a range of six orders of magnitude in viscosity ratio between droplet and pool, as well as the effect of this ratio on the threshold to splash. We identify two distinct regimes in the splashing threshold, the first for low viscosity pools (where the pool to droplet ratio is less than ~ 35) whereby the threshold to splash increases with the pool viscosity and the splash itself originates from the pool. In the second (high pool viscosity) regime we observe that the threshold to splash now decreases with pool viscosity, and that the splash originates from the droplet. In the

transition between these regimes we also observe a pool viscosity for which splashing was unable to be achieved for the experimental conditions available in the laboratory.

We start by explaining the observation of which fluid the splash originates from. This is carried out via high resolution simulations aimed at investigating the dynamics of the jet formed during the early stages following the impact. In corroboration with previous results in the literature, we show how the jet composition varies with the pool viscosity, being largely from the pool for low viscosities transitioning to entirely from the droplet for high viscosities. Significantly, we note that the non-splashing case identified above corresponds to when the jet composition transitions from mostly pool to mostly droplet.

Having ascertained the origin of the splash in both cases, we then turn our attention to explaining the differing trends observed in the splashing threshold. Starting with the high viscosity case, we combine the ideas from impact onto soft solids in the literature with the model for the pool motion in the previous chapter to explain the cushioning effect due to the pool motion on the droplet. This has the effect of reducing the maximum pressure in the droplet and thus its tendency to splash. Using the equation for the penetration velocity we are able to quantify the pressure reduction in the droplet, and from this derive an equation governing the splashing threshold showing excellent agreement to the experimental results.

Finally, we then focus on the low viscosity case, where we investigate the different factors involved in the formation of the jet that precedes the splash. We show how the driving force behind this jet remains largely constant across different pool viscosities but the viscous stress opposing it increases with pool viscosity. This explains the increasing threshold to splash observed for these low viscosity pools.

4.2 Publication: Fudge *et. al.* *"Drop splashing after impact onto immiscible pools of different viscosities"*. Published in revised format JCIS 2023

Drop splashing after impact onto immiscible pools of different viscosities

Ben D. Fudge[a], Radu Cimpeanu[b,c,d], Arnaud Antkowiak[e], J. Rafael Castrejón-Pita[f], Alfonso A. Castrejón-Pita[a,*]

[a]*Department of Engineering Science, University of Oxford, Oxford, OX1 3PJ, United Kingdom*
[b]*Mathematics Institute, University of Warwick, Coventry, CV4 7AL, United Kingdom*
[c]*Mathematical Institute, University of Oxford, Oxford, OX2 6GG, United Kingdom*
[d]*Department of Mathematics, Imperial College London,London, SW7 2AZ,United Kingdom*
[e]*Institut Jean le Rond d'Alembert, Sorbonne Universite, 4 Place Jussieu, Paris, 75005, France*
[f]*Department of Mechanical Engineering, University College London, London, WC1E 7JE, United Kingdom*

Abstract

Droplet impact onto liquid pools is a canonical scenario relevant to numerous natural phenomena and industrial processes. However, despite their ubiquity, multi-fluid systems with the drop and pool consisting of different liquids are far less well understood. Our **hypothesis** is that the post-impact dynamics greatly depends on the drop-to-pool viscosity ratio μ_p/μ_d, which we explore over a range of six orders of magnitude using a combination of **experiments** and **theoretical approaches** (mathematical modelling and direct numerical simulation). Our **findings** indicate that in this scenario the splashing threshold and the composition of the ejecta sheet are controlled by the viscosity ratio. We uncover that increasing the pool viscosity decreases the splashing threshold for high viscosity pools ($\mu_p/\mu_d \gtrsim 35$) when the splash comes from the droplet. By contrast, for low viscosity pools, the splash sheet comes from the pool and increasing the pool viscosity increases the splashing threshold. Surprisingly, there are conditions for which no splashing is observed under the conditions attainable in our laboratory. Furthermore, considering the interface velocity together with asymptotic arguments underlying the generation of the ejecta has allowed us to understand meaningful variations in the pressure during impact and rationalise the observed changes in the splashing threshold.

Keywords: drops, splashing, wetting, impact, experiment, direct numerical simulation

1. Introduction

Droplet impact onto a deep pool is a topic that has seen significant research owing to the plethora of phenomena for which it acts as a fundamental framework. Examples include the formation of a Rayleigh jet and break-up into droplets [1–3], the formation and subsequent collapse of craters on impacts on a low viscosity pool [4–7], the entrapment of air bubbles [8, 9], or the formation of a sheet at the droplet-pool interface [10, 11]. In most past scenarios, both the impacting drop and the pool are composed of the same liquid. In moderate-to-high speed scenarios, the focus has been on the complex early stages of impact, which culminate, in the more violent cases, in the formation of liquid sheets which are then subject to break-up. The combination of experimental and numerical tools [11] has led to models for the pressure

*Corresponding author
Email addresses: benjamin.fudge@eng.ox.ac.uk (Ben D. Fudge), radu.cimpeanu@warwick.ac.uk (Radu Cimpeanu), arnaud.antkowiak@upmc.fr (Arnaud Antkowiak), castrejon@cantab.net (J. Rafael Castrejón-Pita), alfonso.castrejon-pita@wadham.ox.ac.uk (Alfonso A. Castrejón-Pita)

variation during impact and the key velocities in the system [6, 12, 13]. In fact, Wagner theory has been successfully used to model the early-time splashing dynamics [14, 15]. By contrast, the impact of a droplet onto a different fluid provides challenges that require paradigm shifts from the single-fluid systems. The introduction of a distinct second liquid permits the variation of physical properties such as density and viscosity between the droplet and pool. Only very recently [16–19] has progress in two-fluid impact with significant variations in fluid properties been made experimentally and theoretically, revealing significant changes in the dynamics of the interfaces, the formation of the liquid sheet, and its shape and composition.

In the single-fluid impact regime, the splashing threshold is one of the most studied quantities due to its practical applications, especially during the impact onto rough surfaces [20], oblique impact [21–23], impact at reduced pressures [24] or onto soft solids [25]. Research into the splashing threshold for two-fluids impact is more limited however. For the case of droplet impact onto thin films of a different fluid Kittel *et al.* [17] studied the splashing threshold in terms of the film to droplet viscosity ratio, and concluded that the dynamics is controlled by the properties of the lower viscosity fluid, as this is where splashing originates from. Marcotte *et al.* [18] examined ethanol droplet impact onto deep water-glycerol solution pools, which allowed the variation of viscosity in a miscible setup in which the interfacial tension was set to zero. The investigation focused on the impact process, interface shape identification and orientation changes of the ejected sheet upon impact. Unfortunately, the splashing threshold was not discussed, however the contributions of the different liquids to the ejected sheet as the viscosity ratio varied was discussed qualitatively therein.

Despite this early progress, a comprehensive understanding of the effect of the liquid pool properties on splashing is still lacking. In this work we experimentally investigate the impact of a droplet onto a viscous pool across several orders of magnitude of viscosity ratios ($\mathcal{O}(1) - \mathcal{O}\left(1 \times 10^6\right)$) and quantify the effect of this ratio on the splashing threshold. This is complemented by high-resolution direct numerical simulation of three-phase impacts, looking at the jet composition as the viscosity ratio varies and its comparison with experimental observations. Finally we theoretically develop a model for the splashing threshold using a combination of analytical arguments, numerical data, and the dynamics of the drop-pool interface extended from our previous work [19].

2. Experimental method

Our setup is illustrated in Fig. 1 (a) where drops of Fluorinert FC-770 were generated from a stainless steel needle and a syringe pump to fall under gravity. Droplets impact onto a 20 mm-deep pool filled with silicone oil, with viscosity μ_p ranging between $2 - 1{,}000{,}000$ cSt. Fluorinert is chemically stable, inert, resistant to contamination, and has a high density and low surface tension leading to splashing at low impact speeds. Silicone oils and FC-770 are immiscible, providing a factor scarcely investigated in liquid-on-liquid impacts. The impact events are captured with a high speed camera (either a Phantom v12 or a Phantom v2512) in a shadowgraphy configuration at up to 310,000 frames-per-second and resolutions of $\sim 6\,\mu$m per pixel. The pool depth is large enough to prevent any boundary effects due to the finite-size of the container. The impact velocity is varied by adjusting the fall height. Silicone oils have constant density and surface tension over the viscosity range used here. Image analysis is used to obtain the droplet impact speed, diameter, eccentricity e, and orientation. Only impacts with a low eccentricity ($e < 0.3$) are retained to avoid effects associated to shape irregularities [26].

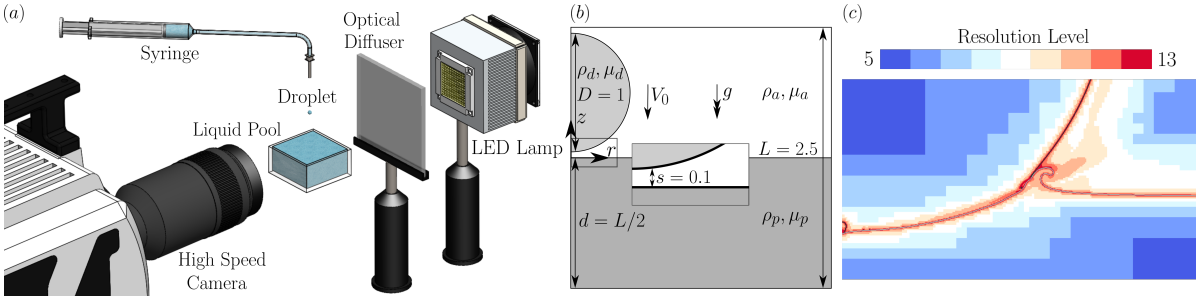

Figure 1: (a) Diagram of the experimental setup, with a single camera capturing both the falling droplet and the subsequent post-impact dynamics. (b) Sketch of the axisymmetric simulation domain in its initial state. (c) Zoomed-in view for a typical simulation showing the adaptive mesh refinement, achieving spatial resolutions down to 0.5 μm.

3. Direct numerical simulation

Direct numerical simulations are carried out using Basilisk [27–29] to provide greater insight into regions that are challenging to visualise. A three-phase setup is deployed to resolve the multi-fluid system consisting of the drop, the impacted pool and surrounding gas. This computational environment has been validated previously by Fudge *et al.* [19]. This method allows us to individually track each of the phases and thus study the splashing characteristics to quantify the effect of the viscosity ratio on the jet composition. Figure 1 (b) shows the simulation setup. We use adaptive mesh refinement to vary the grid resolution on the regions of interest resulting in much more efficient simulations with a maximum resolution of 0.5 μm per grid point (~ 1860 grid points per diameter) with an example mesh shown in Fig. 1 (c). The length and velocity scales are made dimensionless using the droplet diameter D and impact velocity V_0 and the time scale is made dimensionless by D/V_0. The Fluorinert-air and silicone oil-air interfaces have σ_{da}=15.0 $\pm$0.1mNm^{-1} and σ_{pa}=20.0 $\pm$0.1mNm^{-1} respectively, with the value for the interface between silicone oils and air varying by less than 5% across the viscosity range considered here. For the Fluorinert-silicone oil interface we experimentally measure the interfacial tension using the pendant drop method for several different oil viscosities, achieving a constant value of σ_{dp}=4.6 $\pm$0.2mNm^{-1}, which we use for the simulations. We note here that, within experimental error, the silicone oil-air interfacial tension is equal to the sum of the other two pairings, meaning that a static liquid lens equilibrium is reached as the Neumann triangle is closed. Figure 2 shows example numerical interfaces for three different impact scenarios, revealing excellent agreement with experiments.

The key quantitative outputs we consider are interfacial shapes, as well as information on velocities, viscous stresses, pressures, and vorticity that aid our understanding of the rich impact landscape. Moreover, using the three-phase method allows us to individually track, among many other properties, the contribution from each of the phases to the ejected jet and thus splashing characteristics, and therefore quantify the effect of the viscosity ratio on the jet composition: Resulting fluid-fluid interfaces are processed in order to extract the jet composition, as illustrated in Fig. 3 for two different impact scenarios. In each case the root of the jet is identified based on the two points of maximum curvature either side of the jet tip. The jet base is then taken as the straight line between these two points denoted by the dashed black line in Fig. 3. The total jet volume and the volumes of the pool and droplet within the jet are then found by integrating the profiles between the jet roots. This level of detail, alongside associated numerical information, allows us to expand on experimental findings and generate predictive capabilities, to be discussed in the following section. The code implemented as part of

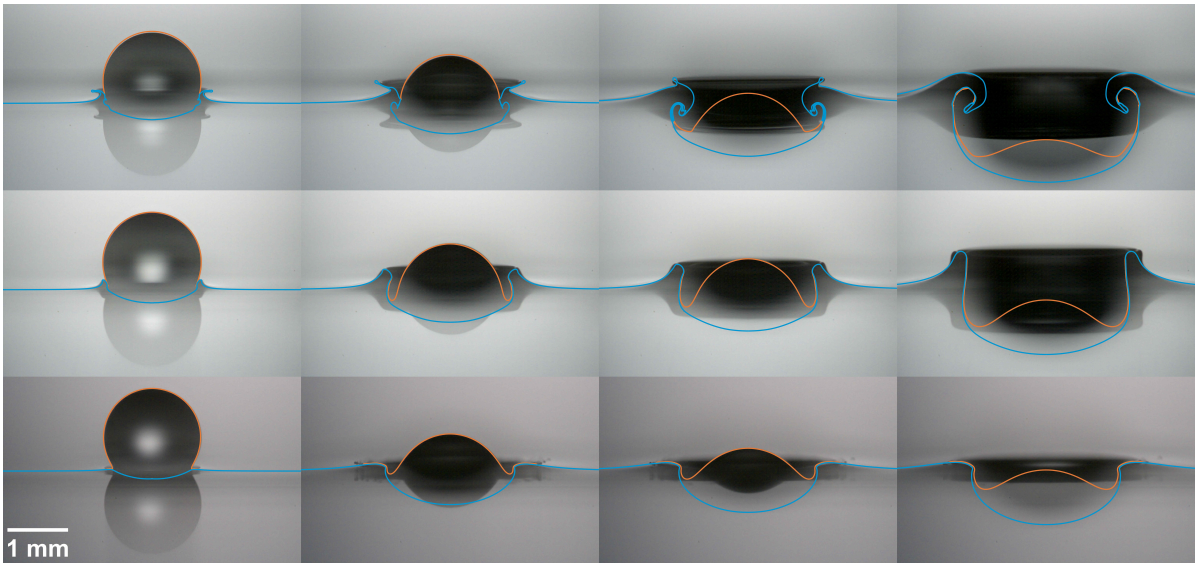

Figure 2: Comparison between experimental data and direct numerical simulation results for the impact of 1.6 mm FC-770 droplets at 3.2 ms^{-1} onto: 20 cSt silicone oil pool at times 0.12 ms, 0.24 ms, 0.44 ms and 0.72 ms post-impact from left to right (top row), 50 cSt silicone oil pool at times 0.08 ms, 0.24 ms, 0.32 ms and 0.56 ms post-impact from left to right (middle row) and 350 cSt silicone oil pool at times 0.04 ms, 0.28 ms, 0.36 ms and 0.48 ms post-impact from left to right (bottom row). In each case the droplet interface is in orange and the pool interface in blue. The scale bar in the bottom left frame applies throughout. Supplementary video material of direct numerical simulation data (fluid phases and adaptive grid) is included for each of the three examples.

this investigation is available at `https://github.com/rcsc-group/DropImpactViscousPool`.

4. Discussion

The impact outcome is shown in Fig. 4 in terms of splashing parameter K [21] versus the pool-to-droplet viscosity ratio, $\mu_r = \mu_p/\mu_d$. Here $K = \mathrm{We}\sqrt{\mathrm{Re}} = \sqrt{(\rho_d^3 D^3 V_0^5)/(\sigma_{da}^2 \mu_d)}$, where $\mathrm{We} = \rho_d D V_0^2/\sigma_{da}$ and $\mathrm{Re} = \rho_d D V_0/\mu_d$ are the Weber and Reynolds numbers with ρ_d, D, V_0, σ_{da} and μ_d denoting the droplet density, diameter, impact velocity, surface tension, and viscosity. We have considered the splashing threshold of K as the midpoint between the splashing/non-splashing regions, denoting it as yellow squares in Fig. 4. The inset images show splashing for four different viscosity ratios (1.39, 242.75, 3467.86 and 41614.29) at an approximately constant K value of 120,000, which allows us to visualise the qualitative difference between the impacts at different pool viscosities. Specifically we can see that there is noticeable pool motion for the lower pool viscosity cases, whereas for the higher viscosities there is no noticeable deformation and the impact dynamics resembles that onto a solid. Also note that for the higher two of these viscosities the K value is significantly above the threshold, and thus the splash appears significantly more vigorous than for the two lower ratios.

Quantitatively we observe that, for low pool viscosity ratios ($\mu_p/\mu_d < 35$), the splashing threshold increases with pool viscosity. By contrast, for greater pool viscosities ($\mu_p/\mu_d > 35$) the threshold does the opposite. An intuitive explanation is that, as the pool viscosity increases, the pool motion decreases and thus less energy is removed from the droplet, making a splash more likely. At $\mu_p/\mu_d \sim 35$ ($\mu_p = 50$ cSt) no experimental condition resulted in splashing (our maximum impact speed was $V_0 = 5.62\,\mathrm{ms}^{-1}$, or $K = 681{,}396$). Interestingly, a numerical investigation of this scenario also led to no evidence of splashing. In fact, simulations were performed at other higher velocities, up to the theoretical terminal velocity of the drop, and no liquid fragmentation was detected. We identify that $\mu_p = 50$ cSt marks the transition below

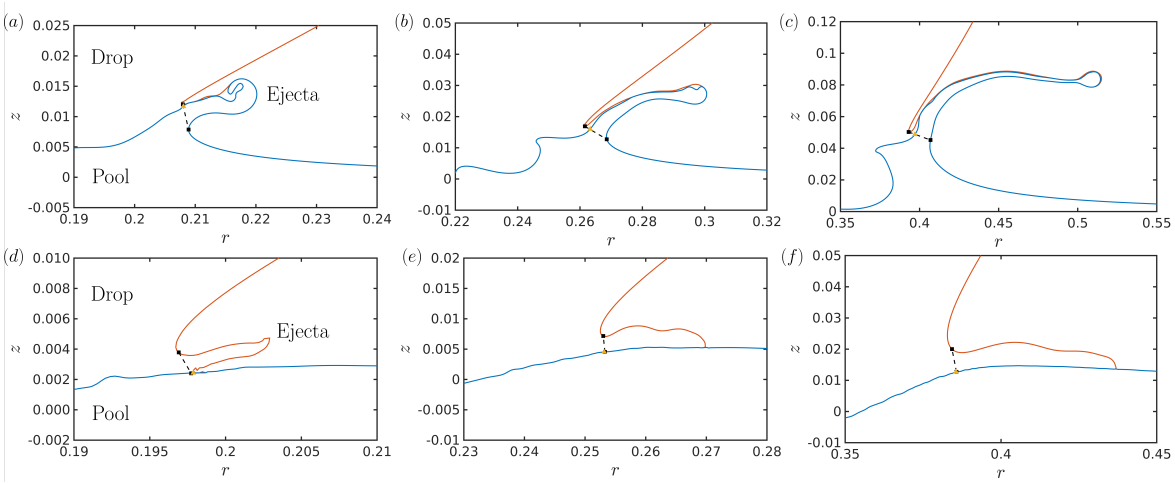

Figure 3: Example calculation of jet contributions for the impact of a 1.6 mm FC-770 droplet at 3.2 ms^{-1} onto a pool with (a) $\mu_p = 5$ cSt at $t = 0.03$, (b) $\mu_p = 5$ cSt at $t = 0.05$, (c) $\mu_p = 5$ cSt at $t = 0.125$, (d) $\mu_p = 350$ cSt at $t = 0.03$, (e) $\mu_p = 350$ cSt at $t = 0.05$ and (f) $\mu_p = 350$ cSt at $t = 0.125$. The top and bottom rows correspond to the left and rightmost plots in Fig. 5 respectively. Note the different axis scales in each plot which are the dimensionless simulation radial position and height.

which the ejected splash originates from the pool fluid (crown splash), whereas above this viscosity the splash comes from the droplet (prompt splash). Our hypothesis is that increasing the pool viscosity has opposing effects on the different types of splashing, i.e. increasing the pool viscosity inhibits crown splashing, but enhances prompt splashing. Consequently we believe that this pool viscosity corresponds to the point where the overall splash suppression is the highest when considering a combination of the two mechanisms. This is consistent with the previous observation that the pool displacement is very small for higher viscosity pools, making it unlikely that the splash would come from it.

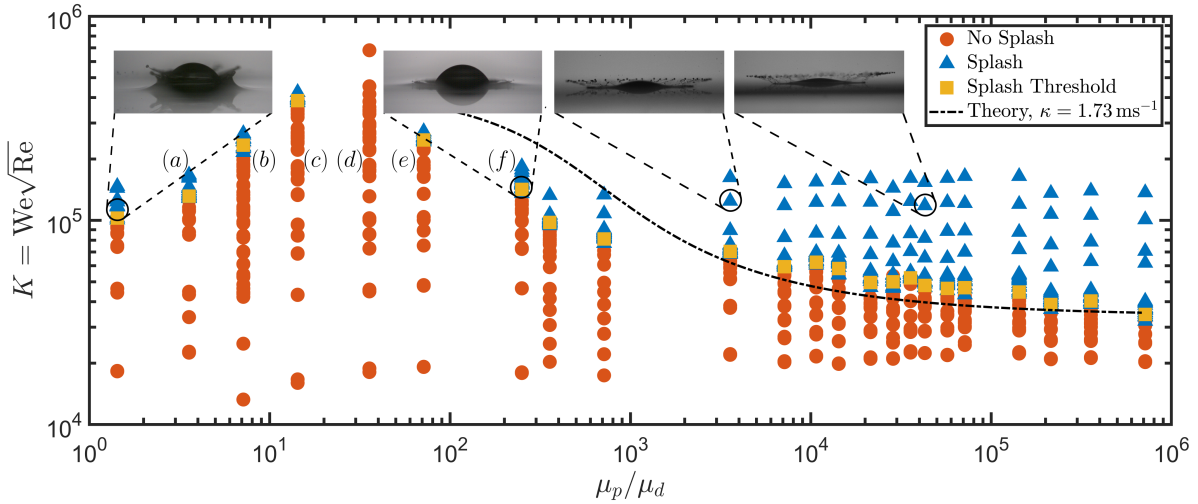

Figure 4: Regime diagram summarising the impact behaviour characterised by the splashing parameter K versus the pool to droplet viscosity ratio, delineating impacts that splash (blue triangles) from those that don't (orange circles), as well as the splashing threshold (yellow squares). For the case of a viscosity ratio of ∼35 no fall height available in the experimental setup resulted in splashing. The dot-dashed line corresponds to the solution to theoretical threshold from the solution of eq. (4) with a κ value of 1.73 ms^{-1}. The inset snapshots show examples of splashing at $K \sim 120{,}000$ for four different viscosity ratios. Representative video supplementary material is also provided. The (a)-(f) labels correspond to the plots in Fig. 5. Note the logarithmic scale on both axes.

Next we turn our attention to a quantitative discussion of the jet composition and how this

relates to which fluid contributes to the splash. We will also expand upon the discussion of the jet composition in [18] in view of the generalised setup herein. As noted in section 3, the DNS platform allows us to extract the interfaces of the three different phases. This enables us to identify the jet region and the contribution of each fluid to it, as illustrated in Fig. 3. We perform a systematic investigation of the jet composition across several different pool viscosities as a function of time during the impact process. We restrict ourselves to pool viscosities of up to 350 cSt (corresponding to a pool to droplet viscosity ratio of 242.75), given the already large scale physical property contrast between the pool and surrounding gas, encompassing between them several orders of magnitude in this key parameter. We note however that from the experimental videos we can see that above this viscosity there is no significant phenomenological change in the impact process. Consequently we now limit ourselves to pool viscosities within the range $5 - 350$ cSt, as denoted by the points (a)-(f) in Fig. 4. In each case the impact is characterised by a K value of 165,000. We present these results in Fig. 5, where we plot the percentage of the jet from each of the fluids (pool and droplet) against the simulation time for several pool viscosities. We note here that $t = 0$ corresponds to the theoretical time of contact between the droplet and pool if neither deformed and that the white area at early times in all cases corresponds to the time before which the jet has formed (which is a largely constant value across all of the viscosities).

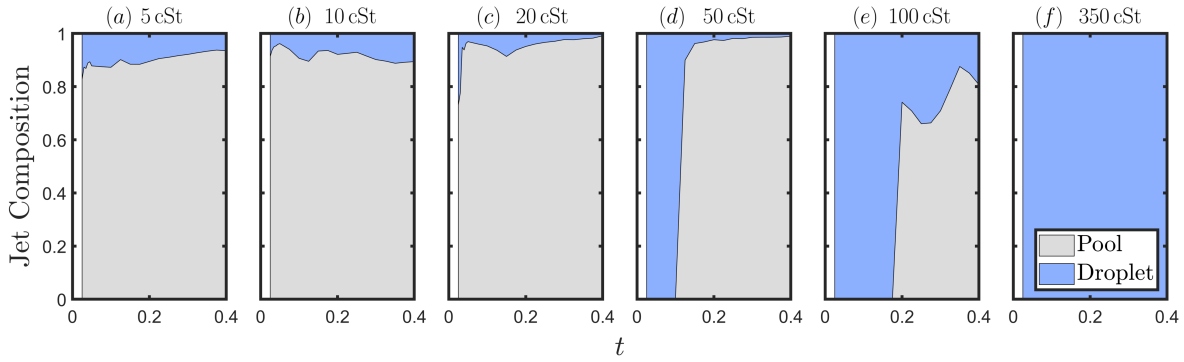

Figure 5: Post-impact jet composition versus time for impact cases described by $K = 165{,}000$ onto pools characterised by viscosities of 5, 10, 20, 50, 100 and 350 cSt, respectively. Here $t = 0$ corresponds to the theoretical time of impact if neither the pool nor the droplet were to deform pre-impact. The white area at early times in each case depicts the time interval during which the jet has not yet formed.

From the plot we can see the clear trend that as the viscosity ratio increases, a progressively larger proportion of the jet originates from the droplet compared to the pool. This agrees with our earlier observation and intuition that a more viscous pool will deform less prominently and thus contribute less fluid into the jet. We notice that for the 5, 10 and 20 cSt viscosity pools the jet is almost entirely composed by fluid coming from the pool across all times. By contrast, for 50 and 100 cSt viscosity pools we identify a transition in which at early times the jet is entirely composed of droplet fluid, but then at later times contributions from the pool also begin to materialise. Comparing the 50 and 100 cSt pool viscosity cases we can see that this transition happens at a later time and with a smaller amount of pool liquid inside the jet. Finally, we find that when the pool viscosity is 350 cSt, the jet contains only fluid from the droplet, with the impact region acting more similar to a (weakly) compliant solid. The plots in Fig. 3 shed more light into the morphological features of the interfaces during this dynamics. The top row corresponds to the 5 cSt pool, where we can see that the droplet contributes to the upper portion of the jet, with significant deformation of the pool. The bottom row illustrates the 350 cSt pool, where we only observe a slight rising of the pool surface at the location of the jet root but the

dynamics itself consists simply of a droplet spreading on the pool surface. This indicates good qualitative agreement to the results of Marcotte *et al.* [18], who show similar simulation profiles in their Figure 2.

Our earlier experimental observation on the source of the splash coming from the pool for $\mu_p/\mu_d < 35$ and from the droplet for $\mu_p/\mu_d > 35$ is thus reinforced by the above analysis and cross-comparison between experimental and numerical findings, as well as recent results from the literature. In what follows we aim to provide a mechanistic explanation of the above, providing predictive capabilities beyond the specific parameter regimes discussed previously.

5. Theoretical approach

We now provide a theoretical model for the two different splashing threshold trends identified in Section 4 and attempt to derive models quantifying them. We consider both the high viscosity region ($\mu_p/\mu_d > 35$) where the splash comes from the droplet and the threshold to splash decreases with pool viscosity, as well as the low viscosity region ($\mu_p/\mu_d < 35$) where the splash comes from the pool and the threshold to splash increases with pool viscosity, as they are phenomenologically unique.

First we consider the high viscosity case, which shares similarities to the scenario in which the threshold to splash on a soft solid decreases as the solid becomes more firm [25]. Following Howland *et al.* [25], we explain this by first noting that as the pool viscosity increases the displacement decreases and the peak pressure in the droplet increases. Figure 6 shows the peak pressure inside the droplet as a function of time for simulated impact scenarios with a constant K value of $165,000$ and for several different pool viscosities. From the figure we identify the overall trend that increasing the pool viscosity increases the peak pressure in the droplet, as well as the maximum value in time of this maximum pressure. We also observe that at the time of impact the maximum pressure occurs at the centre of the droplet, but as the impact progresses and the droplet begins to spread out, the maximum moves with the contact line peaking with the formation of the jet, and decreasing thereafter. This holds for both high viscosity pools where the jet is formed with fluid from the droplet and low viscosity pools where the pool is the main contributor to the jet composition. Figure 7 (a) illustrates experimental snapshots revealing the faster spreading of the jet for higher viscosity pools, which is consistent with the hypothesis that the pool deformation reduces the pressure driving the jet, causing it to form more slowly as the pool deformation is enhanced at lower viscosities.

A significant feature is that for pool viscosities less than 100 cSt there is little variation in the peak droplet pressure with viscosity, but above this viscosity value we begin identifying noticeable increases in the peak droplet pressure with larger pool viscosities. As this viscosity of 100 cSt corresponds to the region in our parameter space where splashing from the droplet is observed, we believe therefore that this corresponds to the threshold peak pressure in the droplet that must be exceeded in order for prompt splashing to occur.

We can however provide an explanation for the reduction in the peak pressure. As noted by Howland *et al.* [25], we can use arguments stemming from Wagner theory [14] to find that the peak pressure in the droplet is given by $p_{\mathrm{max,d}}^{\mathrm{Wagner}} = 3\rho_d V_0 R/8\delta t$, where δt is the of time between sheet ejection (when the pressure reaches a maximum) and theoretical impact if neither droplet or pool deformed. We justify the use of this result by considering Fig. 7 (b), specifically the inset, in which we depict the early time motion of the jet as being very well predicted by the use of Wagner theory estimates within their expected range of applicability. We note however that this result originally comes from impact onto a solid surface and therefore we transform it into

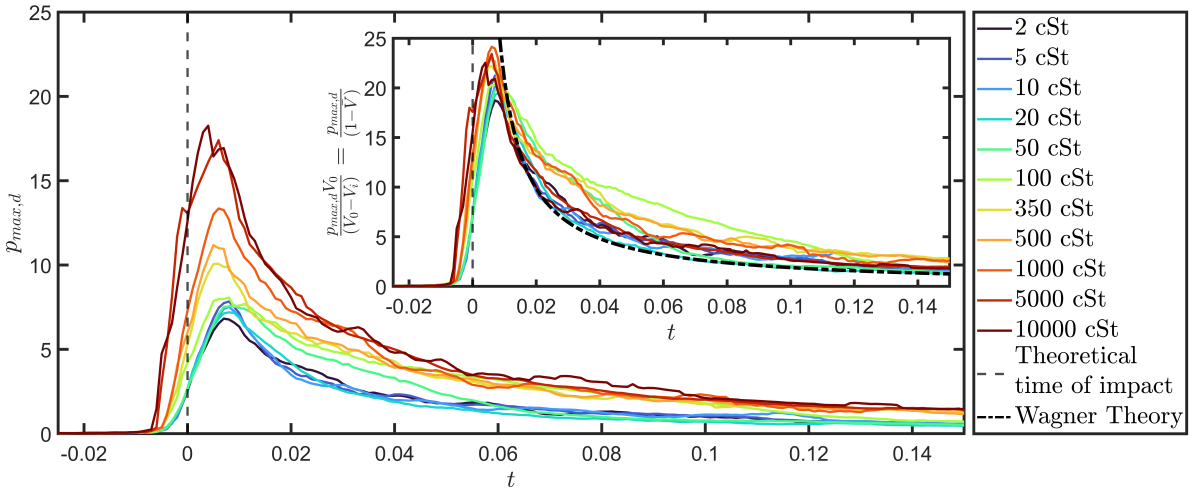

Figure 6: Droplet peak pressure against time for several different pool viscosities (direct numerical simulation data). In each case the key impact parameter is $K = 165{,}000$ and $t = 0$ corresponds to the theoretical time of impact if neither droplet nor pool deformed. (Inset) The same pressure is normalised by $\frac{V_0}{(V_0-V_i)} = \frac{1}{(1-\bar{V})}$, where $\bar{V}$ is the velocity of the common droplet-pool interface [19].

the velocity that the droplet actually sees as $V_0 - V_\mathrm{i}$, where V_i is the speed of the droplet-pool interface, which is the relative velocity of the droplet into the pool.

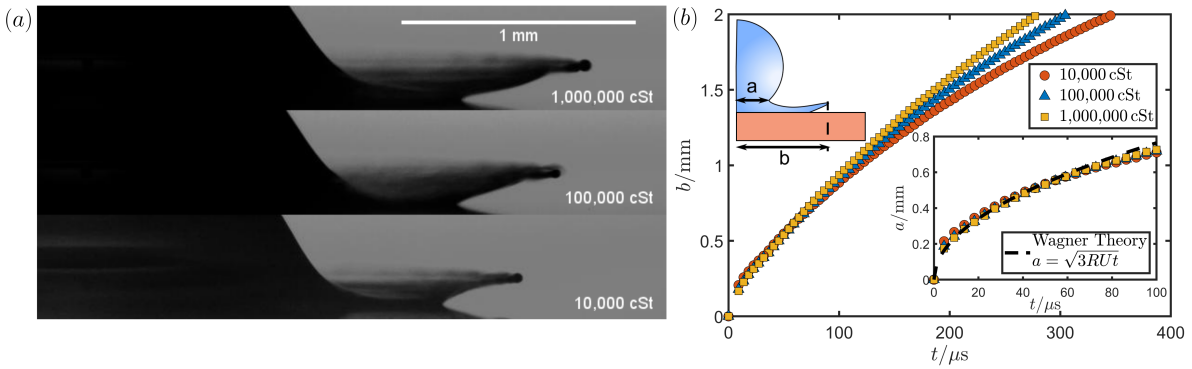

Figure 7: (a) Snapshots of 1.6 mm diameter FC-770 droplets impacting onto silicone oil pools at 2.5 ms^{-1}, taken at 300 μs post-impact (video supplementary material also included). (b) Measurement of the spreading distance of the tip of the jet (main figure) and the root of the jet (lower inset) as defined in the upper inset. In the case of the jet root location the result predicted by Wagner theory is also included.

In order to determine this relative velocity we use the result derived by Fudge *et al.* [19] to find the pool velocity, resulting in $V_0 - V_\mathrm{i} = V_0(1 - \bar{V})$, where $\bar{V} = V_\mathrm{i}/V_0$ is the normalised common interface penetration velocity given by

$$\bar{V} = \frac{1}{\sqrt{1 + A\rho_r + \frac{C}{\mathrm{Re_d}}\mu_r}}, \tag{1}$$

where the parameters A and C have values of 2.7096 and 24.3984, respectively. Figure 8 (a) illustrates the predictions obtained via eq. (1) extended to much higher viscosity ratios than previously explored in [19], as well as penetration velocities extracted from simulations indicating that the model remains valid even at these higher viscosities justifying its use here. Consequently, if we normalise the measured maximum pressure by dividing through by $\frac{V_0-V_\mathrm{i}}{V_0}$ we should recover the Wagner maximum pressure, which we would no longer anticipate to vary

with viscosity. In the inset of Fig. 6 we can visualise the normalised droplet maximum pressure versus time, showing a very good collapse of the curves across all values of the pool viscosity, as well as good agreement with the theoretical result predicted by Wagner theory (dash-dotted lines). Consequently we are now able to express the maximum pressure in the droplet in terms of the droplet and pool velocities, as well as Wagner pressure $p_{\mathrm{max,d}}^{\mathrm{Wagner}}$ as

$$p_{\mathrm{max,d}} = \frac{3\rho_d R(V_0 - V_i)}{8(t - t_0)} = \frac{V_0 - V_i}{V_0} p_{\mathrm{max,d}}^{\mathrm{Wagner}}. \tag{2}$$

The expression above may also be used to explain the decrease in the splashing threshold for high pool viscosities. As in Howland *et al.* [25], we ascertain that for splashing to occur we require the maximum pressure in the droplet to exceed a threshold value, p_{T}. For splashing we therefore require $p_{\mathrm{max,d}} \gtrsim p_{\mathrm{T}}$ and, using eq. (2) and the expression for the maximum Wagner pressure, leads to

$$V_{0,T} - V_i = V_{0,T}(1 - \bar{V}) \gtrsim \frac{8 p_T \delta t}{3\rho_d R}, \tag{3}$$

where $V_{0,T}$ denotes the threshold droplet impact velocity to splash. Equation (3) indicates that in order to splash we require the droplet impact velocity relative to the pool to exceed a threshold value given by $\frac{8p_T\delta t}{3\rho_d R}$, which we hereafter denote as κ. This is consistent with impact onto a solid surface, where V_i would be zero, and we would simply require the droplet impact speed to exceed a given threshold. We note that in eq. (3) the right hand side is a constant and the left hand side depends on the droplet impact speed and pool viscosity (via $\bar{V}$). We can therefore use this equation to find the threshold impact speed to splash for a given viscosity ratio. Using the equation for the penetration velocity (1) results in

$$V_{0,T}^3 \left[\rho_d D(A^* - 1)\right] + V_{0,T}^2 (C\mu_d\mu_r - 2\kappa\rho_d D A^*) + V_{0,T}(\kappa^2 \rho_d D A^* - 2\kappa C \mu_d \mu_r) + \kappa^2 C \mu_d \mu_r \gtrsim 0, \tag{4}$$

where $A^* = 1 + A\rho_r$ and C come from the penetration velocity given by eq. (1), μ_d is the droplet viscosity, μ_r the pool to droplet viscosity ratio and κ is the required excess speed as above. The selection of the correct root in the cubic equation relies, in first instance, on excluding the one (non-physical) negative root arising within our parameter space. Differentiating between the two remaining positive values is then supported by physical arguments, with the larger of the two roots decreasing in value with the pool viscosity increases being consistent with experimental data.

If we briefly consider the distinguished limit scenario of the pool viscosity tending to infinity, we recover the equation $V_{0,T}^2 - 2\kappa V_{0,T} + \kappa^2 \gtrsim 0$, which has the solution of $V_{0,T} > \kappa$, as we expected above. In order to use this equation we need a value of κ and therefore require estimates for the threshold pressure to splash and the time of sheet ejection. For the threshold pressure we can use the result by Howland *et al.* [25] and note that a pressure of 93 kPa was consistent with their findings and also with the pressures in the droplet measured in this work. To retrieve the jet ejection time we performed experiments and found a consistent value of $\sim 30\,\mu$s across several pool viscosities, again consistent with the framework of impact onto soft solids [25]. We do note however that using these values for p_T and δt leads to κ of $\sim 5\,\mathrm{ms}^{-1}$, which is far larger than the expected threshold speed for impact onto a solid surface. One possible explanation for this discrepancy is that the small time interval describing these dynamics in the experiments at these high speeds (approximately seven frames) makes the accurate determination of the impact time and first appearance of the sheet very challenging. This is exacerbated by the region of interest being obscured by the bulk of the droplet and pool (due to the intrinsic three-

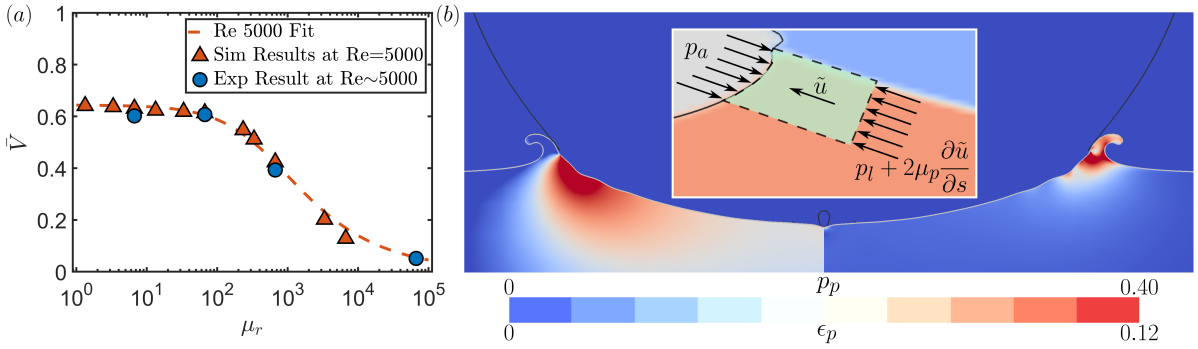

Figure 8: (a) Droplet-pool interface velocity versus the pool to droplet viscosity ratio for an impact with Re = 5000, showing both simulation and experimental results which validate the use of the theoretical prediction from eq. (1) in this higher viscosity regime (the viscosity range is considerably extended from that in [19]). (b) Pool pressure (left hand side) and viscous stress (right hand side) for the case of the impact of a FC-770 droplet impacting onto a 20 cSt silicone oil pool at Re = 6660 and $t = 0.1$ dimensionless time post-impact, showing that the peak pressure and viscous dissipation are both concentrated at the root of the jet. The inset highlights the region around the jet root before its formation, showing the direction of the jet forming velocity $\tilde{u}$ as described in the main text, as well as a control volume (in green) showing the forces acting on it (where the subscripts a and l refer to the air and liquid respectively). Note here the colouring simply distinguishes the different phases. Note that illustrated quantities have been restricted to the pool for visual emphasis, and also the different (non-dimensional) scales for the two measures.

dimensional geometry of the interfaces), meaning that this value of $\sim 30\,\mu$s is thus more likely to be considered an upper bound on the possible ejection time. Comparing to the data-rich simulations however, we observe a much smaller time to ejection of $\sim 10\,\mu$s, resulting in an excess speed of $1.73\,\mathrm{ms}^{-1}$, a value much closer to the observed splashing threshold for impact onto a solid surface which we find as $\sim 1.55\,\mathrm{ms}^{-1}$ for the Fluorinert droplets used here. Figure 4 includes the result of this theoretical argument with an excess speed of $1.73\,\mathrm{ms}^{-1}$, indicating very good agreement with the data especially at higher pool viscosities. The observed difference at lower pool viscosities could be attributed to the droplet-pool interface not immediately reaching the (now higher) penetration velocity. Thus the impact is actually slower and so the pressure damping is slightly less than predicted, resulting in an overestimation of the splashing threshold in this region of the parameter space.

We now focus further on the low pool viscosity section of the parameter regime, where we see splashing from the pool with an increase in the splashing threshold as the pool viscosity increases. As previously noted, Fig. 6 illustrates how for low pool viscosities the peak pressure in the droplet upon impact is largely unchanged (see variations up to 100 cSt) and thus it will not have an effect in this case. Therefore we turn our attention to the pressure inside the pool and how it affects the splashing behaviour. Firstly we underline that, based on experimental observation and analysis, the pool splashing is predicated on the formation of a jet (largely of pool fluid for low viscosities as shown in Fig. 5) from which the splash derives. From our experiments and simulations we can see that as the pool viscosity increases the jet becomes thicker and slower, and is therefore less likely to pinch off and eject a droplet (i.e. splash), which qualitatively explains why increasing the pool viscosity makes splashing less likely. We therefore concentrate in understanding the mechanism underlying the formation of this jet and in particular how it depends on the pool viscosity. As presented on the left hand side of Fig. 8 (b), similar to the maximum pressure in the droplet occurring at the root of the jet, the maximum pressure in the pool also occurs at the root of the jet and it is this pressure which is driving the jet formation. We also note that, as is the case in the droplet, the value of the maximum pressure inside the pool does not vary significantly for pool viscosities less than

100 cSt which is demonstrated in Fig. 9 (a). Thus the driving force behind the jet production is largely constant in this case and it must be the opposing force that is varying with the pool viscosity.

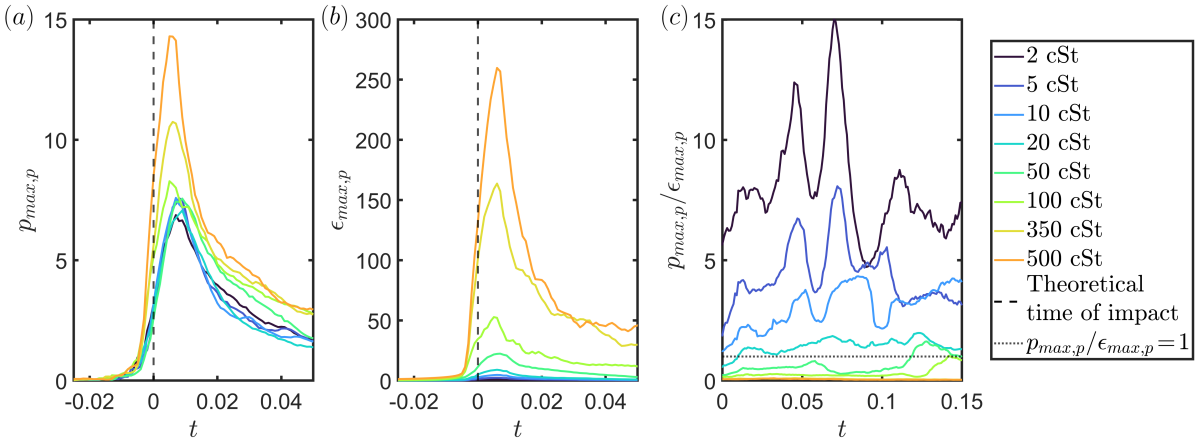

Figure 9: Numerically obtained (a) peak pressure and (b) viscous stress inside the pool versus time for several different pool viscosities. (c) The ratio of the peak pressure to the viscous stress, noting that for jet formation we expect this ratio to be greater than unity (marked by a dotted line). In each case the impact is characterised by a splashing parameter $K = 165{,}000$, and $t = 0$ corresponds to the theoretical time of impact if neither droplet nor pool deformed. These points consist of a subset of those in Fig. 6 with a consistent colour scheme. Note the different scale on the $y-$axes.

We consider the force opposing the jet formation to be the viscous stress, and approximate it as $2\mu_p \frac{\partial \tilde{u}}{\partial s}$, where $\tilde{u}$, shown in the inset in Fig. 8 (b), is the velocity in the direction of the jet formation s. As before, we assume that due to the largely constant penetration velocity in relation to changes in pool viscosity, this derivative should also be largely constant when considering different pool viscosity impact scenarios. We also note that this derivative has a negative value and thus the force from the viscous stress will be, as expected, acting in the negative s direction (i.e. in the opposite direction to the arrow in the inset in Fig. 8 (b)). Thus we hypothesise that the viscous stress varies linearly with the pool viscosity, an observation that is consistent with the data in Fig. 9 (b). This explains why the splashing threshold increases as the pool viscosity increases in this regime as the force driving the splash is largely constant, whereas the one opposing it is increasing (largely linearly) with the pool viscosity. We also observe that the maximum viscous stress occurs at the root of the jet, mirroring the position of the peak pressure inside the pool (right hand side of Fig. 8 (b)). This leads to the condition of a jet needing to form in order to support the splashing mechanism, for which we require the peak pressure in the pool to exceed the peak viscous stress. Figure 9 (c) shows the ratio of the peak pressure to stress from which we identify that for the lower pool viscosities the peak pressure is consistently greater than the viscous stress. By contrast, for pool viscosities $\gtrsim 50$ cSt the peak pressure is largely less than the viscous stress, cases for which we do not see a formation of a pool jet.

These results verify our conjecture that the increase in the splash threshold for low pool viscosities is due to the increase in the viscous stress in the pool at the root of the jet, impeding its formation and slowing it down leading to a decreased tendency to splash. The simulation results indicate that the viscous stress starts to exceed the maximum pressure at a pool viscosity of approximately 50 cSt, which is when we no longer observe crown splashing from the pool in the experimental data.

Combined with the above results for the high viscosity pool cases, we have explained the

observed trends in the splashing threshold across all the tested pool viscosities. Furthermore, by using the prediction for the velocity of the droplet-pool interface [19], we have quantified the effect of the pool motion and how the splashing threshold thus varies.

6. Concluding remarks

We have systematically examined the immiscible impact of liquid droplets onto deep viscous pools across several orders of magnitude of viscosity ratio. Both imaging and computational capabilities required to conduct rigorous studies for multi-fluid impingement scenarios have only been developed in recent years, inspired by the need to understand natural phenomena and industrial applications such as environmental disaster mitigation after oil spills [16, 30] or inkjet printing [31–33]. Drop impact onto immiscible liquid layers is a topic that has attracted recent interest [3, 8], however, these works have been limited to describing phenomenological aspects of the problem, providing important but limited explanations regarding the underlying physical mechanisms controlling the post-impact dynamics. Thus far, efforts have been concentrated either on gentler, often capillary-dominated interfacial flow regimes [34–36], or in simplified fluid property formulation contexts [18]. The present study represents a first comprehensive incursion into a previously inaccessible and rich parameter regime. From this investigation we have observed a non-monotonic response of the splashing threshold against the viscosity ratio. For low viscosity ratios ($\mu_p/\mu_d < 35$) increasing the pool viscosity increases the threshold to splash, and in these cases the main contribution to the ejected liquid sheet originates from the pool. For higher viscosity ratios ($\mu_p/\mu_d > 35$) increasing the pool viscosity decreases the splashing threshold, and in these cases the splash sheets originate from the droplet, consistent with recent studies [17, 18]. Interestingly, for a narrow intermediate regime found at $\mu_p/\mu_d \approx 35$, no splashing could be observed under conditions attainable in our laboratory, nor in our computational campaign. A specialised direct numerical simulation implementation has strengthened our experimental investigations, providing further insight into the underlying motion of both fluids. From these numerical results we have quantified how the different fluids contribute to the jet composition, and therefore the splash, across different velocities, allowing us to interpret the observed experimental results. We have quantified the resulting liquid jet composition in detail, with impact onto low pool viscosities leading to jets consisting mostly of pool fluid ($\approx 80-90\%$ for $\mu_p/\mu_d < 35$), while impact onto high pool viscosities can lead to the jet being entirely composed of fluid coming from the droplet. We also explained the cause for the decrease in splash threshold for high pool viscosities through a mechanism extending the arguments of Howland *et al.* [25]. Using a rigorous asymptotic approach aided by detailed numerical data, we found that the pool deformation at lower pool viscosities causes a reduction in the maximum pressure in the droplet, suppressing the splash. Using recent results by Fudge *et al.* [19] has allowed us to quantify this reduction and provide a compact and readily employable theoretical framework which has proven remarkably robust over large sections of the parameter space in this multi-fluid system. The resulting cross-methodological approach has generated new predictive capabilities not only in assessing primary impact features in vast three-phase flow parametric settings, but also in providing insight into splash sheet formation and eventual break-up into secondary droplets, all of key importance in the context of technological applications.

Declaration of competing interest

The authors declare that they have no known competing financial interests or personal relationships that would have influenced the body of work reported in this submission.

Funding acknowledgement

AACP thanks the Royal Society support through the University Research Fellowship (Grant No. URF\R\180016) & Enhancement Award (Grant No. RGF\EA\181002). RC and AACP gratefully acknowledge funding support from NSF/CBET-EPSRC grant EP/W016036/1. BF was supported by a Doctoral Training Award at the University of Oxford. For the purpose of Open Access, the author has applied a CC BY public copyright licence to any Author Accepted Manuscript (AAM) version arising from this submission.

Code accessibility

The direct numerical simulation implementation supporting the findings reported in this manuscript are openly available from the GitHub repository at `https://github.com/rcsc-group/DropImpactViscousPool`.

Appendix A. Supplementary material

Supporting video material pertaining to both experimental and computational exploration of this work is made available to the interested reader.

References

[1] E. Castillo-Orozco, A. Davanlou, P. K. Choudhury, R. Kumar, Droplet impact on deep liquid pools: Rayleigh jet to formation of secondary droplets, Physical Review E 92 (5) (2015) 053022.

[2] S. K. Das, A. Dalal, M. Breuer, G. Biswas, Evolution of jets during drop impact on a deep liquid pool, Physics of Fluids 34 (2) (2022) 022110.

[3] Z. Che, O. K. Matar, Impact of droplets on immiscible liquid films, Soft Matter 14 (9) (2018) 1540–1551.

[4] U. Jain, M. Jalaal, D. Lohse, D. Van Der Meer, Deep pool water-impacts of viscous oil droplets, Soft Matter 15 (23) (2019) 4629–4638.

[5] H. Lhuissier, C. Sun, A. Prosperetti, D. Lohse, Drop fragmentation at impact onto a bath of an immiscible liquid, Physical Review Letters 110 (26) (2013) 264503.

[6] G.-J. Michon, C. Josserand, T. Séon, Jet dynamics post drop impact on a deep pool, Physical Review Fluids 2 (2) (2017) 023601.

[7] V. Lherm, R. Deguen, T. Alboussière, M. Landeau, Rayleigh–taylor instability in impact cratering experiments, Journal of Fluid Mechanics 937 (2022).

[8] D. Roy, S. S. Rao, S. Basu, Droplet impact on immiscible liquid pool: Multi-scale dynamics of entrapped air cushion at short timescales, Physics of Fluids 34 (5) (2022) 052004.

[9] T. Tran, H. de Maleprade, C. Sun, D. Lohse, Air entrainment during impact of droplets on liquid surfaces, J. Fluid Mech. 726 (2013).

[10] L. Zhang, J. Toole, K. Fezzaa, R. Deegan, Evolution of the ejecta sheet from the impact of a drop with a deep pool, Journal of Fluid Mechanics 690 (2012) 5–15.

[11] M.-J. Thoraval, K. Takehara, T. G. Etoh, S. Popinet, P. Ray, C. Josserand, S. Zaleski, S. T. Thoroddsen, von kármán vortex street within an impacting drop, Physical Review Letters 108 (26) (2012) 264506.

[12] C. Josserand, S. Zaleski, Droplet splashing on a thin liquid film, Physics of Fluids 15 (6) (2003) 1650–1657.

[13] C. Josserand, P. Ray, S. Zaleski, Droplet impact on a thin liquid film: anatomy of the splash, Journal of Fluid Mechanics 802 (2016) 775–805.

[14] H. Wagner, Über stoß-und gleitvorgänge an der oberfläche von flüssigkeiten, ZAMM-Journal of Applied Mathematics and Mechanics/Zeitschrift für Angewandte Mathematik und Mechanik 12 (4) (1932) 193–215.

[15] R. Cimpeanu, M. Moore, Early-time jet formation in liquid–liquid impact problems: theory and simulations, Journal of Fluid Mechanics 856 (2018) 764–796.

[16] D. W. Murphy, C. Li, V. d'Albignac, D. Morra, J. Katz, Splash behaviour and oily marine aerosol production by raindrops impacting oil slicks, Journal of Fluid Mechanics 780 (2015) 536–577.

[17] H. M. Kittel, I. V. Roisman, C. Tropea, Splash of a drop impacting onto a solid substrate wetted by a thin film of another liquid, Physical Review Fluids 3 (7) (2018) 073601.

[18] F. Marcotte, G.-J. Michon, T. Séon, C. Josserand, Ejecta, corolla, and splashes from drop impacts on viscous fluids, Physical Review Letters 122 (1) (2019) 014501.

[19] B. D. Fudge, R. Cimpeanu, A. A. Castrejón-Pita, Dipping into a new pool: The interface dynamics of drops impacting onto a different liquid, Physical Review E 104 (6) (2021) 065102.

[20] C. Stow, M. Hadfield, An experimental investigation of fluid flow resulting from the impact of a water drop with an unyielding dry surface, Proceedings of the Royal Society of London. A. Mathematical and Physical Sciences 373 (1755) (1981) 419–441.

[21] C. Mundo, M. Sommerfeld, C. Tropea, Droplet-wall collisions: experimental studies of the deformation and breakup process, International Journal of Multiphase Flow 21 (2) (1995) 151–173.

[22] J. C. Bird, S. S. Tsai, H. A. Stone, Inclined to splash: triggering and inhibiting a splash with tangential velocity, New Journal of Physics 11 (6) (2009) 063017.

[23] J. Hao, J. Lu, L. Lee, Z. Wu, G. Hu, J. Floryan, Droplet splashing on an inclined surface, Physical Review Letters 122 (5) (2019) 054501.

[24] L. Xu, W. W. Zhang, S. R. Nagel, Drop splashing on a dry smooth surface, Physical Review Letters 94 (18) (2005) 184505.

[25] C. J. Howland, A. Antkowiak, J. R. Castrejón-Pita, S. D. Howison, J. M. Oliver, R. W. Style, A. A. Castrejón-Pita, It's harder to splash on soft solids, Physical Review Letters 117 (18) (2016) 184502.

[26] M.-J. Thoraval, K. Takehara, T. Etoh, S. T. Thoroddsen, Drop impact entrapment of bubble rings, Journal of Fluid Mechanics 724 (2013) 234–258.

[27] S. Popinet, Gerris: a tree-based adaptive solver for the incompressible Euler equations in complex geometries, Journal of Computational Physics 190 (2) (2003) 572–600.

[28] S. Popinet, An accurate adaptive solver for surface-tension-driven interfacial flows, Journal of Computational Physics 228 (16) (2009) 5838–5866.

[29] S. Popinet, A quadtree-adaptive multigrid solver for the Serre–Green–Naghdi equations, Journal of Computational Physics 302 (2015) 336–358.

[30] W. Wang, C. Ji, F. Lin, X. Wei, J. Zou, Formation of water in oil in water particles by drop impact on an oil layer, Physics of Fluids 31 (3) (2019) 037107.

[31] D. Lohse, Fundamental fluid dynamics challenges in inkjet printing, Annual Review of Fluid Mechanics 54 (2022) 349–382.

[32] S. D. Hoath, Fundamentals of inkjet printing: the science of inkjet and droplets, John Wiley & Sons, 2016.

[33] A. A. Castrejón-Pita, E. S. Betton, N. Campbell, N. Jackson, J. Morgan, T. R. Tuladhar, D. C. Vadillo, J. R. Castrejon-Pita, Formulation, quality, cleaning, and other advances in inkjet printing, Atomization and Sprays 31 (4) (2021).

[34] V. Sanjay, U. Sen, P. Kant, D. Lohse, Taylor–Culick retractions and the influence of the surroundings, Journal of Fluid Mechanics 948 (2022) A14.

[35] V. Sanjay, S. Lakshman, P. Chantelot, J. H. Snoeijer, D. Lohse, Drop impact on viscous liquid films, Journal of Fluid Mechanics 958 (2023) A25.

[36] Z. Yang, B. Ji, J. T. Ault, J. Feng, Enhanced singular jet formation in oil-coated bubble bursting, Nature Physics (2023) 1–7.

Statement of Authorship for joint/multi-authored papers for PGR thesis

To appear at the end of each thesis chapter submitted as an article/paper.

The statement shall describe the candidate's and co-authors' independent research contributions in the thesis publications. For each publication there should exist a complete statement that is to be filled out and signed by the candidate and supervisor **(only required where there isn't already a statement of contribution within the paper itself).**

Title of Paper:	Drop splashing after impact onto immiscible pools of different viscosities
Publication Status	▪ Submitted for Publication
Publication Details	Fudge, B.D., Cimpeanu, R., Antkowiak, A., Castrejón-Pita, J.R. and Castrejón-Pita, A.A. Drop splashing after impact onto immiscible pools of different viscosities. In submission

Student Confirmation

Student name:	Benjamin David Fudge
Contribution to the paper	Lead Author, performed all experiments, except those in Figure 7, and numerical simulations, analysed and presented results, jointly performed theoretical modelling, and writing and editing of manuscript
Signature: 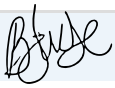	**Date: 09/12/2022**

Supervisor Confirmation

By signing the Statement of Authorship, you are certifying that the candidate made a substantial contribution to the publication, and that the description described above is accurate.

Supervisor name and title: Prof. Alfonso A. Castrejon-Pita	
Supervisor comments: Benjamin D. Fudge led and carried out the research contained in this chapter/article. Other authors provided formal supervision (AACP, RC) and informal supervision (JRCP, AA) and funds to carry out the research.	
Signature: 	**Date: 09/12/2022**

5

Droplet Splashing on Curved Substrates

Contents

5.1 Introduction

In this chapter we present the paper *"Droplet Splashing on Curved Substrates"* published in the Journal of Colloid and Interface Science. Here we investigate the impact of droplets onto smooth solid surfaces of different curvatures, both convex spheres and concave lenses. Whilst previous results in the literature have produced conflicting results for the effect of the curvature on the splashing threshold, in this work we find a consistent trend for both cases, i.e. that increasing positive curvature increases the threshold to splash. This corresponds to smaller spheres requiring higher impact speeds to splash, and similarly more curved concave lenses require lower speeds to splash. Whilst previous works have quantified the results in terms of the ratio of the radii of curvatures of the droplet and pool, these are often not consistent when the droplet size varies. Here we show that the relative effects of

changing either of these values has the same effect (i.e. both an increase in the droplet size or radius of curvature of the substrate enhances splashing). Consequently we use a new combination of these parameters to accurately account for these changes.

We offer an explanation of these results by applying and adapting recently developed theories which incorporate the air flow around the spreading lamella post impact, and its effect on the splashing dynamics. We note how the curvature of the surface either allows the air flow to escape underneath the spreading droplet for a convex sphere, or becomes further confined for a concave lens. This curvature effect can then be quantified by the change in the wedge angle between the droplet and surface, which is an important factor in the splashing parameter. Through geometric reasoning and experimental results, we find a relationship between the substrate curvature and wedge angle, which when incorporated into the theory provides an excellent collapse of the data for all curvatures onto one threshold value.

Finally we also investigate the effect of asymmetric impacts between the droplet and surface. Whilst for impact onto flat surfaces the positioning of the droplet has no effect, in the case of curved surfaces there is now a spatial variation in the dynamics of the impact. Specifically we observe that when the impact is not at the centre of the surface, splashing is enhanced in the downwards direction (that is the one further from the surface centre), and suppressed (or at least reduced) in the upwards direction. We note that this result is somewhat analogous to findings in the context of impact onto inclined surfaces, previously reported in the literature, suggesting that a similar underlying mechanism is controlling the dynamics in both cases.

5.2 Publication: Sykes *et. al.* *"Droplet Splashing on Curved Substrates"* JCIS 2022

Journal of Colloid and Interface Science 615 (2022) 227–235

Contents lists available at ScienceDirect

Journal of Colloid and Interface Science

journal homepage: www.elsevier.com/locate/jcis

Droplet splashing on curved substrates

Thomas C. Sykes [a,*], Ben D. Fudge [a], Miguel A. Quetzeri-Santiago [b], J. Rafael Castrejón-Pita [c], Alfonso A. Castrejón-Pita [a,*]

[a] Department of Engineering Science, University of Oxford, Oxford OX1 3PJ, United Kingdom
[b] Mesoscale Chemical Systems Group, MESA+ Institute and Faculty of Science and Technology, University of Twente, Enschede 7500AE, The Netherlands
[c] School of Engineering and Materials Science, Queen Mary University of London, London E1 4NS, United Kingdom

GRAPHICAL ABSTRACT

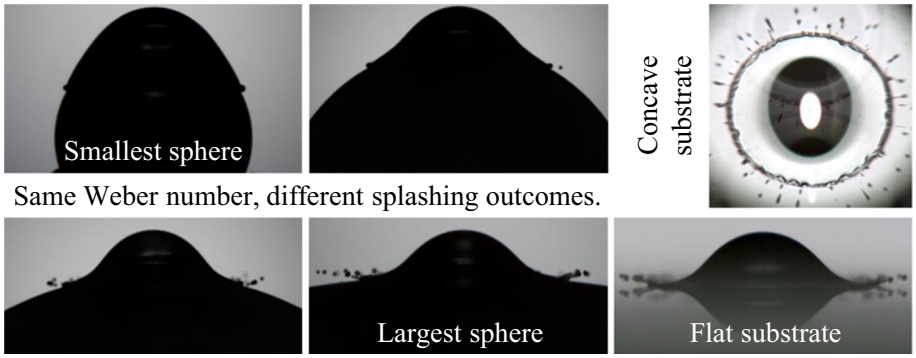

ARTICLE INFO

Article history:
Received 2 November 2021
Revised 20 January 2022
Accepted 21 January 2022
Available online 29 January 2022

Keywords:
Droplets
Splashing
Textured substrates
Wetting
Droplet impact

ABSTRACT

Droplets impacting dry solid substrates often splash above a certain threshold impact velocity. We *hypothesise* that substrate curvature alters splashing thresholds due to a modification to the lift force acting on the lamella at the point of breakup. We have undertaken high-speed imaging *experiments* of millimetric droplets impacting convex and concave surfaces to establish splashing thresholds and dynamics across a wide range of substrate geometries and impact conditions. Our *findings* indicate that the tendency of droplets to splash is proportional to the reciprocal of the substrate's radius of curvature, independent of whether the substrate is convex or concave, with it being harder for droplets to splash on small spheres. Moreover, we consistently parameterise the axisymmetric splashing threshold across all curved substrate geometries via a modification to the well-known splashing ratio. Finally, the splashing dynamics resulting from initial asymmetry between the impacting droplet and curved substrate are also elucidated.

1. Introduction

Droplet impact onto solid substrates arises throughout industry and nature, which has motivated extensive work on the topic since the seminal work of Worthington in the 19th century [1]. Despite the resulting body of literature, droplet impact is still captivating scientists for its wide range of outcomes, from simple spreading

* Corresponding authors.
E-mail addresses: thomas.sykes@eng.ox.ac.uk, t.c.sykes@outlook.com (T.C. Sykes), castrejon@cantab.net (J.R. Castrejón-Pita), alfonso.castrejon-pita@wadham.ox.ac.uk (A.A. Castrejón-Pita).

https://doi.org/10.1016/j.jcis.2022.01.136
0021-9797/

and deposition to bouncing and splashing (i.e. droplet fragmentation) [2,3]. The parameters governing the physics of impact, including droplet properties, substrate characteristics (including wettability and temperature), and the ambient pressure, are broad and intricately linked, with many playing pivotal roles in the resulting dynamics [4–11]. Droplet impact phenomena have been traditionally characterised via the Weber, $We = \rho u^2 l/\sigma$, and Reynolds, $Re = \rho u l/\mu$, numbers, where μ, σ, ρ, u, and l are the droplet's dynamic viscosity, surface tension, density, impact velocity, and a characteristic length scale (typically the droplet diameter), respectively. In this context, simple deposition typically occurs at low Weber and Reynolds numbers. In contrast, at sufficiently high Weber and Reynolds numbers, an impacting droplet splashes, breaking-up into secondary droplets (satellites).

Understanding the conditions under which splashing occurs is of utmost importance in applications including spray processes, forensic science, and inkjet printing [3]. In many cases, research and development aims to prevent fluid misting and the formation of smaller droplets with indiscriminate trajectories, both of which can affect finish quality and aerosolise potentially-hazardous fluids [12]. Whilst past works have mainly focused on droplets impacting flat surfaces, some natural and industrial applications see droplets impacting concave or convex substrates instead, including individual spherical particles. Examples of these processes include spray drying, rain-induced icing, and the inkjet printing of a binder on powder beds for additive manufacturing [13,14]. Notably, inkjet printing applications are seeking to expand into textured surface markets, such as in the food industry, aerospace, and automotive.

Past works have demonstrated that droplets impacting a dry spherical target can produce at least seven distinct outcomes: deposition, rebound, coating, gravity disintegration, momentum disintegration, and splashing [13,15–17]. These outcomes are dependent on the impact velocity, liquid properties, substrate wettability, surface roughness (as for flat substrates [18]), and the sphere size relative to the droplet diameter. Most droplet impact studies on spheres have been conducted at moderate Weber numbers ($We < 100$), finding larger wetting areas on spherical substrates than on flat ones, for similar impact conditions [19–21]. Similarly, it has been shown that increasing substrate curvature (i.e. smaller spheres) leads to droplets spreading to a larger maximum spreading diameter, while also enhancing receding following maximum spreading [22,23]. In contrast, few studies have been conducted under the parameter range leading to splashing [e.g. 24–26], despite its practical significance [13]. Other studies have been focused on wet surfaces, which strongly influences impact outcomes [e.g. 27,28]. In fact, some of these works present contradictory results regarding the influence of the substrate curvature on splashing thresholds.

In this work, we study the effect of substrate curvature on the propensity of an impacting droplet to splash using high-speed imaging. Our experimental conditions cover a wide range of parameters, encompassing simple deposition through to corona splashing. Our experimental protocol (involving two high-speed cameras positioned perpendicularly to determine impact position) enables the transition between simple deposition and splashing to be precisely delineated across a range of curved substrates, including convex spheres (covering an order-of-magnitude wide range of diameters), a flat substrate, and concave surfaces. Moreover, by considering the effect of substrate curvature on the lift force acting on the lamella at the onset of splashing, we identify a potential mechanism underpinning the splashing threshold and propose a modification to the well-known splashing ratio [5,29] to account for the effect of substrate curvature.

2. Experimental method

Single ethanol droplets (density, $\rho = 785\ \mathrm{kg\ m^{-3}}$; surface tension, $\sigma = 22.2\ \mathrm{mN\ m^{-1}}$; dynamic viscosity, $\mu = 1.10\ \mathrm{mPa\ s}$ [30]) were impacted onto smooth untreated borosilicate-glass substrates. Ethanol strongly wets untreated glass, with a static contact angle of $(5 \pm 4)^\circ$, and a quasistatic advancing contact angle of $(20 \pm 3)^\circ$ [10,18]. These angles were measured using a polynomial fitting approach, as detailed in Ref. [31] (also see Fig. 1d). The contact line usually pinned at the maximum spread length, if achieved; the receding contact angle is close to 0°, implying a contact angle hysteresis of approximately 20°. Characterised by their apex radius of curvature, r_s, the substrates were eight convex spheres (Bearing Warehouse Ltd and Glass Sphere s.r.o.), covering an order-of-magnitude wide range of $r_s \in [2.0, 20.0]$ mm, two plano-concave lenses with $r_s \in \{-25.84, -12.92\}$ mm (KPC040 and KPC043, Newport), and a flat cover slip ($r_s \to \infty$). All substrates were thoroughly cleaned and dried between successive impacts.

Droplets were generated by dripping from a blunt-end dispensing tip (Metcal or Fisnar) at 15 μL $\mathrm{min^{-1}}$ using a syringe pump, until the pendant droplet detached due to gravity and fell vertically towards the substrate. Two dispensing tip sizes (22 and 25 gauge) were used interchangeably to adjust droplet volume; the distance between the dispensing tip and substrate apex was varied (180 mm–400 mm) to adjust the impact velocity, $u \in [1.77, 2.58]\ \mathrm{m\ s^{-1}}$, as measured using an in-house MATLAB script. Impact velocities were selected to comprehensively span the splashing threshold of each substrate. As noted by other authors for millimetric droplets generated by dripping (e.g. Ref. [32]), oscillations in the free surface of the falling droplets meant that they were not necessarily spherical on impact, whilst it is known that droplet shape influences splashing [33]. These oscillations were accounted for by measuring the radius of curvature of the bottom of the droplet, r_c at the point of impact (see the solid part of the droplet's edge in Fig. 1a). We take $l = 2r_c$ as the characteristic length scale to approximate the effective diameter of the droplet for the purposes of splashing (e.g. $We = \rho u^2 \cdot 2r_c/\sigma$). For a typical experiment (oblate droplet), r_c was generally 5% greater than the equivalent spherical radius, with variations in r_c around 4% for a fixed droplet volume – see §1 of the Supplemental Material for details. In this work, $We \in [237, 539]$, $Re \in [2544, 4221]$, and $Oh = \sqrt{We}/Re = \mu/\sqrt{\rho\sigma l} \in [5.3 \times 10^{-3}, 6.1 \times 10^{-3}]$.

The dispensing tips and substrates were attached to manual translation and elevation stages, providing each with independent 3-axis motion, enabling the impact position to be varied and axisymmetry between the droplet and substrate to be ensured when desired. All impacts were simultaneously imaged using two high-speed cameras positioned perpendicularly, in a shadowgraphy setup. For the convex substrates, both cameras were focused on the apex of the sphere, as seen in Fig. 1b (not to scale; similarly for the flat substrate). One camera, either a Phantom TMX 7510 or v2512 recording at 25,000–110,000 frames per second (fps), was principally used to image the droplet geometry and impact dynamics with an 105–199 pixels $\mathrm{mm^{-1}}$ effective resolution. The second camera, either a Phantom v12.1 or Miro LAB310 recording at up to 11,000 fps, with 34–99 pixels $\mathrm{mm^{-1}}$, gave a wider view of the dynamics. The two cameras together enabled the impact point in the horizontal plane of a top-down view to be precisely determined. Further technical details of the experiment are provided in §2 of the Supplemental Material. Also described there is a modified setup used for the concave surfaces, where the higher-speed camera imaged the splashing dynamics through the bottom of the substrate via a mirror.

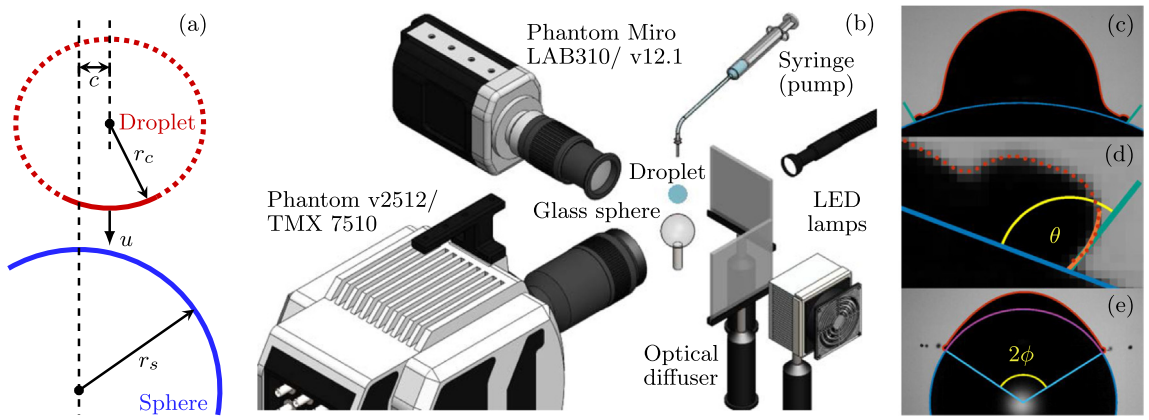

Fig. 1. (a) A sketch of droplet impact onto a convex substrate (sphere), labelled with pertinent geometric variables and impact velocity. c refers to the radial offset in a 2D horizontal plane of the substrate and droplet's vertical axes of symmetry; zero offset out of the plane of the figure is assumed here. Axisymmetric impact implies that $c \approx 0$, as in Sections 3.1 and 3.2. (b) A sketch of the accompanying experimental setup. (c)–(e) Image-processed frames: red points represent detected edge pixels; orange line indicates the fitted polynomial; green lines are tangent to the free surface at the contact point.

For convex substrates, the dynamic contact angle, θ was measured for all times $t > 0$ ($t = 0$ on impact) using a polynomial fitting approach, as seen in Figs. 1c and 1d [31]. The orange line in Fig. 1d represents the fitted polynomial; the green line represents the tangent to the polynomial at the contact point, from which θ is measured relative to the tangent to the sphere's surface. The angle subtended by the radial lines to the contact points at the centre of the sphere, 2ϕ and the spread length (purple line) were also measured – see Fig. 1e.

3. Results and discussion

3.1. Splashing propensity and dynamics

For fixed $\mathrm{We} = 414 \pm 2$ ($\mathrm{Re} = 3533 \pm 35; \mathrm{K} = \mathrm{We}^{1/2}\mathrm{Re}^{1/4} = 157 \pm 1$), Fig. 2 (and the accompanying videos) demonstrates that the splashing propensity of a $(3.79 \pm 0.08)\mu$L droplet impacting a sphere axisymmetrically depends strongly on substrate curvature, r_s. Note that τ represents dimensionless time ($\tau = 0$ on impact), with respect to the kinetic time scale, $2r_c/u$. Within our experiments, both prompt and corona splashing is seen. Solely for the classification of droplet impact outcomes, no distinction is made between prompt and corona splashing; any break-up of the droplet during the outward spreading phase is considered splashing[1]. Splashing is therefore seen for all $r_s \geqslant 3.0$ mm in Fig. 2, whilst the droplet simply spreads across the $r_s = 2.0$ mm sphere. The $r_s \in \{3.0, 4.0\}$ mm spheres show splashing behaviour akin to prompt splashing, whilst more comprehensive corona-like breakup is evident for $r_s \in \{7.0, 20.0\}$ mm. Indeed, corona splashing is known to occur for such impact conditions on smooth flat glass substrates (as seen in the bottom row of Fig. 2), which is far from the splashing threshold, just above which prompt splashing ensues. Hence, Fig. 2 substantiates the qualitative conclusion that it is harder for impacting droplets to splash on smaller spheres. Moreover, Fig. 2 qualitatively demonstrates that satellite trajectories, number and volume distributions vary on curved substrates for fixed impact conditions, further indicating the significant affect of substrate curvature on post-splashing dynamics that could be of interest in natural and industrial contexts, as previously elucidated for flat targets [35,36]. A detailed study of such post-splashing dynamics represents an excellent opportunity to extend this work.

[1] There are other mechanisms of secondary droplet formation, such as induced by a droplet spreading into a convex substrate's mount or over the rim of a concave substrate (as recently demonstrated by Ref. [34]) and gravity disintegration; these mechanisms are not considered as splashing here.

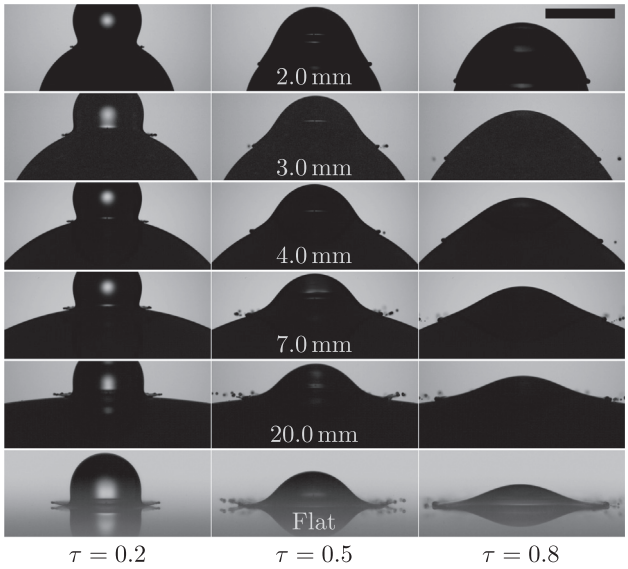

Fig. 2. Axisymmetric impact of fixed-volume ethanol droplets onto a selection of convex substrates, and a flat glass side (bottom row), at constant $\mathrm{We} = 414 \pm 2$. Substrate curvature, r_s, is indicated in the centre of each row. Times τ are dimensionless with respect to the kinetic time scale, $2r_c/u$. Normalised offset $c/r_c \ll 0.1$. The scale bar is 2 mm.

For a quantitative assessment of splashing thresholds, the splashing propensity of $(3.6 \pm 0.3)\mu$L droplets are presented as a regime map in Fig. 3a, in terms of the traditional splashing parameter $\mathrm{K} = \mathrm{We}^{5/8}\mathrm{Oh}^{-1/4} = \mathrm{We}^{1/2}\mathrm{Re}^{1/4}$, and the ratio of droplet to substrate curvature $\Omega = r_c/r_s$. The latter enables comparison to existing studies [28,26]. Defining c as the dimensional horizontal radial offset of the substrate and droplet's vertical axes of symmetry on impact (see Fig. 1a, where zero offset out of the plane of the figure is assumed), only $\Omega > 0$ experiments with $c/r_c < 0.15$ are plotted to ensure axisymmetry (cf. Section 3.3). The splashing threshold region for each substrate is defined as $\mathrm{K} \in [\mathrm{K}_l, \mathrm{K}_h]$, where $\mathrm{K}_l = \min(\mathrm{K})\,\forall\,\mathrm{K}$ showing splashing, and $\mathrm{K}_h = \max(\mathrm{K})\,\forall\,\mathrm{K}$ not exhibiting splashing. Individual experiments are plotted as separate points and coloured according to splashing outcome. Those points outside the threshold region are faded, with the vertical extent of the threshold region commensurate to the error in determining K. $\mathrm{K} \approx 127$ (black-dashed line in Fig. 3a) is the accepted splashing threshold for ethanol droplets impacting flat dry sub-

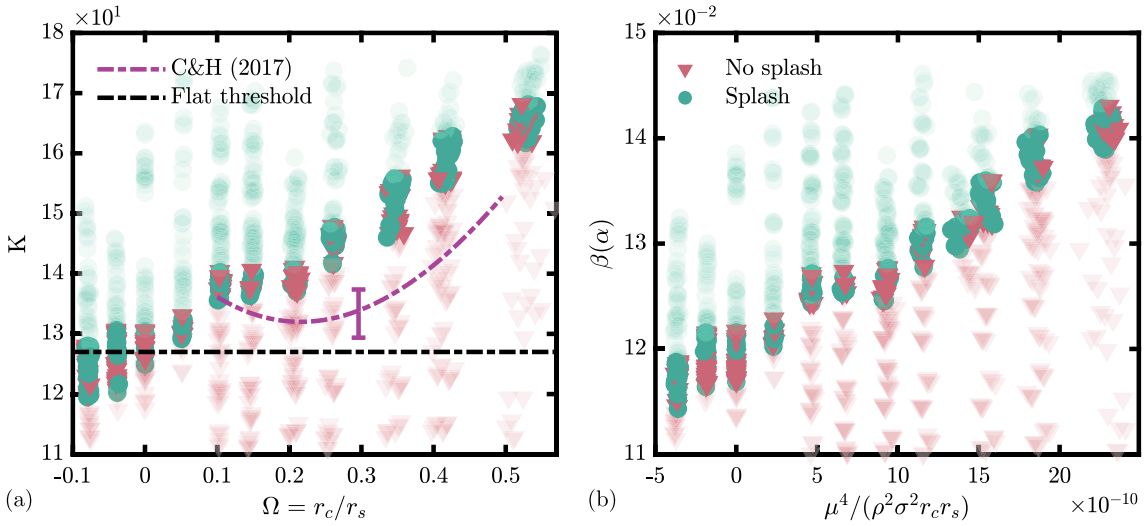

Fig. 3. Splashing propensity of (3.6 ± 0.3)μL droplets (originating from a 25 gauge dispensing tip) impacting convex ($r_s > 0$), concave ($r_s < 0$), and flat ($r_s \to \infty$) substrates, in terms of the splashing parameter $K = We^{5/8}Oh^{-1/4}$ and splashing ratio $\beta(\alpha)$. (4.85 ± 0.15)μL droplet data are also included in panel (b). All impacts are axisymmetric ($c/r_c < 0.15$ for $r_s > 0$ data). 'C&H (2017)' refers to the polynominal fit found in Ref. [26] for micrometric droplets with $\Omega \in [0.09, 0.55]$. The flat threshold of $K \approx 127$ is sourced from Refs. [37,10], which is consisten.t with our data.

strates (i.e. $r_s \to \infty$ and $\Omega = 0$) [37,10], which is consistent with our data.

$\Omega > 0$ for spheres, whilst $\Omega < 0$ for concave surfaces. Examples of impact dynamics on both concave substrates studied are seen in Fig. 4. In the first three rows, $We \in [302, 337]$ is varied on the $r_s = -12.92$ mm substrate. Interestingly, there are a similar number of satellite droplets for the two $We \in \{314, 337\}$ cases exhibiting splashing. Due to the satellite's shallower trajectory, more land back on the substrate for the $We = 314$ example (seen as long streaks in the $\tau = 0.6$ frames). We did not observe satellites landing on spheres of similar $|r_s|$ values: concave surfaces curve upwards to intersect the satellites' trajectories. Satellites that land within the maximum spread length of the primary droplet are able to recoalesce with it (see $\tau = 0.9$), which is significant from the point of view of applications wishing to avoid contamination resulting from splashing [12]. For fixed $We = 337$ (bottom two rows of Fig. 4), more satellites materialise on the substrate with greater $|1/r_s|$ (i.e. $r_s = -12.92$ mm, 3rd row of Fig. 4), and also appear to have a greater volume (with a greater potential for secondary breakup). These qualitative observations indicate that the trend in splashing propensity on spheres identified above continues into concave surfaces, which is quantitatively confirmed in Fig. 3a. Note that the $\Omega < 0$ data shown in Fig. 3a have been filtered according to the axisymmetry condition $c/r_c < 0.15$. However, there is additional uncertainty in the apex position relative to the droplet location on impact here. Nevertheless, the splashing dynamics are well separated and consistent for both concave examples.

Fig. 3a shows unique behaviour in comparison to the existing literature. Charalampous and Hardalupas (2017), herein 'C&H (2017)', considered the impact of micrometric droplets (diameter $[170, 280]$μm) onto dry spheres of three different diameters ($\{500, 1000, 2000\}$μm), with droplets continuously impinging at up to 20000 Hz [26]. The splashing threshold was found to be $We \approx 400$ for $0.09 < \Omega < 0.30$, and increased to $We \approx 450$ for $\Omega \approx 0.5$. Their polynomial fit describing the splashing threshold (extracted from figure 12 of C&H (2017), in terms of We) is plotted in terms of K with our data in Fig. 3a. Ω values are taken directly from the source, assuming that $Oh = 8 \times 10^{-3}$; the error bar represents uncertainty in $Oh \in [7.0 \times 10^{-3}, 8.9 \times 10^{-3}]$. The trend broadly agrees with our data for $\Omega > 0.3$, being only one or two

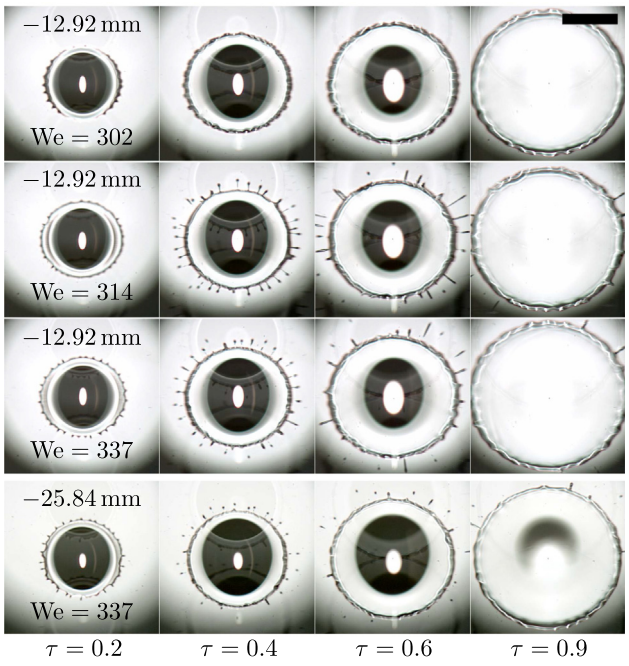

Fig. 4. Axisymmetric impact of ethanol droplets onto a selection of concave surfaces, viewed from below (through the substrate). Substrate curvature, r_s is indicated in each row, along with We. Times τ are dimensionless with respect to the kinetic time scale, $2r_c/u$. Note that droplets appear ellipsoidal in these images due to a slight misalignment between the mirror and curved target (concave lens). The scale bar is 2 mm.

standard deviations away, but diverges after a minimum at $\Omega < 0.3$. C&H (2017) noted that their observations disagreed with a 1999 paper that considered impact onto dry spheres (but still with continuous impingement at 1000 Hz), which concluded that it was easier to splash on small spheres [25]. A qualitatively-similar trend was obtained by Liang et al. (2014) for impact onto wetted spheres (with a pre-existing film of varying thickness: 12 μm–61 μm). The splashing threshold of millimetric heptane droplets ($Oh = 2.6 \times 10^{-3}$, diameter 1.8 mm) on spheres was found to approximately coincide with that of a flat substrate for

$\Omega < 0.224 : \mathrm{We} = 124$, corresponding to $\mathrm{K} = 90$ [28]. Indeed, the presence of a thin film is known to reduce the splashing threshold of heptane droplets on smooth flat substrates [38]. In Liang et al.'s work, for smaller spheres ($\Omega > 0.224$), the splashing threshold increased approximately linearly with Ω, similar to our data. Their observed $\Omega < 0.224$ behaviour may owe to the pre-existing thin film, which could decrease the effective substrate curvature and alter the lift force acting on the lamella (see Section 3.2). With the benefit of a wider range of $\Omega \in [-0.08, 0.55]$, a thoroughly-dry substrate, and verifiable-axisymmetry, our work demonstrates that the splashing threshold on dry curved substrates consistently increases with increasing Ω over concave, flat, and convex substrates.

For a single liquid and a unique flat substrate, K is sufficient to parameterise splashing thresholds, though they are also affected by the surrounding gas pressure [39] (amongst other factors), which K does not account for. In recent times, for smooth flat hydrophobic substrates, low-Oh splashing has been successfully parameterised by a splashing ratio

$$\beta(\alpha) = \frac{2.22}{\tan\alpha}\frac{\mu_g^{1/2}(\rho r_c u^5)^{1/6}}{\sigma^{2/3}}, \tag{1}$$

which was derived assuming that splashing results from the growth of capillary instabilities as aerodynamic forces (the sum of gas lubrication and suction forces) lift the advancing lamella off the substrate [5,40,29,41]. Here, $\mu_g = 1.8 \times 10^{-5}$ Pa s is the gas' dynamic viscosity, r_c is the chosen length scale, and α is the *wedge angle* between the substrate and lamella at the onset of splashing. $\alpha \approx 60^\circ$ for smooth flat substrates, independent of wettability [41]. Splashing on smooth flat substrates, from wetting to superhydrophobic, has been successfully parameterised using $\beta(\alpha)$ and the dynamic contact angle [10]. The theory underpinning $\beta(\alpha)$ has also been extended to rough substrates [42], and to explain splashing suppression of micron-sized droplets [43].

Accordingly, our experimental data is plotted in terms of $\beta(\alpha)$ in Fig. 3b. The flat threshold ($r_s \to \infty$) of $\beta(\alpha) \approx 0.12$ is consistent with existing data for hydrophilic flat substrates: Ref. [41] reports a splashing threshold of 0.120 ± 0.008 for ethanol–water mixtures, taking the radius as the length scale. For spheres, increasing either r_c or r_s promotes splashing, whilst they have opposite effects on Ω. Hence, we plot against the dimensionless quantity $\mu^4/(\rho^2\sigma^2 r_c r_s)$ instead in Fig. 3b, which is Oh^4 with $l = \sqrt{r_c r_s}$, the geometric mean of the radii of curvature, so $\mathrm{Oh}^4 \propto 1/(r_c r_s)$. Our larger droplet volume ($(4.85 \pm 0.15)\mu$L) data, for $r_s = 3.0$ mm, are also plotted in Fig. 3b, whose threshold is seen to be consistent with the existing $(3.6 \pm 0.3)\mu$L data, which would not be the case if plotting against Ω.

3.2. Splashing mechanism

We now wish to explain the trend in splashing propensity seen in Fig. 3 from a physical perspective. Our hypothesis is that the propensity to splash decreases as $1/r_s$ increases due to a modification to the lift force on the lamella, which can be accounted for geometrically. For a general geometry, we define an effective wedge angle α^*, where $\alpha^* = \psi + \phi$. In Fig. 5a, ψ is the angle between the tangent to the lamella at the contact point and the horizontal, whilst ϕ is the angle between the horizontal and downstream tangent to the substrate at the contact point (if $r_s < 0$, then $\phi < 0$), both at the onset of breakup. Herein, all angles are reported in radians.

Whilst $\phi = 0$ for a flat substrate (with $\alpha = \psi = \pi/3$), ϕ is non-zero for curved substrates. Geometrically, ϕ is also the angle subtended by the substrate between the vertical axis and contact point, at the centre of the substrate's curvature (see Fig. 5a). Therefore, $s = r_s\phi$, where s is half of the spread length of the droplet along the curved substrate at the onset of breakup. Note that $\phi \to 0$ as $r_s \to \infty$, as required for a flat substrate. Fig. 5b presents s measured for a selection of our experiments, plotted against $1/r_s$; error bars represent the variation between different experiments. The data shows that s, within experimental error, does not depend on the substrate curvature. A similar conclusion was reached in C&H (2017) with micrometric droplets; their data, extracted from figure 16, is also plotted in Fig. 5b (green points, plotted against Ω). Hence, $s = 1.9$ mm, delineated by the dashed line in Fig. 5b, is taken as a fixed constant value, within experimental error for all curvatures in Fig. 5b. Consequently, ϕ can be regraded as a geometric property of the substrate.

The angle between the tangent to the lamella at the contact point and the horizontal at the onset of breakup, ψ would be expected to decrease as $1/r_s$ increases, since the surrounding gas is easier to drain from beneath the lamella on smaller spheres. This variable was measured for a selection of our splashing experiments, noting that $\psi = \pi - \theta - \phi$ (see Figs. 1d and 5a), and plotted in Fig. 5c against $1/r_s$, alongside equivalent data from C&H (2017), extracted from figure 17 (green points, plotted against Ω); the error bars represent variation between different experiments. We note here the appreciable challenges of both accurately determining the exact time of breakup and measuring the true dynamic contact angle for splashing studies in general [41,10,44]; hence, the relatively large experimental uncertainty in ψ. Moreover, for convex substrates, if any part of the lamella falls below the horizontal plane containing the contact point (always if $\psi \lesssim 0$; often the case for small $\psi > 0$), then the true contact point (and therefore θ) is hidden by the revolved lamella. See the darker lamella region of the sketch inset in Fig. 5a, where the hidden contact point is indicated. In such cases, θ and ψ cannot be measured from an external side view (as in this work). Despite these challenges, Fig. 5c indicates that ψ varies linearly with respect to $1/r_s$. Note that ψ, an offset contact angle, should not depend on r_c, given that contact angles are determined by the chemical properties of the substrate and wetting fluid [45,46]. Recalling that $\psi = \pi/3$ at $1/r_s = 0$ (flat substrate), the linear dependence on r_s implies that $\psi = \pi/3 + m/r_s$ for a gradient m.

The effective wedge angle on curved substrates, α^* is therefore given by

$$\alpha^* = \psi + \phi = \frac{\pi}{3} + \frac{m+s}{r_s}. \tag{2}$$

Recall from Section 3.1 that $\beta(\alpha) \approx 0.12$ (flat substrates). Moreover, $s = 1.9$ mm is constant, which suggests that $m = -1.75$ mm to parameterise the effect of substrate curvature. This value of m indicated by the slope of the triangle in Fig. 5c, which is consistent (within identified errors) with both data sets shown. Hence, the data in Fig. 3b are replotted with the splashing ratio corrected for substrate curvature by substituting Eqn. (2) into Eqn. (1) with $m + s = 0.15$ mm, denoted $\beta(\alpha^*)$, in Fig. 6. As seen, $\beta(\alpha^*) \approx 0.12$ for all concave, convex, and flat substrates studied. That is, $\beta(\alpha^*)$ yields a consistent splashing threshold for axisymmetric impact, regardless of substrate curvature.

Substrate curvature can therefore be taken into account in Eqn. (1) using the effective wedge angle α^*. Note that the origin of the constant wedge angle for flat substrates is the relative position of the contact point and the tip of the lamella, due to the no-slip condition [40]. On spheres, the contact point moves downwards by a constant amount for a given curvature (given that s is fixed), effectively opening the gap between the lamella and substrate, notwithstanding the relative ease of draining gas from beneath the lamella. The relative change in the vertical position of the contact point depends on the size of the sphere, showing that α^* depends on r_s. In other words, $\alpha^* > \pi/3$ characterises the effective increase in

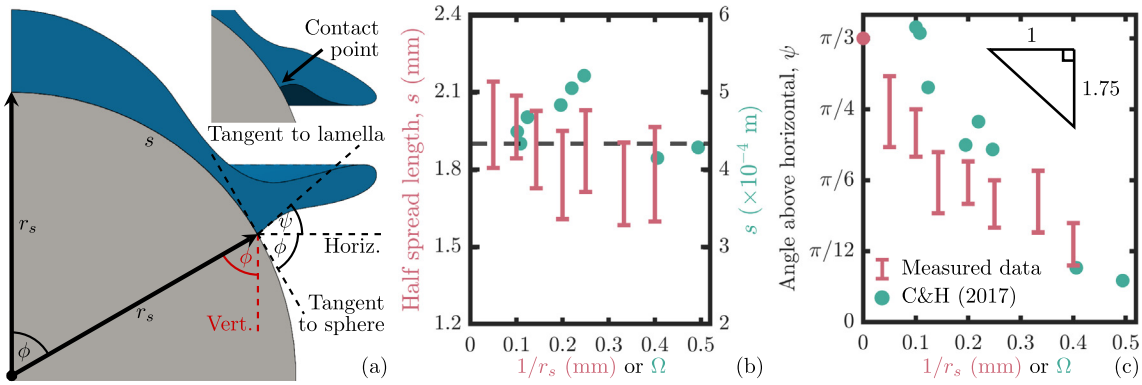

Fig. 5. (a) Sketch of a droplet spreading on a sphere, at the point of lamella breakup, with variables pertinent to the proposed mechanism indicated. Not to scale. Note that $\alpha^* = \phi + \psi$. The inset sketch shows that the contact point in a 2D vertical plane (indicated) can be hidden by the 3D revolved lamella (darker blue) from an external view. (b) Half spread length on the curved substrate at the onset of breakup, s, against a measure of substrate curvature. The dashed line indicates the constant value of $s = 1.9$ mm. (c) ψ (at the onset of breakup) against the same measure of substrate curvature. For both graphs, axis labels are colour-coded according to relevant data; red data was measured from our convex substrate experiments that splash; green data was extracted from C&H (2017) [26]. Error bars represent variation between differ.ent experiments.

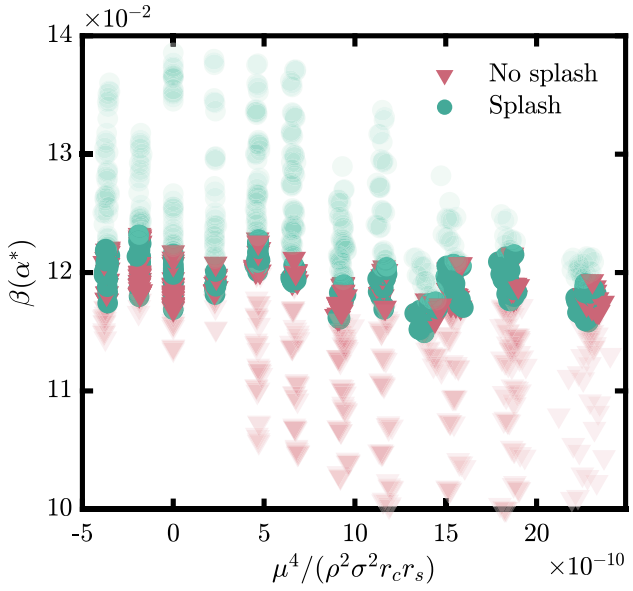

Fig. 6. Splashing propensity of (3.6 ± 0.3)μL and (4.85 ± 0.15)μL droplets parameterised by the splashing ratio corrected for substrate curvature using the wedge angle given in (2), denoted $\beta(\alpha^*)$, with $s = 1.9$ mm and $m = -1.75$ mm.

the lift force ($\propto 1/\tan\alpha$) that is required to have a droplet splash on a sphere at the same threshold as on a flat substrate (i.e. 0.12). Whilst the derivation (and values of m and s) was based upon spheres, Eqn. (1) predicts that $\alpha^* < \pi/3$ for convex surfaces ($r_s < 0$): $\beta(\alpha^*)$ increases in this case to account for the reduced splashing threshold identified in Section 3.1. The correction proposed therefore accounts for the effects of both positive and negative substrate curvature, as confirmed in Fig. 6.

In Eqn. (1), only the wedge angle has been modified in order to accommodate substrate curvature, whilst $\beta(\alpha)$ (with a fixed wedge angle) can successfully parameterise splashing thresholds of a wide range of low-viscosity fluids on flat substrates [10,41,40]. We thus expect that the wedge angle should not be affected by fluid properties on curved substrates either. Hence, the (geometrically-derived) effective wedge angle approach may be used to parameterise splashing thresholds on curved substrates for a wider range of low-viscosity fluids than studied here. Moreover, there is no strong dependence of substrate curvature on spreading rates on time scales relevant to splashing (see §3 of the Supplementary Material). This observation indicates that $\beta(\alpha^*)$ and θ may parameterise splashing on curved substrates of different wettabilities, as $\beta(\alpha)$ and θ can for flat substrates [10].

3.3. Asymmetric impacts

The results above pertain to axisymmetric impact ($c \approx 0$); in this section, we assess the effect of initial asymmetry between the impacting droplet and curved substrate via a horizontal offset from the axis of symmetry. Fig. 7a depicts the impact position on all $r_s \geqslant 2.0$ mm substrates investigated, from the perspective of a top-down view, with radial positions normalised by r_c. Only those experiments within the $\beta(\alpha)$ splashing threshold region for each substrate ($\beta(\alpha) \in [\beta_l, \beta_h]$ – see Section 3.1 for equivalent definitions in K) are displayed; these data correspond to all $r_s > 0$ points in Fig. 3b, in addition to $c/r_c > 0.15$ experiments (delineated by the orange-dashed circle in Fig. 7a). A pessimistic indication of the maximum error in determining the impact position (based on the cameras' minimum effective resolution) is indicated by the purple circle surrounding one point. Since only experiments within the splashing threshold regions (commensurate to the experimental error) are plotted, if asymmetry did not play a role in splashing outcomes here, then a uniform distribution would be expected in Fig. 7a. Such a distribution is seen for almost-axisymmetric impacts, but the splashing outcome is seen to dominate for experiments with $c/r_c \gtrsim 0.12$. Note that no such radial dependence would be expected if *all* experiments (i.e. both inside and outside the splashing threshold regions) were plotted. In summary, Fig. 7a suggests that modest offsets increase the splashing propensity of droplets close to the splashing threshold. To ensure that all axisymmetric impacts are included in the regime maps (Figs. 3 and 6), only $c/r_c < 0.15$ experiments are displayed.

Examples of typical non-axisymmetric impacts above the threshold region are shown in Figs. 7b and 7c. The whole offset is seen in the upper rows (from the perspective of one camera), whilst the offset is negligible ($< 0.01 r_c$) in the perpendicular direction (bottom rows, from the perspective of the other camera). Interestingly, non-axisymmetric splashing dynamics are seen in the negligible offset rows. We suggest that this observation results from inherently-3D effects influencing rim breakup due to a perturbation from the offset, which is best perceived from a bottom-up view of non-axisymmetric impact onto one of the concave surfaces, as shown in Fig. 7d ($c/r_c \approx 0.3$). Here, the gas beneath the lamella is harder to drain in the direction of the offset (with respect to the substrate apex, identified by a red circle), due to the upward-

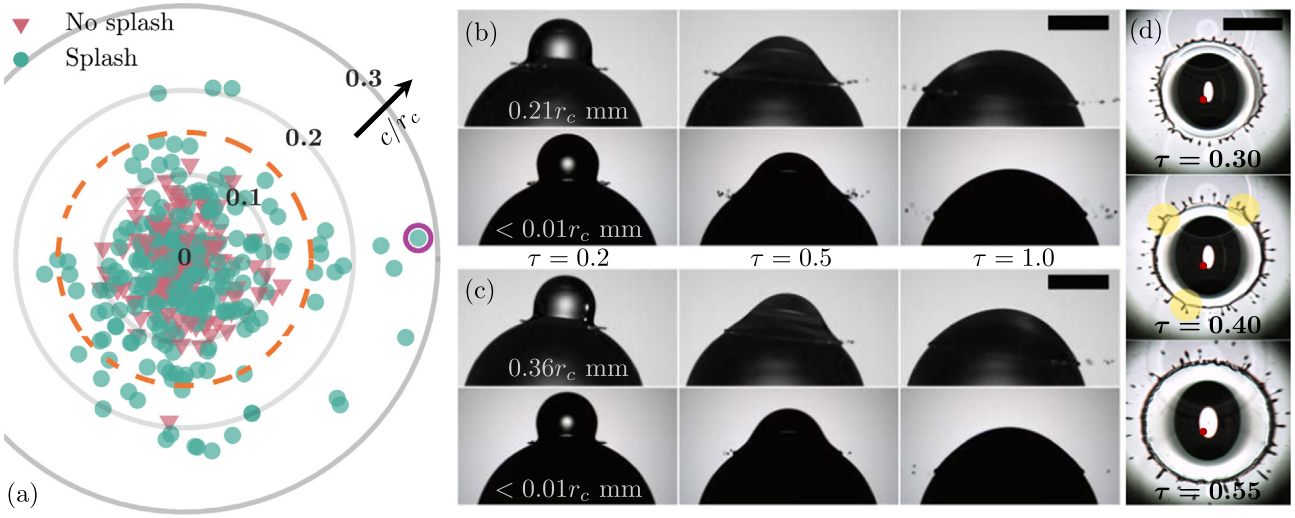

Fig. 7. Effect of asymmetry. (a) Impact position (centre axisymmetric) of every $r_s > 0$ experiment within the $\beta(\alpha)$ splashing threshold regions (all opaque $r_s > 0$ points in Fig. 3b; additional experiments with a larger offset), coloured by splashing outcome. The purple circle indicates the maximum error in impact position, based upon the minimum effective resolution of 34 pixels mm^{-1}. Only experiments within the orange dashed circle (indicating $c/r_c = 0.15$) are shown in the regime maps above. (b) We $= 482$; $\beta(\alpha) = 0.144$ impact onto a $r_s = 3.0$ mm sphere. Dimensional offsets in the *perpendicular* planes of view are indicated in each $\tau = 0.2$ frames. (c) Similar We $= 436$; $\beta(\alpha) = 0.141$ impact to panel (b), but with a larger offset. (d) Asymmetric We $= 345/\beta(\alpha) = 0.128$ impact (offset $c/r_c \approx 0.3$) onto a $r_s = -12.92$ mm substrate. Red points locate the substrate apex (approximately); yellow highlights indicate inherently 3D rim phenomena. All scale bars are 2 mm.

sloping substrate, so the lamella remains raised for longer in such directions. These asymmetric rim dynamics lead to the large distribution in satellite sizes and trajectories for a given impact, including due to the aforementioned 3D effects such as a splitting and merging of fingers (highlighted yellow in Fig. 7d). Also seen with non-zero offsets is film breakup in the body of the lamella, which can lead to long ligaments with substantial angular velocity that result in non-radial satellite trajectories. Note that many satellites land within the maximum spread length of the droplet in the direction of offset on concave surfaces, as the substrate curves substantially upwards to meet the satellites' trajectories. These 3D effects may play a role in the increase in splashing propensity seen with modest offsets for experiments close to the splashing threshold (identified in the previous paragraph), including the relatively-sharp radial transition seen in Fig. 7a.

In the offset views (top rows) of Figs. 7b and 7c, splashing is generally more pronounced in the 'downward' direction (towards the right here). Splashing can be suppressed in the 'upward' direction for larger offsets, as exhibited in Fig. 7c. These observations are consistent with known splashing behaviour on inclined flat substrates, where upward splashing is suppressed above a given substrate inclination, followed by the suppression of downward splashing at a yet greater inclination [47,48]. Under the theoretical framework from which $\beta(\alpha)$ is derived, the modification of splashing on inclined flat substrates stems from an effective reduction in impact velocity perpendicular to the substrate according to $\cos\eta$, where η is the substrate inclination. The lamella tip velocities therefore decrease with increasing η too, as does the lift force acting on the lamella itself, which in turn affects splashing. For a spherical substrate, η is the polar angle to the impact point from the vertical (similar to ϕ in Fig. 1e). Fig. 7c indicates that the mechanism of splashing modification on inclined flat substrates translates to curved substrates, so complete splashing suppression on spheres might be expected for even larger offsets than shown in Fig. 7c, though this is beyond the scope of our work.

Finally, it is interesting to note the relation of offsets from axisymmetry to the mechanism discussed in Section 3.2. Offsets decrease the effective substrate curvature in the upward direction, reducing the ability to drain gas from beneath the lamella, as elucidated in Section 3.2; conversely, the gas is easier to drain in the downward direction. Moreover, the substrate drops away from the lamella at a faster rate than in the downward direction compared to the upward direction, opening the effective wedge angle and reducing the splashing ratio. However, suppressed splashing is seen in the upward direction in Fig. 7c, which suggests that for large offsets the mechanism noted above for splashing suppression on tilted flat substrates may carry-over to curved substrates and the reduction in lamella tip velocities may be more significant than curvature-related effects.

4. Conclusions

This study has conclusively demonstrated that droplet splashing is significantly affected by the target substrate's curvature. Notably, we found that the radius of curvature, r_s plays a key role in the micromechanics of splashing. For axisymmetric impacts, splashing propensity was found to decrease monotonically with increasing $1/r_s$ over the uniquely-wide range of target geometries studied, including both convex ($r_s > 0$) and concave ($r_s < 0$) substrates, with a boundary value consistent with the known splashing behaviour on flat substrates ($r_s \to \infty$). Therefore, the splashing threshold is higher for smaller spheres compared to a flat substrate, whilst it is lower for concave surfaces. This new result for completely-dry surfaces diverges from related studies that considered wetted or continuously impinged spheres [25,26,28], in which splashing thresholds only appeared to change for the smaller spheres studied. We hypothesised that the alteration to the splashing thresholds seen in this work owes to a curvature-induced modification to the lift force acting on the advancing lamella at the point of breakup. Hence, we successfully incorporated the effect of substrate curvature into state-of-the-art splashing theory for flat substrates [5,29,40,41] via the introduction of an effective wedge angle between the lamella and substrate. Effects of asymmetry are only apparent for lateral offsets from axisymmetry greater than approximately 0.12, normalised by the droplet's radius of curvature at the point of impact. Inherently-3D dynamics are prevalent for asymmetric impact with a small offset, whilst splashing can be suppressed, at least in some directions, for larger

offsets. The latter result has parallels with splashing on inclined flat substrates [47,48]. Our results enhance the fundamental understanding of splashing in general, which is relevant to surfaces of other properties and geometries than the curved substrates we studied, but also indicate the potential for engineering textured substrates to reduce the distribution and aerosolisation of potentially-hazardous fluids by modifying droplet splashing dynamics.

Declaration of Competing Interest

The authors declare that they have no known competing financial interests or personal relationships that could have appeared to influence the work reported in this paper.

Funding acknowledgement

This work was funded by a Royal Society University Research Fellowship (Grant No. URF\R\180016) & Enhancement Award (Grant No. RGF\EA\181002) and two NSF/CBET-EPSRC grants (Grant Nos. EP/S029966/1 and EP/W016036/1).

Appendix A. Supplementary material

Supplementary data associated with this article can be found, in the online version, at https://doi.org/10.1016/j.jcis.2022.01.136.

References

[1] A.M. Worthington, R.S. Cole, IV. Impact with a liquid surface studied by the aid of instantaneous photography. Paper II, Philos. Trans. R. Soc. London, Ser. A 194 (252–261) (1900) 175–199. doi:10.1098/rsta.1900.0016.
[2] A.L. Yarin, Drop impact dynamics: splashing, spreading, receding, bouncing, Annu. Rev. Fluid Mech. 38 (2006) 159–192, https://doi.org/10.1146/annurev.fluid.38.050304.092144.
[3] C. Josserand, S.T. Thoroddsen, Drop impact on a solid surface, Annu. Rev. Fluid Mech. 48 (2016) 365–391, https://doi.org/10.1146/annurev-fluid-122414-034401.
[4] M.M. Driscoll, S.R. Nagel, Ultrafast interference imaging of air in splashing dynamics, Phys. Rev. Lett. 107 (15) (2011) 154502, https://doi.org/10.1103/PhysRevLett.107.154502.
[5] G. Riboux, J.M. Gordillo, Experiments of drops impacting a smooth solid surface: A model of the critical impact speed for drop splashing, Phys. Rev. Lett. 113 (2) (2014) 024507, https://doi.org/10.1103/PhysRevLett.113.024507.
[6] Y. Liu, P. Tan, L. Xu, Kelvin-Helmholtz instability in an ultrathin air film causes drop splashing on smooth surfaces, PNAS 112 (11) (2015) 3280–3284, https://doi.org/10.1073/pnas.1417718112.
[7] J. Palacios, J. Hernández, P. Gómez, C. Zanzi, J. López, Experimental study of splashing patterns and the splashing/deposition threshold in drop impacts onto dry smooth solid surfaces, Exp. Therm Fluid Sci. 44 (2013) 571–582, https://doi.org/10.1016/j.expthermflusci.2012.08.020.
[8] H. Almohammadi, A. Amirfazli, Droplet impact: Viscosity and wettability effects on splashing, J. Colloid Interface Sci. 553 (2019) 22–30, https://doi.org/10.1016/j.jcis.2019.05.101.
[9] H. Almohammadi, A. Amirfazli, Understanding the drop impact on moving hydrophilic and hydrophobic surfaces, Soft Matter 13 (10) (2017) 2040–2053, https://doi.org/10.1039/C6SM02514E.
[10] M.A. Quetzeri-Santiago, K. Yokoi, A.A. Castrejón-Pita, J.R. Castrejón-Pita, Role of the dynamic contact angle on splashing, Phys. Rev. Lett. 122 (22) (2019) 228001, https://doi.org/10.1103/PhysRevLett.122.228001.
[11] M.A.J. Van Limbeek, P.B.J. Hoefnagels, M. Shirota, C. Sun, D. Lohse, Boiling regimes of impacting drops on a heated substrate under reduced pressure, Phys. Rev. Fluids 3 (5) (2018) 053601, https://doi.org/10.1103/PhysRevFluids.3.053601.
[12] L. Bourouiba, The fluid dynamics of disease transmission, Annu. Rev. Fluid Mech. 53 (2021) 473–508, https://doi.org/10.1146/annurev-fluid-060220-113712.
[13] D. Khojasteh, N.M. Kazerooni, M. Marengo, A review of liquid droplet impacting onto solid spherical particles: A physical pathway to encapsulation mechanisms, J. Ind. Eng. Chem. 71 (2019) 50–64, https://doi.org/10.1016/j.jiec.2018.11.030.
[14] Y. Zhang, C. Tse, D. Rouholamin, P.J. Smith, Scaffolds for tissue engineering produced by inkjet printing, Cent. Eur. J. Eng. 2 (3) (2012) 325–335, https://doi.org/10.2478/s13531-012-0016-2.
[15] S.A. Banitabaei, A. Amirfazli, Droplet impact onto a solid sphere: Effect of wettability and impact velocity, Phys. Fluids 29 (6) (2017) 062111, https://doi.org/10.1063/1.4990088.
[16] G. Khurana, N. Sahoo, P. Dhar, Phenomenology of droplet collision hydrodynamics on wetting and non-wetting spheres, Phys. Fluids 31 (7) (2019) 072003, https://doi.org/10.1063/1.5103223.
[17] I. Yoon, S. Shin, Direct numerical simulation of droplet collision with stationary spherical particle: A comprehensive map of outcomes, Int. J. Multiphase Flow 135 (2021) 103503, https://doi.org/10.1016/j.ijmultiphaseflow.2020.103503.
[18] M.A. Quetzeri-Santiago, A.A. Castrejón-Pita, J.R. Castrejón-Pita, The effect of surface roughness on the contact line and splashing dynamics of impacting droplets, Sci. Rep. 9 (1) (2019) 1–10, https://doi.org/10.1038/s41598-019-51490-5.
[19] S. Bakshi, I.V. Roisman, C. Tropea, Investigations on the impact of a drop onto a small spherical target, Phys. Fluids 19 (3) (2007) 032102, https://doi.org/10.1063/1.2716065.
[20] A. Bordbar, A. Taassob, D. Khojasteh, M. Marengo, R. Kamali, Maximum spreading and rebound of a droplet impacting onto a spherical surface at low Weber numbers, Langmuir 34 (17) (2018) 5149–5158, https://doi.org/10.1021/acs.langmuir.8b00625.
[21] D. Khojasteh, A. Bordbar, R. Kamali, M. Marengo, Curvature effect on droplet impacting onto hydrophobic and superhydrophobic spheres, Int. J. Comput. Fluid Dyn. 31 (6–8) (2017) 310–323, https://doi.org/10.1080/10618562.2017.1349312.
[22] X. Liu, X. Zhang, J. Min, Maximum spreading of droplets impacting spherical surfaces, Phys. Fluids 31 (9) (2019) 092102, https://doi.org/10.1063/1.5117278.
[23] S. Chen, V. Bertola, Drop impact on spherical soft surfaces, Phys. Fluids 29 (8) (2017) 082106, https://doi.org/10.1063/1.4996587.
[24] S. Mitra, T.B.T. Nguyen, E. Doroodchi, V. Pareek, J.B. Joshi, G.M. Evans, On wetting characteristics of droplet on a spherical particle in film boiling regime, Chem. Eng. Sci. 149 (2016) 181–203, https://doi.org/10.1016/j.ces.2016.04.003.
[25] Y. Hardalupas, A. Taylor, J. Wilkins, Experimental investigation of sub-millimetre droplet impingement on to spherical surfaces, Int. J. Heat Fluid Flow 20 (5) (1999) 477–485, https://doi.org/10.1016/S0142-727X(99)00045-4.
[26] G. Charalampous, Y. Hardalupas, Collisions of droplets on spherical particles, Phys. Fluids 29 (10) (2017) 103305, https://doi.org/10.1063/1.5005124.
[27] G. Liang, Y. Guo, Y. Yang, S. Guo, S. Shen, Special phenomena from a single liquid drop impact on wetted cylindrical surfaces, Exp. Therm Fluid Sci. 51 (2013) 18–27, https://doi.org/10.1016/j.expthermflusci.2013.06.012.
[28] G. Liang, Y. Guo, X. Mu, S. Shen, Experimental investigation of a drop impacting on wetted spheres, Exp. Therm. Fluid Sci. 55 (2014) 150–157, https://doi.org/10.1016/j.expthermflusci.2013.06.012.
[29] J.M. Gordillo, G. Riboux, A note on the aerodynamic splashing of droplets, J. Fluid Mech. 871 (2019) R3, https://doi.org/10.1017/jfm.2019.396.
[30] T.C. Sykes, Internal dynamics of coalescing droplets Ph.D. thesis, University of Leeds, 2020.
[31] M.A. Quetzeri-Santiago, J.R. Castrejón-Pita, A.A. Castrejón-Pita, On the analysis of the contact angle for impacting droplets using a polynomial fitting approach, Exp. Fluids 61 (2020) 1–13, https://doi.org/10.1007/s00348-020-02971-1.
[32] E. Li, M.-J. Thoraval, J. Marston, S.T. Thoroddsen, Early azimuthal instability during drop impact, J. Fluid Mech. 848 (2018) 821–835, https://doi.org/10.1017/jfm.2018.383.
[33] Q. Liu, J.H.Y. Lo, Y. Li, Y. Liu, J. Zhao, L. Xu, The role of drop shape in impact and splash, Nat. Commun. 12 (1) (2021) 1–8, https://doi.org/10.1038/s41467-021-23138-4.
[34] C. Lin, K. Zhang, X. Chen, L. Xiao, S. Chen, J. Zhu, T. Zou, Reducing droplet contact time and area by craterlike surface structure, Phys. Rev. Fluids 6 (8) (2021) 083602, https://doi.org/10.1103/PhysRevFluids.6.083602.
[35] Y. Wang, L. Bourouiba, Unsteady sheet fragmentation: droplet sizes and speeds, J. Fluid Mech. 848 (2018) 946–967, https://doi.org/10.1017/jfm.2018.359.
[36] H. Zhang, Y. Gao, X. Zhang, X. Yi, Y. Du, F. He, Z. Jin, P. Hao, Characteristics of secondary droplets produced by the impact of drops onto a smooth surface, Adv. Aerodyn. 3 (1) (2021) 1–12, https://doi.org/10.1186/s42774-021-00091-w.
[37] J.C. Bird, S.S.H. Tsai, H.A. Stone, Inclined to splash: triggering and inhibiting a splash with tangential velocity, New J. Phys. 11 (6) (2009) 063017, https://doi.org/10.1088/1367-2630/11/6/063017.
[38] R.L. Vander Wal, G.M. Berger, S.D. Mozes, The combined influence of a rough surface and thin fluid film upon the splashing threshold and splash dynamics of a droplet impacting onto them, Exp. Fluids 40 (1) (2006) 23–32. doi:10.1007/s00348-005-0043-3.
[39] L. Xu, W.W. Zhang, S.R. Nagel, Drop splashing on a dry smooth surface, Phys. Rev. Lett. 94 (18) (2005) 184505, https://doi.org/10.1103/PhysRevLett.94.184505.
[40] G. Riboux, J.M. Gordillo, Boundary-layer effects in droplet splashing, Phys. Rev. E 96 (1) (2017) 013105, https://doi.org/10.1103/PhysRevE.96.013105.

[41] T.C. de Goede, N. Laan, K.G. De Bruin, D. Bonn, Effect of wetting on drop splashing of newtonian fluids and blood, Langmuir 34 (18) (2018) 5163–5168, https://doi.org/10.1021/acs.langmuir.7b03355.
[42] P. García-Geijo, E.S. Quintero, G. Riboux, J.M. Gordillo, Spreading and splashing of drops impacting rough substrates, J. Fluid Mech. 917 (2021) A50, https://doi.org/10.1017/jfm.2021.313.
[43] M. Usawa, Y. Fujita, Y. Tagawa, G. Riboux, J.M. Gordillo, Large impact velocities suppress the splashing of micron-sized droplets, Phys. Rev. Fluids 6 (2) (2021) 023605, https://doi.org/10.1103/PhysRevFluids.6.023605.
[44] C.A. Papakonstantinou, H. Chen, A. Amirfazli, New ellipse fitting method for contact angle measurement, Surf. Innovations (2021) 1–9, https://doi.org/10.1680/jsuin.21.00028.
[45] J.F. Joanny, P.-G. De Gennes, A model for contact angle hysteresis, J. Chem. Phys. 81 (1) (1984) 552–562, https://doi.org/10.1063/1.447337.
[46] D. Bonn, J. Eggers, J. Indekeu, J. Meunier, E. Rolley, Wetting and spreading, Rev. Mod. Phys. 81 (2) (2009) 739, https://doi.org/10.1103/RevModPhys.81.739.
[47] Š. Šikalo, C. Tropea, E. Ganić, Impact of droplets onto inclined surfaces, J. Colloid Interface Sci. 286 (2) (2005) 661–669, https://doi.org/10.1016/j.jcis.2005.01.050.
[48] J. Hao, J. Lu, L. Lee, Z. Wu, G. Hu, J.M. Floryan, Droplet splashing on an inclined surface, Phys. Rev. Lett. 122 (5) (2019) 054501, https://doi.org/10.1103/PhysRevLett.122.054501.

Supplementary Material for: Droplet splashing on curved substrates

Thomas C. Sykes,[1,*] Ben D. Fudge,[1] Miguel A. Quetzeri-Santiago,[2]
J. Rafael Castrejón-Pita,[3,†] and Alfonso A. Castrejón-Pita[1,‡]

[1] *Department of Engineering Science, University of Oxford, Oxford OX1 3PJ, United Kingdom*
[2] *Mesoscale Chemical Systems Group, MESA+ Institute and Faculty of Science and Technology, University of Twente, 7500AE Enschede, The Netherlands*
[3] *School of Engineering and Materials Science, Queen Mary University of London, London E1 4NS, United Kingdom*

(Dated: January 11, 2022)

CONTENTS

§1. ACCOUNTING FOR NON-SPHERICITY OF IMPACTING DROPLETS

A. Measuring the radius of curvature, r_c

As mentioned in the main text, oscillations in the free surface of the falling droplets meant that they were not necessarily spherical on impact. In such cases, several studies in the literature [e.g. 1] have recognised that it is more appropriate to base the characteristic length upon the radius of curvature at the bottom of the droplet (its 'south point'), r_c, rather than use the droplet's equivalent spherical radius, r_n. If the droplet can be well approximated by an axially-aligned ellipse, then r_c is well-defined by the droplet's aspect ratio and r_n. However, the droplets in this study could not always be well approximated by such an ellipse, so it was preferred to measure r_c directly using image processing: a circle was fitted to detected edges within a certain angular range around the droplet's south point.

For a typical experiment, Fig. S1a demonstrates the result of fitting a (blue) circle to all (yellow) detected edges of the droplet, which suggests that $r_n = 0.96\,\text{mm}$ in this example. Evidently, the droplet is oblate (with eccentricity ~ 0.29); the fitted circle does not coincide with the detected edges around the south or east points, but this fitting is likely to yield a fair approximation to r_n. In Fig. S1b, a (red) circle is fitted only to the (green) detected edges spanning the lower 60° of detected edges (called the 'fitting angular range around the south point'), yielding $r_c = 1.06\,\text{mm}$. In this case, the fitted circle coincides exceptionally well with the detected edges around the south point, giving high confidence that r_c approximates the radius of curvature of the bottom of the droplet well.

The choice of 60° for the fitting angular range is elucidated in Fig. S1c, where r_c is measured based upon angles of 20°–120° for six randomly-chosen experiments, represented by different colours. For each experiment, r_n is indicated by the dashed line of equivalent colour. For small angular ranges $\lesssim 40°$, the measurement of r_c is unreliable due to the small range in vertical position of all detected edge pixels involved, relative to the error in their detected position,

* thomas.sykes@eng.ox.ac.uk; t.c.sykes@outlook.com
† castrejon@cantab.net
‡ alfonso.castrejon-pita@wadham.ox.ac.uk

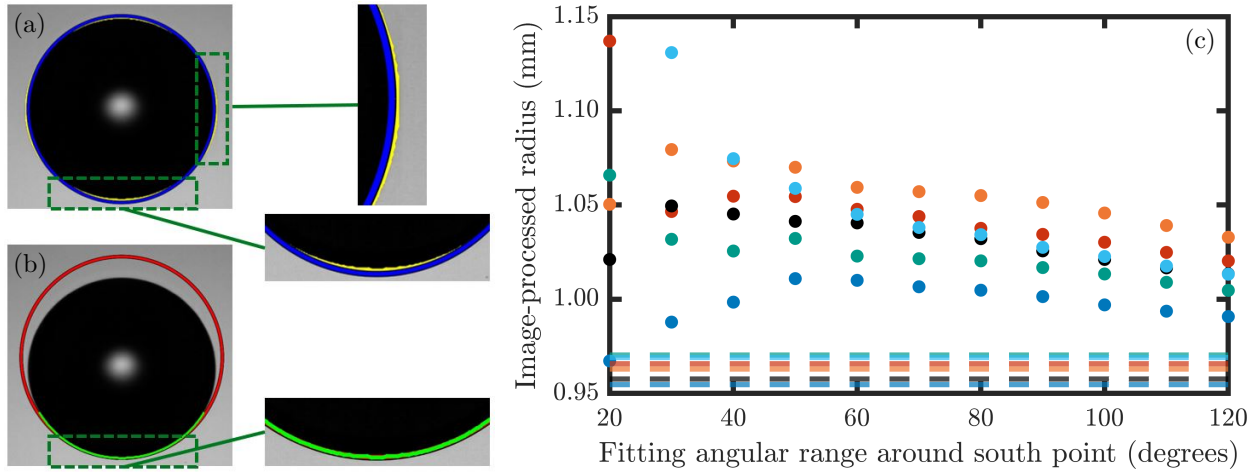

FIG. S1: (a) A (blue) circle fitted to the (yellow) detected edges of the whole droplet, yielding $r_n = 0.96\,\text{mm}$. (b) A (red) circle fitted to the (green) detected edges of the same droplet, covering an angular range of 60° spanning the droplet's south point, yielding $r_c = 1.06\,\text{mm}$. (c) The dependence of r_c on fitting angular range for six randomly-chosen experiments, represented by different colours; the horizontal dashed lines indicate r_n for each.

despite the use of an accurate subpixel edge detection method (see Ref. [2]). On the other hand, the oblate nature of a typical droplet in this work means that the use of a too high angular range would be expected to artificially lower the detected r_c (and similarly, if the droplet were a prolate spheroid, increase the measured r_c), which is borne out in Fig. S1c. 60° is therefore chosen as a good compromise between these two competing demands – it's the lowest value with which we have confidence of consistently attaining reliable measurements. In general, the choice of angular range is likely to depend upon the effective resolution of the image, magnitude of eccentricity, and quality of edge detection.

B. Effects of non-sphericity

The axisymmetric impact of three $r_n = 0.96\,\text{mm}$ droplets onto a $r_s = 2.5\,\text{mm}$ sphere at $u = 2.40\,\text{m}\,\text{s}^{-1}$ are shown in Fig. S2. $r_c \in [1.02, 1.06]$ mm is varied between rows, giving $\text{We} = \rho u^2 \cdot 2r_c/\sigma \in [412, 430]$. The smallest $r_c = 1.02\,\text{mm}$ droplet exhibits simple deposition (no breakup), whilst the two more oblate droplets ($r_c \in \{1.04, 1.06\}$ mm) splash. If the characteristic length scale were based upon r_n, then there would be no difference in Weber number (or indeed

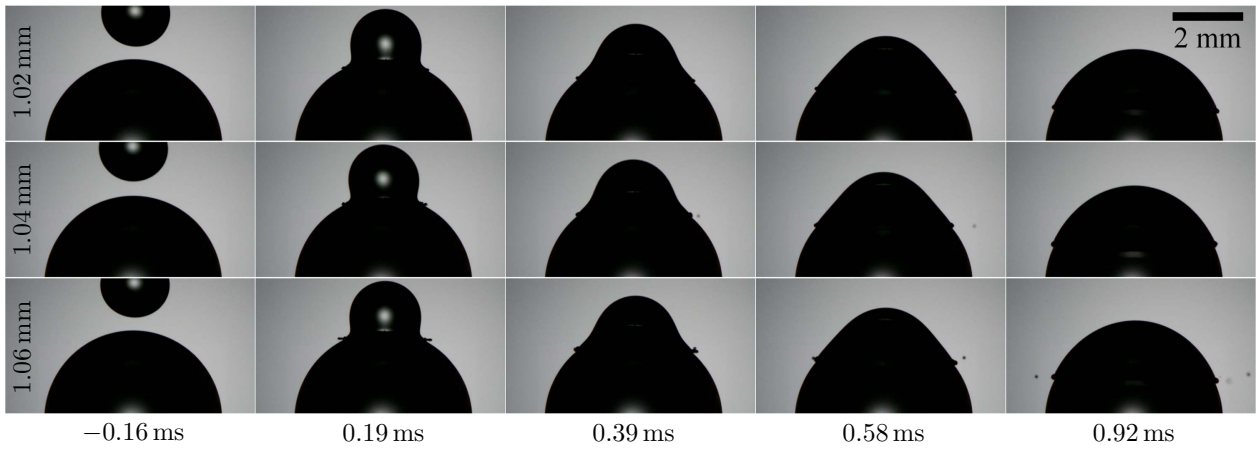

FIG. S2: A collection of three $r_n = 0.96\,\text{mm}$ droplets impacting a $r_s = 2.5\,\text{mm}$ sphere at $u = 2.40\,\text{m}\,\text{s}^{-1}$. Only r_c (indicated in each row) is varied between each row, spanning the splashing threshold: We = 412 (no splashing), We = 423 (one satellite droplet) and We = 430 (several satellites), respectively.

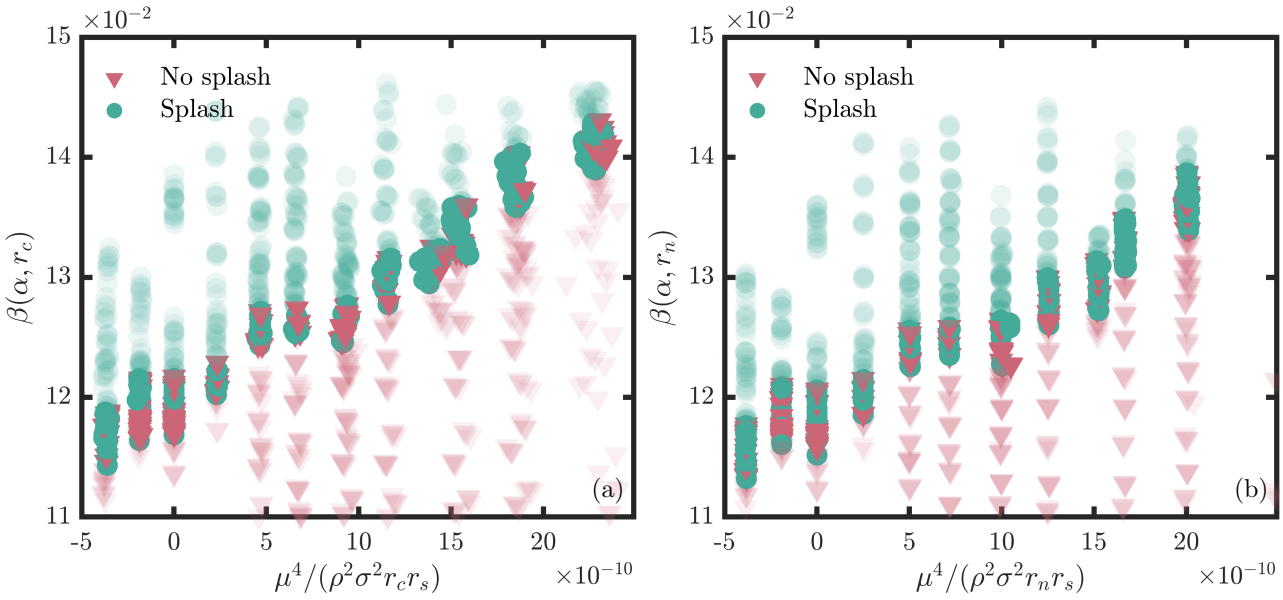

FIG. S3: Splashing propensity of (3.6 ± 0.3) µL and (4.85 ± 0.15) µL droplets, in terms of the (uncorrected) splashing ratio, $\beta(\alpha)$. (a) The length scale is r_c; the graph is a repeat of Fig. 3b in the main text. (b) The length scale is r_n.

$\beta(\alpha)$ and K) between these three experiments. However, using r_c enables the impact outcomes to be appropriately divided.

Figure. 3b (main text) also appears as Fig. S3a here. Recall that this graph is based upon the length scale r_c. For comparison, these data are replotted in Fig. S3b, using r_n as the length scale. Both graphs in Fig. S3 show the same qualitative trend, though they are quantitatively distinct. Note the lower random variation in r_n than r_c, which manifests as more clearly defined columns in the latter panel of Fig. S3. Nevertheless, the threshold regions are generally slightly extended when using r_n, further indicating the appropriateness of using r_c as the length scale in this work (i.e. the choice reduces the effective error).

§2. DETAILED EXPERIMENTAL INFORMATION

A. Droplet generation procedure

As noted in the main text, droplets were generated by dripping in this work. Since the substrate was spatially varying, precise control of the droplet impact position was required, unlike for geometrically and chemically-homogeneous substrates. To achieve impact velocities relevant to splashing, especially for the smaller spheres, the tip had to be positioned high above the substrate, which posed challenges in attaining and maintaining the desired impact position. The following procedures were employed to reduce the random variation in droplet impact position:

- An extra droplet was generated (and caught) immediately before each droplet was deposited onto the substrate, with the second droplet found to be more predictable in terms of impact position.
- The tip was covered by a loosely-fitting cylindrical pipe to protect the falling droplet from random air currents during its initial fall. Protecting the droplet's path closer to the tip (where its velocity was low) was found to be far more important than protecting its path close to the substrate, so an approximately $15 - 30$ cm telescopic tube was usually used.
- Dewetting of the tip during periods that the syringe pump was not active for more than a minute or so (e.g. during height changes or offloading data from the cameras) was found to greatly influence subsequent impact positions. Therefore, the syringe pump was programmed to activate for (4 ± 1) s in every 20 s when it would otherwise be inactive, in order to maintain the meniscus at the end of the tip and keep the tip wetted throughout.

Taken together, these procedures enabled adequate control of droplet impact positions.

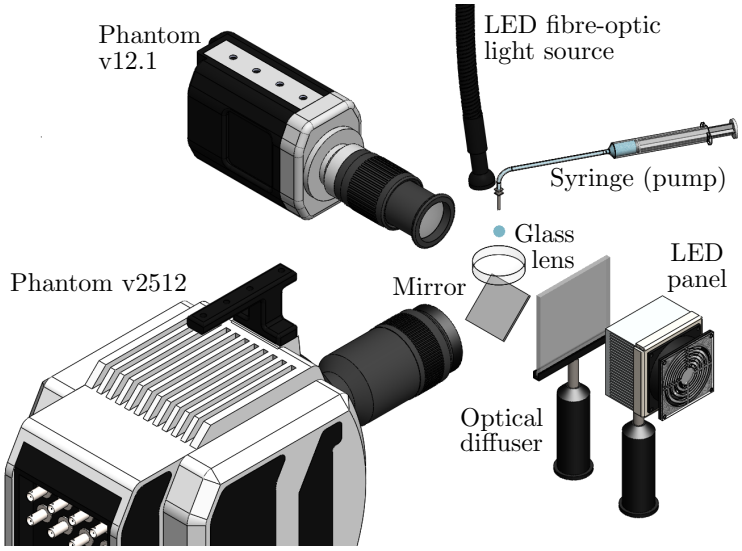

FIG. S4: A sketch (not to scale) of the experimental setup used for concave surfaces. The glass lens (concave substrate) was supported on a horizontal platform (not shown), in which a hole was cut to provide optical access.

B. Imaging

The cameras used in this work are detailed in the main text, which are the v2512, TMX 7510, Miro LAB310 and v12.1 (all Phantom high-speed cameras from Vision Research/AMETEK). Table S1 lists the lenses used with these cameras, alongside the pertinent imaging parameters (frame rate, effective resolution and exposure time). For all experiments, a 30 W LED array provided illumination via a ground glass diffuser to the v12.1/Miro, whilst a Photonic F5100 LED fibre-optic light source was used with a diffuser (except for the concave experiments) for the v2512/TMX.

C. Experimental setup for concave substrates

The experimental setup used for concave surfaces ($r_s < 0$) is shown in Fig. S4. A Phantom v2512 captured the impact and splashing dynamics from below (through the substrate) via an optical mirror, at up to 39,000 fps and with an effective resolution of 107 pixels mm^{-1}. Illumination for this camera was provided by an LED fibre-optic light source (Photonic F5100) positioned close to the dispensing tip, with the light path into the lens offset by a small angle (in the vertical plane) to the path of the falling droplet. To determine the droplet's geometry and impact velocity, a Phantom v12.1 was positioned perpendicular to the v2512 and captured the droplet as it fell into the lens, at up to 11,000 fps and with an effective resolution of 98 pixels mm^{-1}. Both cameras were kept horizontal, meaning that the latter lost sight of the droplet up to 7 mm above the substrate's apex. As for convex substrates, the impact velocity was determined from a second-order polynomial fit to the time series of the droplet's south-point height (relative to the substrate), evaluated at the substrate without the impact time needing to be known a priori. The impact velocities were found to be consistent with the $> 1,000$ convex substrate experiments in which the droplet could be seen up to and beyond the moment of impact at $t = 0$.

TABLE S1: Lenses and characteristics of the imaging configurations used in this work.

Camera	Lens	Ext. tubes (mm)	Frame rates (fps)	Effective res. (pixels mm^{-1})	Exposure (µs)
v2512	Nikon AF-S VR 105 mm f/2.8G	92 – 124	25,000 – 40,000	105 – 131	0.8 – 2.4 (convex) 20 (concave)
TMX		92	94,000	169	2.3
TMX	Navitar 12X Zoom Lens System[a]	0	76,000; 110,000	199	0.8 – 1.2
Miro	Nikon AF 60 mm f/2.8D	0	7,200	34	2.3
v12.1	Laowa 100 mm f/2.8 2x APO	20 – 36	10,200; 11,000	48 – 99	18 – 25

[a] Only used for qualitative data (no experiments using this lens are seen in the regime maps).

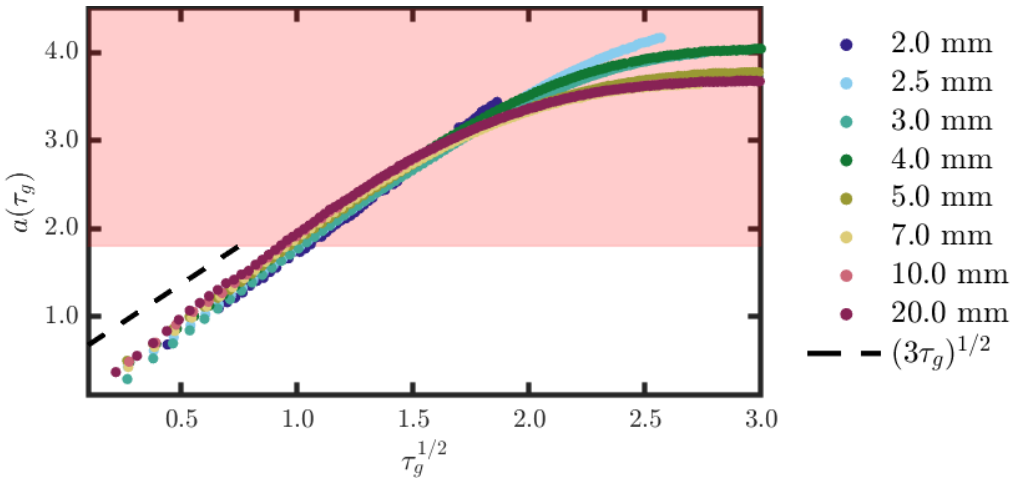

FIG. S5: Dimensionless half spread length, $a(\tau_g)$ of droplets spreading along the surface of a spherical substrate (r_s values are indicated in the legend) following axisymmetric impact at We $= 276 \pm 6$. Times τ_g are dimensionless with respect to the kinetic time scale using the droplet radius r_c as the length scale, r_c/u. The dashed line indicates the expected gradient for flat substrates – i.e. $(3\tau_g)^{1/2}$, translated upwards by 0.5 units for improved visibility. The red region indicates spread lengths beyond the expected point of breakup for experiments that splash.

§3. SPREADING OF DROPLETS ON SPHERICAL SUBSTRATES

For a flat substrate, the dimensionless half spread length of the droplet (in other words, the radius of the wetted area), a, is given by $a(\tau_g) = (3\tau_g)^{1/2}$, where $t/\tau_g = r_c/u$. The latter is the kinetic time scale based upon the droplet radius, rather than the diameter. The flat-substrate relation for a is derived from Wagner's theory, and has been extensively validated [3].

To check whether substrate curvature affects spreading in the period of interest for droplet splashing (i.e. before breakup occurs, if it would), we consider the time series of $a(\tau_g)$ for each spherical substrate studied. A representative We $= 276 \pm 6$ experiment for each such substrate is chosen, and $a(\tau_g)$ plotted against $\tau_g^{1/2}$ in Fig. S5. These Weber numbers are close to the splashing threshold for a flat substrate (so no experiment plotted splashes), chosen to reduce error in determining the contact line position (satellites and long extensive lamellae can obscure the true contact line – see Fig. 5a in the main text). Similar graphs can be observed for all Weber numbers studied. The red shaded region in Fig. S5 indicates spread lengths above which lamella breakup would have occurred (recall that $s = 1.9\,$mm from Sec. 3B), so this region is not of interest from the perspective of splashing thresholds.

Figure S5 shows that substrates of all (positive) curvatures studied have very similar spreading rates up to $a(\tau_g) \approx 2.5$, which is well into the red region of irrelevance to splashing thresholds. Moreover, the spreading dynamics at times of interest follow the expected $(3\tau_g)^{1/2}$ behaviour seen for flat substrates – see the dashed line (translated upwards by 0.5 units to improve its visibility) and compare its gradient to the data for spheres. Hence, substrate curvature appears not to affect spreading dynamics during the (relatively short) period of time relevant to splashing thresholds.

§4. LIST OF OTHER SUPPLEMENTARY MATERIAL

Figure 1 videos: fig1_{2,3,4,7,20}mm.mp4 and fig1_flat.mp4
Videos to accompany each experiment shown in Fig. 1. The videos cover dimensionless times $\tau \in [-0.3, 1.6]$ ($\tau \in [-0.3, 1.2]$ for the flat substrate) and play approximately 3,300x slower than real time. The width of each $r_s > 0$ video (in physical units) is matched to have a common effective scale. The substrate radius of curvature, r_s, is indicated in the file name of each video.

Regime map raw data: fig{3a,3b,6}_points.csv
Comma-separated value (CSV) files containing a list of our data points contained within each figure indicated in the file name. Each row corresponds to a different data point. The first column indicates the substrate's radius of

curvature (in millimeters) – 0 is used to identify flat substrates, for which $r_s \to \infty$; 300 identifies the larger droplet volume data, for which $r_s = 3.0\,\mathrm{mm}$. The final column indicates the splashing outcome in terms of MATLAB markers: 'v' indicates no splashing, whilst 'o' indicates splashing.

Regime map threshold data: fig{3a,3b,6}_thresholds.csv
CSV files containing the vertical axis values delineating each substrate's splashing threshold region for each regime map. The first column (substrate radius of curvature) follows the same conventions as for the raw data (see above).

---

[1] E. Li, M.-J. Thoraval, J. Marston, and S. T. Thoroddsen, Early azimuthal instability during drop impact, J. Fluid Mech. **848**, 821 (2018).
[2] A. Trujillo-Pino, K. Krissian, M. Alemán-Flores, and D. Santana-Cedrés, Accurate subpixel edge location based on partial area effect, Image Vision Comput. **31**, 72 (2013).
[3] G. Riboux and J. M. Gordillo, Experiments of drops impacting a smooth solid surface: A model of the critical impact speed for drop splashing, Phys. Rev. Lett. **113**, 024507 (2014).

Statement of Authorship for joint/multi-authored papers for PGR thesis

To appear at the end of each thesis chapter submitted as an article/paper.

The statement shall describe the candidate's and co-authors' independent research contributions in the thesis publications. For each publication there should exist a complete statement that is to be filled out and signed by the candidate and supervisor **(only required where there isn't already a statement of contribution within the paper itself).**

Title of Paper:	Droplet splashing on curved substrates
Publication Status	▪ Published
Publication Details	Sykes, T.C., Fudge, B.D., Quetzeri-Santiago, M.A., Castrejón-Pita, J.R. and Castrejón-Pita, A.A., 2022. Droplet splashing on curved substrates. *Journal of Colloid and Interface Science*, *615*, pp.227-235.

Student Confirmation

Student name:	Benjamin David Fudge
Contribution to the paper	Second Author, initial conceptualisation, ran ~50% of experiments, performed post-processing and analysis of corresponding data, presented results and visualisations, and co-wrote the manuscript.
Signature: 	**Date: 09/12/2022**

Supervisor Confirmation

By signing the Statement of Authorship, you are certifying that the candidate made a substantial contribution to the publication, and that the description described above is accurate.

Supervisor name and title: Prof. Alfonso A. Castrejon-Pita

Supervisor comments: Benjamin D. Fudge originally led the research contained in this chapter/article, including the very preliminary experiments that motivated us to continue working on it. During COVID-led lockdowns and subsequent restrictions, it was my duty to re-distribute duties and research focus to different members of staff/students in my group to maximise use of laboratories when they re-opened. This meant that while he kept working on this project, Ben's efforts were re-directed towards numerical work while it was impossible for more than one person to work in the lab an any one time (due to ongoing restrictions at the time). TCS and MAQS are PDRAs, who being more senior than students, acted as local laboratory co-leads during these difficult times. Ben continued running experiments and post-processing once restrictions were lifted, also contributing to the mathematical modelling, writing and editing the manuscript. Other authors provided supervision and funds to carry out this research.

Signature:  **Date: 09/12/2022**

6

Penetration Velocity of Droplet Impact onto a Film atop a Pool

Contents

6.1 Introduction

In the final exploratory chapter of this thesis we elaborate on the manuscript *"Drop impact onto immiscible films floating on deep pools"*, currently in draft format for future submission. This extends upon the work in chapter 3, where we now have a droplet impacting onto a thin film of a different liquid floating on top of a deep pool the same fluid as the droplet. This is of practical importance in scenarios such as rain droplets impacting onto oil slicks on water following an oil spill. Using the previous result as a reference we can consider two limiting cases, the first of which is the film thickness tending to zero and leading us to expect that the system should behave as if the film was not there. In the second case of infinite film thickness

we expect the underlying pool to no longer have any effect, as the film itself will behave as if it were a deep pool. Our results in fact indicate that this transition to where the underlying pool no longer has an effect actually occurs at a finite film thickness. This is in agreement with previous results in the literature, where threshold values for film thickness are found for other phenomena such as the crater depth post impact. Between these limiting cases however we observe a dependence of the penetration velocity on the film thickness, and we identify either an increase or decrease in the velocity with increasing thickness depending on the limiting cases. We also observe a deviation from the expected results for very small film thicknesses with the resulting velocity greater than either of the limiting cases, which we attribute to the interaction between the upper and lower film surfaces.

Further to the rich physical phenomena described above, in the case of a floating liquid film, there is an additional interface between the underside of the film and the deep pool whose dynamics will also depend on the film thickness. We investigate this motion and find a monotonic decrease in the velocity with increasing film thickness for all considered film velocities. We attribute this to the delay in the impact travelling through the increasingly thick film.

6.2 Publication: Fudge, Cimpeanu and Castrejón-Pita *"Drop impact onto immiscible films floating on deep pools"* draft paper

Drop impact onto immiscible films floating on deep pools

Ben D. Fudge,[1,*] Radu Cimpeanu,[2,3,†] and Alfonso A. Castrejón-Pita[1,‡]

[1] *Department of Engineering Science, University of Oxford, Oxford, OX1 3PJ, UK*
[2] *Mathematics Institute, University of Warwick, Coventry CV4 7AL, UK*
[3] *Mathematical Institute, University of Oxford, Oxford OX2 6GG,UK*

(Dated: January 9, 2023)

The interface dynamics of a droplet impacting onto a liquid pool has been well studied, and the common interfacial velocity quantified for the cases when the pool is both the same and a different fluid to the impacting droplet. In this work we investigate the scenario of a droplet impacting onto a pool of the same fluid coated by a film of another fluid of variable thickness both experimentally and computationally. The effect of the film thickness on the penetration velocity of both the upper droplet-film and lower film-pool interfaces are measured for experiments and simulations For the upper interface the velocity is compared to the limiting cases of zero film thickness-in which the film has no effect and thus behave like a fluid on same fluid impact- and infinite film thickness-in which the underlying pool has no effect. For finite film thickness cases we carefully quantify the transition between the two limiting scenarios, and provide insight into the interfacial and flow quantities of interest, with a robust transitional behaviour observed over a rich parametric landscape.

I. INTRODUCTION

The scenario of droplet impact onto thin films floating on deep pools is of great practical interest. Examples include raindrops hitting oil slicks on seawater can in fact spread the oil droplets much further than just the slick itself [1] or the manufacture of encapsulated drugs [2] in the context of advanced drug delivery systems. The introduction of a liquid film on top of an underlying deep pool adds another layer of complexity, and the possibility of further variation in parameters and resulting post-impact dynamics. Apart from the multiple liquid properties of both liquid phases, the studied multi-phase flow now includes the thickness of the film. Consequently, understanding the underlying dynamics of droplet-film-pool systems, and how varying the parameters such as the film thickness affects these dynamics, is of both fundamental and practical importance.

Previous work in this area has often focused of the dynamics of the post-impact 'crater' formation [3–5], with the particular case of Zhang *et al.* [5] identifying the formation of a double crown consisting of fluid from both the droplet and film for certain film thicknesses. Specifically they find an impact Weber number below which and a film thickness above which no double crown is formed, whilst in between these regimes the critical Weber number depends strongly on the film thickness, with thinner films requiring lower Weber numbers to produce a double crown. Furthermore they quantify the variation of various parameters such as both crown heights, the maximum crater volume and maximum height of the ejected jet with both the impact Weber number and film thickness providing an energetic model to explain these. Other related investigative directions include examining the formation of an air cavity behind a solid sphere impacting onto a film floating on a deep pool [6, 7] showing that an oil layer can prevent the usual sealing of the air cavity instead producing an emulsion of the oil in water, or the inverse case where an oil droplet rises in a liquid pool meeting an oil film on top and how a water layer can remain coating the droplet [8].

One particular case of interest is that of Kim *et al.* [4] finding that the maximum crater depth only depends on the film thickness for thicknesses up to $1.6\times$ the impacting droplet diameter, value above which it behaves as if it were an infinitely deep pool. In contrast to the work presented here and in other examples such as [5, 9] therein the droplet and the film consist of the same fluid and the underlying pool of a different fluid. They further suggest that miscibility between the droplet and film could have a potential effect into the dynamics of the droplet-film-pool motion noting that in previous examples without oil layers the validity of the theoretical prediction for the crater depth depends on the spreading coefficient between the fluids and not just the immiscibility property.

Given the complex landscape described previously, the focus of this work will therefore lie in the investigation of the early time dynamics of both the upper droplet-film and lower film-pool interfaces post-impact. In particular we concentrate on how the interfacial penetration speeds vary with the film thickness for different oil film viscosities, where for the upper interface the limiting thick film case would give penetration velocities both above and below the value predicted for same fluid impact, which is 1/2 that of the impacting drop velocity [10–14] whereas the immediate trend for the lower interface is less clear. We use a combination of high speed imaging experiments and high resolution direct numerical simulations (DNS) in order to find the speed of these common interfaces and carefully quantify their dependence on the film thickness for a variety of oils with different physical properties.

* benjamin.fudge@wadham.ox.ac.uk
† radu.cimpeanu@warwick.ac.uk
‡ alfonso.castrejon-pita@wadham.ox.ac.uk

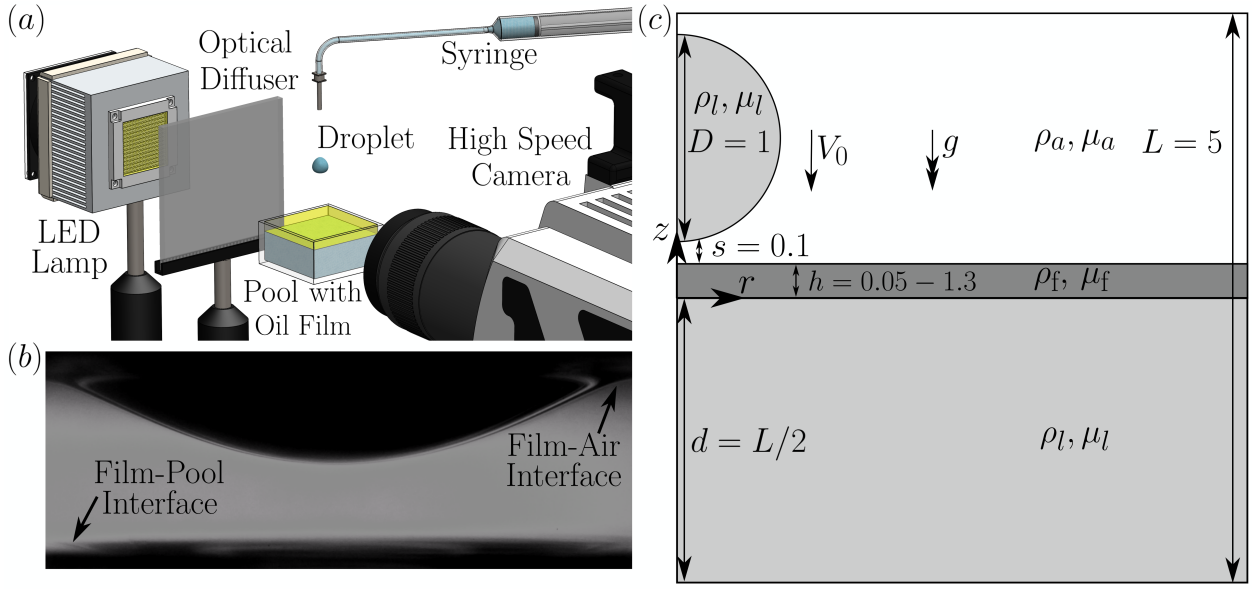

FIG. 1. (a) Diagram of the experimental system with the camera aimed at the underside of the upper layer in order to capture the displacement of the drop-film interface. (b) Example snapshot from the impact of a 2.6 mm diameter water droplet impacting at $0.58\,\mathrm{ms}^{-1}$ onto a 350 cSt silicone oil film showing the droplet penetrating into the film. At the bottom of the image the lower film-pool interface can be seen to be displaced slightly. (c) Simulation setup showing the distinction between the phases where the impacting droplet and pool are of the same fluid. The underlying pool depth is fixed at 2.5× the droplet diameter whilst the thickness of the layer on top is varied whilst maintaining the distance to the droplet fixed.

II. EXPERIMENT

Figure 1 (a) illustrates the experimental setup used for this work. The impacts are captured using a single camera setup consisting of a Phantom V2512 aimed at the underside of the top of the film to capture its displacement and thus the penetration velocity. Separate images are also recorded with the droplet falling at the same height in order to find the droplet impact speed and diameter. These impacts are captured at up to 50,000 frames per second and resolutions of up to 4μm per pixel. Figure 1 (b) shows an example snapshot from the impact of a 2.6 mm diameter water droplet onto a 350 cSt silicone oil film at $0.58\,\mathrm{ms}^{-1}$ from which we can see the displacement of the common droplet-film interface as well as the small displacement of the lower film-pool interface at the bottom of the image. The frames are extracted from the videos and post processed using the image processing toolbox in MATLAB in order to find the droplet impact parameters as well as the interface penetration speed. The pool container depth is greater than 10× the droplet diameter so we use a constant depth of pool fluid underneath to provide a constant baseline depth. On top of this a variable depth film is place with the droplet fall height adjusted to have a constant impact speed. The pool is deep enough to ensure that there are no effects due to the solid pool bottom.

For the experiments we use a pool and droplet consisting of water, as this configuration provides the best visualisation as we are able to achieve a 90° contact angle with the acrylic wall of the container when paired with a single viscosity silicone oil (350 cSt) film across a range of thicknesses from 0.05 to 1.3 times the droplet diameter, which was observed to be sufficient in order to examine the full range of variation for our quantities of interest and to validate the numerical results. In each case the impact consists of a 2.6 mm diameter water droplet impacting at $0.58\,\mathrm{ms}^{-1}$ onto a 350 cSt silicone oil film across the range of thicknesses considered.

III. DIRECT NUMERICAL SIMULATIONS

The direct numerical simulation framework is developed using the open-source solver Basilisk [15–17]. Our setup allowed us to systematically investigate the variance in the penetration velocity across a wide range of film thicknesses. For these we use a three-phase setup [14] in order to be able to independently vary the droplet and film properties in the presence of the surrounding air. In each case the underlying pool (which is the same fluid as the droplet) is fixed to be 2.5 times the droplet diameter to provide a constant underlying layer to eliminate any effects due to the finite depth of the pool. The film of variable depth is then on top of this as shown in Fig. 1 (c). Furthermore the domain size is sufficiently large in the lateral direction such that there are no effects such as wave reflections from the edge of the domain. In all cases the boundary conditions are solid impermeable no slip walls at the bottom and side of the domain with a

90 degree contact angle for the side, outflow at the top of the domain and axisymmetry along the centre. Adaptive mesh refinement is used with resolutions of up to level 12 corresponding to ~ 820 cells per droplet diameter with the adaptivity being based on errors in the interface location and velocity components. The simulations separately output both the top and bottom interfaces of the film in order to track their individual displacements, with the film thickness varying between 0.05 and 1.3 times the droplet diameter, in line with their experimental counterparts. For the simulations we use a pool and droplet of Fluorinert FC-770 and the films are silicone oils of either 20, 100 or 350 cSt viscosity. These values are chosen as they provide a wide range of penetration velocities both above and below the 1/2 value expected for same fluid impact, and thus we should be able to interrogate a significant variation as we change the film thickness. Simulations are also performed in the case that the pool and droplet both consist of water as cross-validation to the experimental results.

We note that our observations of the impact behaviour from our experiments indicate the axisymmetric nature of the results thus justifying our use of the axisymmetric solver here. For the parameters used herein a typical run required $\sim$15 CPU hours on 6 CPUs with approximately 100,000 grid points.

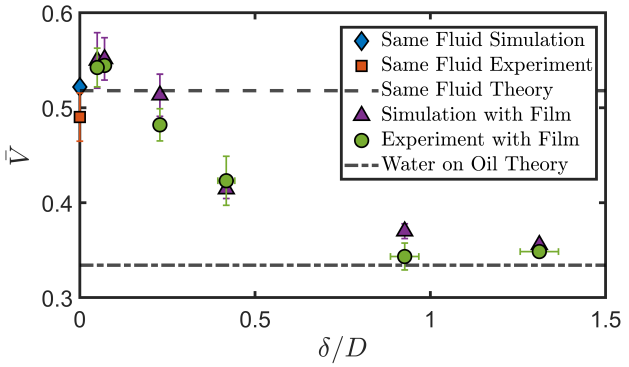

FIG. 2. Comparisons between experiments, simulation and theory (for the limiting cases of no film thickness and infinite film thickness i.e. just water on oil given by equation (1)) across a wide range of film thicknesses. In each case the impact consists of a 2.6 mm diameter water droplet impacting at 0.58 ms^{-1} onto a 350 cSt silicone oil film for both experiments and simulations corresponding to Re = 1470, We = 11.8 and Fr = 3.6. For the experiments the error bars in the x-direction account for uncertainty in the droplet diameter as well as film thickness and the error bars in the y-direction account for the uncertainty in the pool displacement speed and droplet impact speed. For the simulations the error bars in the y-direction correspond to uncertainty in the droplet impact speed and thus the parameters used in the simulation. In some cases the error bars are smaller than the point markers.

IV. EXPERIMENTAL-NUMERICAL COMPARISON

In order to validate the simulations we compare the experimentally measured penetration velocity to those predicted by their computational counterparts runs under the same parametric conditions. These results are displayed in Fig. 2, providing a summary of the penetration velocity against the normalised film thickness. The error bars in the experimental values correspond to uncertainty in the impacting droplet size and film thickness affecting the $x-$axis values and uncertainty in the droplet impact speed affecting the $y-$axis values. Reynolds, Weber and Froude numbers, defined respectively as $\mathrm{Re} = \rho_\mathrm{d}\mathrm{DV}_0/\mu_\mathrm{d}$, $\mathrm{We} = \rho_\mathrm{d}\mathrm{DV}_0^2/\sigma_\mathrm{d}$ and $\mathrm{Fr} = \mathrm{V}_0/\sqrt{\mathrm{gD}}$ where ρ_d, D, V_0, μ_d and σ_d are the droplet density, diameter, impact speed, viscosity and surface tension respectively and g is the acceleration due to gravity, for the corresponding simulation were set to the central value. To account for the experimental uncertainty (mostly due to the oscillations of the drop) we ran simulations at the averaged measured impact speed from the experiments, as well as $\pm 20\%$ the impact speed in order to give an estimate to the expected simulation value which are represented as the error bars in the simulation results in Fig. 2. Included is also the predicted penetration velocity in the limiting cases of infinite pool depth (for impacts onto both the same or different liquid) from the equation derived by Fudge *et al.* [14]. The results show a very good agreement between the experiments and the simulations within the experimental error confirming the expected trend of the penetration velocity varying between approximately 1/2 for a very thin film and that for a two-fluid setup for a very thick film. We note in both experiments and the simulations there is a slight overshoot above the 1/2 value for the smallest non-zero film thicknesses followed by a smooth decrease to an approximately constant value of $\bar{V} \sim 0.32$ for $\delta/D \geq 0.75$.

V. DISCUSSION

Complementing our experimental campaign, we now present the results of a comprehensive sweep of simulations across several film thicknesses in the range of $0.05 - 1.3$ times the droplet diameter of three different viscosity silicone oils (20, 100 or 350 cSt) for constant droplet impact conditions of Re = 1230, We = 69 and Fr = 4.8, which correspond to a 1.6 mm diameter FC-770 droplet impacting at 0.6 ms^{-1}. Table I presents the properties of these fluids as well as the expected penetration velocity for the impact of a FC-770 droplet onto a deep pool of each fluid at the conditions above given by equation (1) from Fudge *et al.* [14], namely

$$\bar{V} = \frac{1}{\sqrt{1 + 2.71\rho_r + \frac{24.4}{\mathrm{Re}}\mu_r}}. \qquad (1)$$

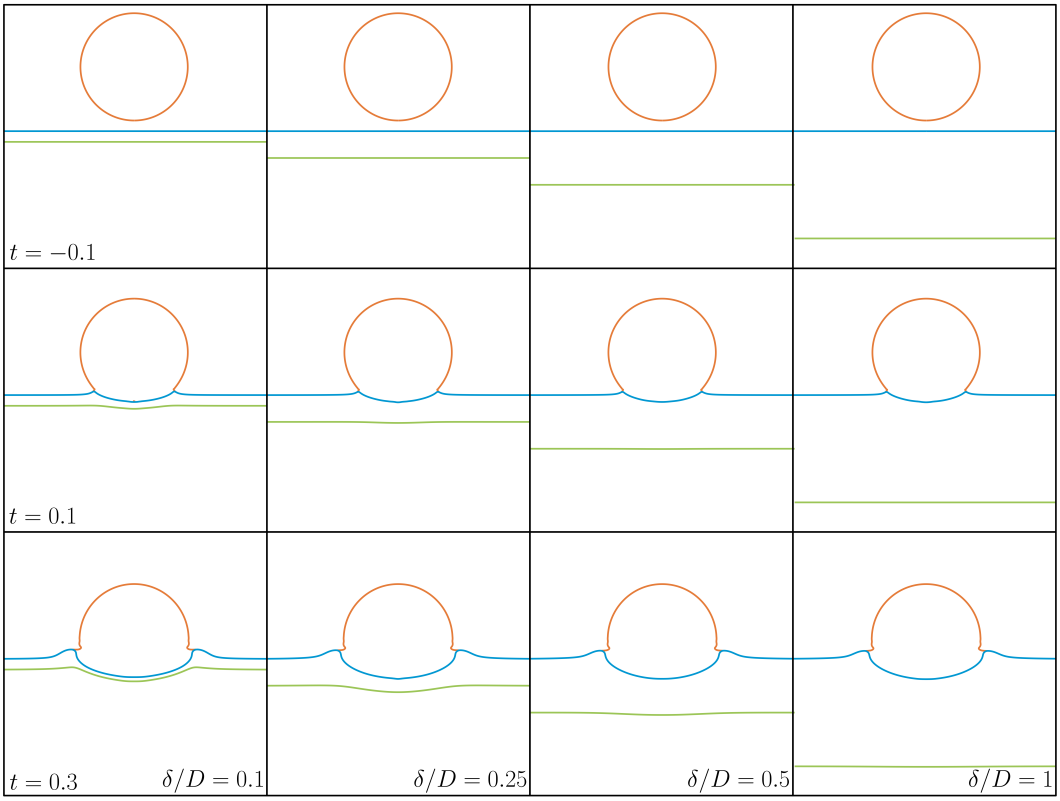

FIG. 3. Comparison between simulations at different film thicknesses for the case of a 20 cSt silicone oil film being impacted by a 1.6 mm diameter FC-770 droplet impacting at 0.6 ms^{-1} resulting in impact parameters of Re = 1230, We = 69 and Fr = 4.8. The thickness labels apply throughout each column and the time labels throughout each row with $t = 0$ corresponding to the theoretical impact time if neither the droplet or film deformed. In each case the droplet interface is depicted in orange, the film upper interface in blue and film lower interface in green. Note that this does not show the full simulation domain with the underlying pool thickness being the same throughout but cropped for clarity.

Here ρ_d is the pool to droplet density ratio, Re the Reynolds number based on the impacting droplet (fixed at 1230 for all cases here) and μ_r the pool to droplet viscosity ratio.

We anticipate observing differing trends for the three different viscosities. For the lowest viscosity (20 cSt), where the penetration velocity is greater than the same fluid impact counterpart, we expect to see a decrease in the penetration velocity towards ~ 0.5 as the film thickness decreases whereas for the highest viscosity (350 cSt) we expect to see an increase in penetration velocity as the film thickness decreases. For the intermediate viscosity case (100 cSt), where the predicted penetration velocity is approximately 0.5, we expect to see a constant penetration across all film thicknesses.

TABLE I. Properties of fluids used in the simulations. The fourth column presents the theoretical normalised penetration velocity from (1) for the impact of a 1.6 mm diameter FC-770 droplet at 0.6 ms^{-1} onto a deep pool of the given fluid (Re = 1230, We = 69 and Fr = 4.8).

Fluid	ρ (kgm^{-3})	μ (cP)	$\bar{V}$
20 cSt Silicone oil	953	19.1	0.607
100 cSt Silicone oil	960	96.0	0.512
350 cSt Silicone oil	968	338.8	0.371
Fluorinert FC-770	1793	1.4	0.518

Figure 3 shows the time evolution of the impact onto a 20 cSt film for four of the film thicknesses considered here, with each column representing a different thickness and time advancing down the rows with $t = 0$ corresponding to the theoretical time of impact if neither the droplet or the film deformed. In this case we expect the droplet film interface velocity to increase with increasing film thickness, which can be observed in the lowest row where the interface be be seen to have moved further down for the thickest film thickness compared to the thinnest one. From this figure we can also see how the motion of the lower interface varies with the film thickness with noticeable deformation visible for the lowest film thickness ($\delta/D = 0.1$) to only a slight dimple at late times for the medium thickness ($\delta/D = 0.5$) to no visible deformation for the thickest film ($\delta/D = 1$) visually showing the difference in the motion of the film for varying film thicknesses.

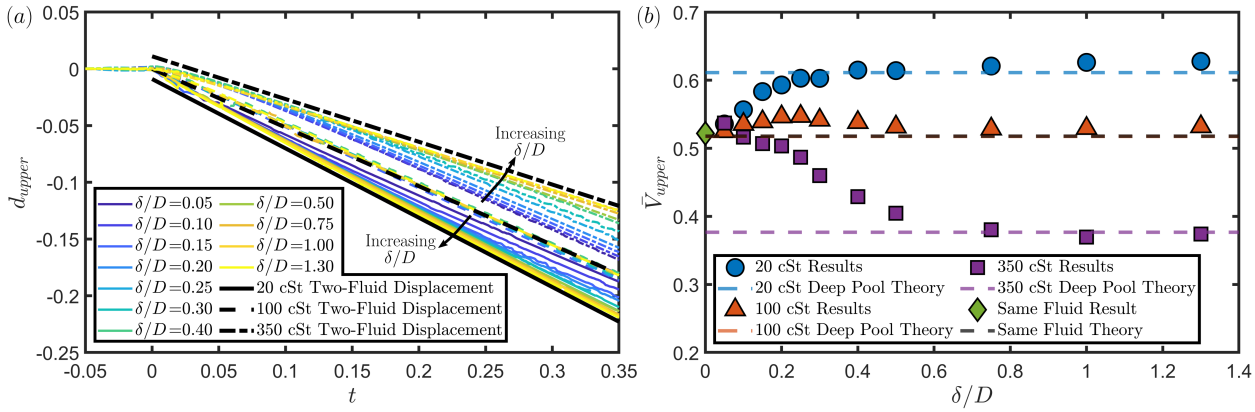

FIG. 4. (a) Displacement of the upper film interface against time for several different film thicknesses in the range $0.05 \leq \delta/D \leq 1.3$ for three different film viscosities (20, 100 or 350 cSt). In each case the impact conditions correspond to a 1.6 mm diameter FC-770 droplet impacting at 0.6 ms^{-1} resulting in impact parameters of Re = 1230, We = 69 and Fr = 4.8. The black solid, dashed and chain lines correspond to displacement at constant speed at the theoretical penetration velocity for impact onto a pool of the corresponding silicone oils (20, 100 or 350 cSt) respectively with the lines being offset for clarity. Note that at the parameters considered the predicted penetration velocity for the 100 cSt case is less than 0.1% different from that of the same fluid case and thus the dashed line can also be considered representative of the same fluid case. (b) Penetration velocity against the normalised film thickness for three different film viscosities extracted from the results in panel (a). Also included are dashed lines corresponding to the theoretical penetration velocity for impact onto a pool of the same silicone oil as the points of the same colour (corresponding to the black lines in panel (a)).

Figure 4 (a) shows the displacement against time of the upper film surface for normalised film thicknesses in the range $0.05 \leq \delta/D \leq 1.3$ for the three different film viscosities considered. From this we clearly observe the variation of the interfacial speed with the film thickness. Most notably for thicker films the lines are largely parallel to the corresponding lines for motion at the velocity predicted for the deep pool case (as shown by the black lines). The plot also confirms our expectation that increasing the film thickness will result in the penetration velocity tending towards the deep pool limit. We can see that for the 20 cSt film the velocity increases with increasing δ/D (the solid lines) and for the 350 cSt film the opposite is true (the chain lines). We also extract these velocities and present them in Fig. 4 (b) confirming this trend. What we can also see from the figure is that there is a threshold thickness of the film above which we no longer distinguish any further variation of the penetration velocity with the thickness at $\delta/D \approx 0.5-0.75$. This suggests that as this film thickness for the timescales considered here the film is thick enough to be considered a deep pool and we can in fact see from Fig. 4 (b) that above this thickness the measured penetration velocity is largely that predicted in the case of a deep pool of the oil (shown by the dashed lines). This is consistent with the results of Kim *et al.* [4] where they found that the maximum crater depth formed by a droplet impacting onto a film only varies with the thickness up to thicknesses of 1.6 times the impacting droplet diameter. Whilst we have a slightly different value of the threshold here, we note that it is of the same order of magnitude and that there are differences in the scenarios such as the impact conditions, fluid arrangements (here the droplet and film are immiscible whereas in [4] they are the same and the underlying pool different) and the timescales considered.

We also observe from Fig. 4 (b) that for small film thicknesses in the range $0.10 \leq \delta/D \leq 0.3$ there is a slight upwards deviation in the penetration velocity for the 100 cSt film case even though we expected it to be constant across all thicknesses at this viscosity. In fact a slight upwards deviation could also be considered for the 20 and 350 cSt cases at these thicknesses too noting that if all of the points were displaced to make the 100 cSt case constant the 20 and 350 cSt cases would result in fairly linear variances of the penetration velocities with thickness. This consolidates our earlier observation of this deviation at low film thicknesses in the experimental results as seen in Fig. 2 where we can see that for $\delta/D = 0.05$ and 0.07 the measured penetration velocity is larger than 0.5 for both the experiments and simulations performed. This leads us to suggest that there is an underlying mechanism in the film motion leading to a slight increase in the penetration velocity compared to what we would expect. While this merits additional investigation beyond the scope of the current investigation, our initial hypothesis is linked to a spring-like mechanistic interaction while the upper and lower interfaces are in close proximity to one another. In particular, the impacting drop providing energy into the liquid film produces an initial change in both velocity and pressure inside the film which will act (on a slightly delayed timescale) on the lower interface following an early compression stage with energy build-up. As the lower interface is eventually set in motion, a recoil effect providing additional downward

momentum to the entire liquid film region becomes noticeable. This is sufficient to further enhance the motion of the top interface as part of a delicate interplay between the two fluid surfaces. Access to both pressure and velocity profiles near the region of symmetry could inform a first reduced-dimensional model encapsulating the above dynamics, which we would anticipate providing qualitative (rather than quantitative) understanding of this phenomenon given some of the underlying model reduction procedures. It could nevertheless provide meaningful understanding at an analytical level that could underpin more accurate data-driven variants thereof.

We also turn our attention to the motion of the lower film-pool interface and its velocity. Figure 5 (a) shows the displacement of the lower interface for the single case of a 100 cSt film for all of the film thicknesses considered here. From this plot we can observe that there is a delay in the motion of the lower interface as the film thickness increases due to the time required for the motion of the impact to transfer through the film to the lower interface. For all of the cases we extract the penetration velocity which we take as the gradient of the straight line fitted to the final 0.1 time units of the motion as demonstrated for some of the film thicknesses in Fig. 5 (a) and present the results for all viscosities in Fig. 5 (b). From this figure we can see the general trend of the lower interface velocity decreasing with thickness for all film viscosities for the times considered here. We also note a minor but consistent variation of the velocity with the film thickness with the velocity increasing for increasing film viscosity. One potential explanation for this is that at higher film viscosities we expect the film to behave more solidly and thus transfer the motion through the film more strongly resulting in a faster lower interface motion. Also following on from the results in [18] we note that any upwards moving jet will be composed of a decreasing amount of pool following droplet impact for increasing pool viscosity so this would also result in a larger downwards speed for increasing film thickness.

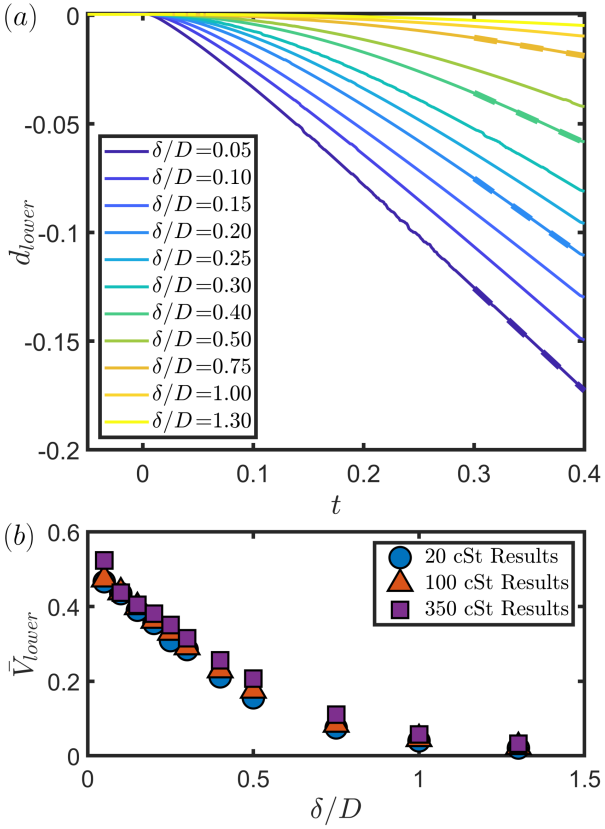

FIG. 5. (a) Displacement of the lower film interface against time for the single viscosity of 350 cSt for the same impact conditions as in Fig. 4. (b) Extracted penetration velocity for the lower film interface for all three considered viscosities (20, 100 or 350 cSt). In each case the velocity is taken as a straight line fit to the final 0.1 time units in the curves in panel (a) as demonstrated by the dashed lines for some of the cases.

VI. CONCLUDING REMARKS

In this work we have systematically investigated the penetration velocity of both the upper and lower interfaces of an oil film floating atop a deep pool impacted by a droplet of the same fluid as the pool. By using a range of oil film viscosities we have seen how increasing the film thickness can both increase or decrease the upper interface velocity depending on whether the deep pool limit of the oil film is greater or less than the 1/2 value for same fluids that we see when the film is very thin. The velocity tends towards the deep pool limit for increasing film thickness for all viscosities and analogous to the results of [4] we find that there is a limit of $\delta/D \approx 0.5 - 0.75$ above which the upper penetration velocity no longer changes, with the film behaving as if it were an infinitely deep pool analogous to previous results in the literature for the depth of the crater formed during impact [4]. We have also discovered that at low film thicknesses ($0.10 \leq \delta/D \leq 0.3$) we can observe a slight increase in the upper penetration velocity which we attribute to the interaction between the upper and the lower film interfaces.

Furthermore we investigated the motion of the lower film-pool interface, uncovering that for the times considered here the velocity decreases as the film thickness increases due to the time delay of the impact transferring through the film. We also found that the lower interface velocity only varies weakly with the oil film viscosity with a slight increase in the velocity with increasing viscosity which we attribute to the greater stiffness of the film causing larger bulk motion in the film.

By combining experimental results with high resolution three-phase simulations, as well as theoretical predictions for the impact onto deep pools [14], we have provided detailed insight into the dynamics of droplet impact onto a liquid film floating on a deep pool. Applications include mitigating oil spread after spills [1] or the manu-

facture of encapsulated drugs [2]. Further work will focus on the small deviation seen for small film thicknesses with a deeper sweep of the parameters in this regime to more fully investigate this effect, or more in depth modelling of the lower interface motion to incorporate its temporal evolution and effect on the full multi-liquid system.

[1] D. W. Murphy, C. Li, V. d'Albignac, D. Morra, and J. Katz, Journal of Fluid Mechanics **780**, 536 (2015).

[2] S. Yin, Y. Huang, X. Shen, C. Zhang, X. Chen, H. Li, T. N. Wong, *et al.*, Journal of Colloid and Interface Science **615**, 887 (2022).

[3] M. Mohasan, A. B. Aqeel, P. Lv, Y. Yang, and H. Duan, Acta Mechanica Sinica **37**, 447 (2021).

[4] D. Kim, J. Lee, A. Bose, I. Kim, and J. Lee, Journal of Fluid Mechanics **906** (2021).

[5] X. Zhang, C. Wang, and S. Rui, European Journal of Mechanics-B/Fluids **92**, 65 (2022).

[6] B. C.-W. Tan and P. J. Thomas, Physics of Fluids **30**, 064104 (2018).

[7] L. B. Smolka and C. K. McLaughlin, Physical Review Fluids **4**, 044001 (2019).

[8] O. Ram and J. Katz, Chemical Engineering Journal **387**, 124075 (2020).

[9] W. Wang, C. Ji, F. Lin, X. Wei, and J. Zou, Physics of Fluids **31**, 037107 (2019).

[10] T. Tran, H. de Maleprade, C. Sun, and D. Lohse, J. Fluid Mech. **726** (2013).

[11] M. H. Hendrix, W. Bouwhuis, D. van der Meer, D. Lohse, and J. H. Snoeijer, J. Fluid Mech. **789**, 708 (2016).

[12] X. Tang, A. Saha, C. K. Law, and C. Sun, Langmuir **34**, 2654 (2018).

[13] Z. Jian, M. A. Channa, A. Kherbeche, H. Chizari, S. T. Thoroddsen, and M.-J. Thoraval, Phys. Rev. Lett. **124**, 184501 (2020).

[14] B. D. Fudge, R. Cimpeanu, and A. A. Castrejón-Pita, Physical Review E **104**, 065102 (2021).

[15] S. Popinet, Journal of Computational Physics **190**, 572 (2003).

[16] S. Popinet, Journal of Computational Physics **228**, 5838 (2009).

[17] S. Popinet, Journal of Computational Physics **302**, 336 (2015).

[18] B. D. Fudge, R. Cimpeanu, A. Antkowiak, J. R. Castrejón-Pita, and A. A. Castrejón-Pita, Journal of Colloid and Interface Science (JCIS (submitted) 2022).

Statement of Authorship for joint/multi-authored papers for PGR thesis

To appear at the end of each thesis chapter submitted as an article/paper.

The statement shall describe the candidate's and co-authors' independent research contributions in the thesis publications. For each publication there should exist a complete statement that is to be filled out and signed by the candidate and supervisor **(only required where there isn't already a statement of contribution within the paper itself).**

Title of Paper:	Droplet impact and penetration velocity of floating immiscible oil layers on a deep pool (provisional)
Publication Status	▪ Unpublished and unsubmitted work written in a manuscript style
Publication Details	Fudge, B.D., Cimpeanu, R. and Castrejón-Pita, A.A. Droplet impact and penetration velocity of floating immiscible oil layers on a deep pool (provisional)

Student Confirmation

Student name:	Benjamin David Fudge
Contribution to the paper	Lead Author, performed all numerical simulations, analysed and presented experimental and numerical results, performed theoretical modelling, and writing and editing of manuscript
Signature: 	**Date: 09/12/2022**

Supervisor Confirmation

By signing the Statement of Authorship, you are certifying that the candidate made a substantial contribution to the publication, and that the description described above is accurate.

Supervisor name and title:
Supervisor comments Benjamin D. Fudge led and carried out the research contained in this chapter/article. Other authors provided formal supervision (AACP, RC) and funds to carry out the research.

Signature: 	**Date: 09/12/2022**

7 Discussion and Conclusion

Contents

In this thesis we have investigated various phenomena related to droplet impact, focusing largely on how the substrate properties (such as viscosity for a liquid substrate or curvature for a solid one) affect the outcome of the impact (for example the penetration velocity or whether splashing occurs). In this final chapter we will now summarise the key findings of this work, as well as the main contributions made to the field. For each individual research thread we also highlight future developments that could be made to build upon the work, while also identifying new opportunities for further research.

7.1 Penetration Velocity

In chapters 3 and 6 we investigated the penetration velocity of the common droplet-pool and droplet-thin film interfaces respectively. Building on initial energetic

modelling in the literature for same fluid impacts where we expect a penetration velocity of one half the impacting droplet velocity [46, 51, 52], we introduced differences between the droplet and pool fluids. The contrast in density was introduced by accounting for the pool density when finding the kinetic energy of the motion of the pool. To account for the pool viscosity we used a simple scaling argument for the viscous dissipation in the pool depending on a fitting parameter, which we then included in the overall energy balance. By performing numerical simulations across a large range of data across several different density and viscosity ratios, as well as impact speeds, we were able to fit the model to the produced data. From the provided values of the fitting parameters we found an explicit equation for the penetration velocity as a function of the density and viscosity ratios and impact Reynolds number. This model showed very good agreement to the experimental and numerical data in the work, spanning over an order of magnitude in both density and viscosity ratios, as well as results reported in the literature for differing fluid cases [71]. Furthermore in our later work on viscous splashing in chapter 4, we tested the validity of the penetration velocity equation for much higher impact speeds and viscosity ratios. The results verified that the model continued to agree well with experimental and numerical results even at viscosity ratios up to 10^5, and was consequently a key piece in explaining the results therein.

Chapter 6 built upon these results and extended them to a new case whereby we had a droplet impacting onto a deep pool of the same fluid coated with a thin film of a different fluid. In this case we considered the two limiting scenarios of zero and infinite film thicknesses, which devolved into two simple cases of the above scenario where the fluids are either the same (for zero film thickness) or are the droplet and a deep pool of the film (for infinite film thickness). We showed how, depending on these two limiting cases, we may observe either an increase or decrease in the velocity of the droplet-upper film interface as we increase the film thickness for different film viscosities. We did note however a deviation in the results for small but non-zero film thicknesses where a penetration velocity larger than either of the limiting cases was observed. We attributed this to interactions between the upper and lower film

interfaces only possible at these small thicknesses. Furthermore we investigated the motion of the lower film-pool interface showing a delay in the motion caused by the film thickness, as well as a weak dependence on the film viscosity attributed to the effective stiffness of the film transferring the motion to the lower interface.

One potential extension of this area of work could be a greater investigation of the penetration for cases where the droplet is more viscous that the impacted pool. Whilst the model in chapter 3 included the viscous dissipation in the pool it does not include dissipation in the droplet. Attempts to include this dissipation however, resulted in a poorly fitted model that did not agree well with the observed results. This could be due to the fact that the amount of energy dissipated in the droplet is largely constant across the range of parameters considered, thus producing an poorly conditioned fitting. In Appendix C of the paper however, we observed that at low pool viscosities the percentage of the total viscous dissipation occurring in the droplet actually became significant (being $\sim 75\%$ of the total dissipation for a viscosity ratio of 0.0625). Consequently one aspect of future work in this area could be the incorporation of the viscous dissipation in the droplet to the model in order to improve its performance at low viscosity ratios. Furthermore, we noted in the modelling section that by relaxing the assumptions about the flow field in the pool, the prefactor of 3 in front of the density ratio could be changed to be a general parameter to be found. Further work therefore could focus on more detailed modelling of the flow field in the pool to explain the modified value found by the fitting and whether it can be achieved robustly in a generalisable manner. One final inclusion could be to also account for the changing surface energies in the energetic balance which was assumed to be negligible, but could become significant in the case of large scale droplet deformation or large interfacial tensions.

7.2 Splashing on a Viscous Pool

Chapter 4 presented the results of the impact of a droplet onto a deep immiscible viscous pool with a range of viscosity ratios from $\mathcal{O}(1)$ to $\mathcal{O}(10^6)$, investigating how the threshold to splash varied with the viscosity ratio. We identified two different

regimes, a low pool viscosity regime (pool to droplet viscosity ratios less than ~ 35) where the threshold to splash increased with pool viscosity and the splash originates from the pool fluid, and a high pool viscosity regime (pool to droplet viscosity ratios greater than ~ 35) where the threshold to splash decreased with the pool viscosity and the splash originates from the droplet. These two regimes were separated by a remarkable point (at a viscosity ratio of approximately 35) where no splashing was observed at any achievable impact speed in the laboratory experiments nor in numerical simulations (albeit axisymmetric) at the terminal velocity. We explained the differing origin of the splash by building upon previous results [41], quantifying the composition of the ejected jet between droplet and pool fluids for several values around the critical viscosity ratio. Here we found a transition between a jet consisting almost entirely of pool fluid to one entirely of droplet fluid in this non-splashing regime.

Furthermore, noting that in the high pool viscosity regime the splash originated from the droplet, we followed on ideas from previous work considering splashing on soft solids [27]. By combining the ideas therein with the results from chapter 3 on the velocity of the common droplet pool interface, we were able to quantify the reduction of the maximum pressure in the droplet due to the cushioning effect of the pool motion. The use of the equation for the penetration velocity to find the maximum pressure was then found to successfully collapse all the pressure curves across the different viscosities onto a single curve, predicted by Wagner theory. Using this result, in conjunction with the notion that in order to splash we need the maximum pressure in the droplet to exceed a certain threshold to splash, we were able to derive an equation determining the critical speed required to splash. This equation showed excellent agreement with the experiments results in this regime, especially for viscosity ratios greater than 3,000. Some deviation between the experimental and theoretical results was observed below these viscosity ratios, with the equation overpredicting the splashing threshold. We theorised this may be due to the droplet-pool interface not reaching the predicted constant theoretical speed. This has the consequence that the pressure reduction is less

than predicted by the theoretical model leading to splashing occurring sooner than expected. Consequently, future work in this area could focus on the early time dynamics of the droplet-pool interface in order to find a temporal dependence of the interface velocity, and thus a more accurate prediction of the pressure reduction in the droplet at the times relevant for splashing.

We also pursued a theoretical incursion into the splashing threshold for the lower viscosity pools, noting that this time the maximum pressure in the pool is of importance, as this is where the splash originates from. By considering a force balance on an element of fluid at the root of the jet from which the splash is ejected, we noted that the driving force of the jet (the pressure in the pool) is opposed by a resisting force (the viscous dissipation in the pool). From our numerical results we demonstrated that the maxima of both occur at the root of the jet. Therefore in order for this jet to form and lead to a splash we required the maximum pressure in the pool to exceed the maximum viscous dissipation. Our numerical results in this regime showed that the maximum pressure in the pool is largely constant, and that the maximum viscous dissipation increased (largely linearly) with the pool viscosity. This explained our observation that the threshold to splash increased with pool viscosity as the jet is opposed by increasingly strong viscous dissipation but driven by a largely constant pressure. In this work however we did not develop a theoretical framework for the values of these opposing forces in the production of the jet due to the challenges of deriving the complicated flow fields within the jet root. Thus future work could be conducted into modelling the jet root flow in this regime. This would allow the quantification of the variance of the pressure and viscous dissipation to derive a condition for the splashing threshold similar to that found for the high viscosity case.

7.3 Splashing on Curved Surfaces

In chapter 5 we investigated the impact of droplets onto solid surfaces focusing on how the splashing threshold depended on the surface curvature for both convex (spheres) and concave (lenses) surfaces. For both cases we observed an increase in

the splashing threshold for increasing positive curvature. That is, smaller spheres resulted in an increased threshold to splash, and more strongly curved lenses (which have a negative curvature and thus an increasing value means a flatter lens) have a decreased threshold to splash. In contrast to previous work, we plotted the splashing threshold against the reciprocal of the product of the droplet and surface radii of curvature (specifically $1/r_d r_s$ where r_d and r_s are the droplet and surface radii of curvature) instead of simply the ratio of the radii. This was due to the fact increasing either of these values has the same effect as larger droplets are more likely to splash as are impacts onto surfaces larger radius of curvature. Consequently if using the ratio of the radii one could increase both by the same factor and obtain the same ratio and yet the splashing threshold would not be the same. Non-dimensionalising the reciprocal product as defined above resulted in a compound Ohnesorge number based on both the droplet and surface curvature.

We explained the observed variation of the splashing threshold with the surface curvature using a recently developed theoretical framework [54] to model droplet splashing on solid surfaces, taking into account the effect of the surrounding air. Specifically one parameter of interest was the wedge angle between the spreading droplet lamella and the surface, whose value was depended on in the splashing parameter but was always taken as a constant for flat surfaces. We showed however, that for curved surfaces this wedge angle is altered by the surface curvature, being increased for convex surfaces as the surface curves away from the spreading droplet or decreased for concave surfaces as it curves towards the droplet. This then affected the air motion whereby for the convex surfaces the air is able to "escape" from underneath the lamella down the curving surfaces, reducing the lift effect on the lamella and thus its tendency to break up and splash, with the reverse true for the concave surface. Through a combination of geometrical reasoning and results from the experiments, we were able to find a functional relationship between the substrate curvature and the effective wedge angle between the spreading droplet and surface. Using this effective wedge angle in the splashing criterion then collapsed the data for all curvatures onto one single threshold thus capturing the effect of the curvature.

Furthermore we noted that, unlike impact onto flat surfaces where it does not matter where on the surface the droplet impacts, for curved surfaces the result could be significantly affected depending on where on the surface the impact occurs. Whilst impacting exactly on the centre of the curved lens or sphere resulted in axisymmetric dynamics, when impacting off centre there was a spatial variation as some parts will be travelling upwards and other downwards, similar to impact on inclined surfaces. The results indicated that in the transition region, where both splashing and non-splashing occur, the effect of a large offset was to enhance splashing. Specifically we noted that splashing was enhanced in the downward direction and reduced in the upward direction, in agreement with the results in the literature for impacts on inclined surfaces. When considering the substrate curvature however, this appeared to disagree with the general result found for the effect of the curvature. This is because in the uphill direction the effective wedge angle is decreased, which was shown to enhance splashing, and yet in the non-axisymmetric case splashing was reduced in this direction. This suggests some additional effect due to the inclined impact, which could be the focus of future work in this area to quantify the effect of non-axisymmetry as well as substrate curvature. Previous work in the literature has investigated such inclined impacts [20, 57, 58], and could act as a foundation for such further work. Finally, one specific challenge of the work was imaging the impact of droplet onto concave lenses due to the curvature of the lens obscuring the point of impact. Future investigations in this area could thus implement a different imaging approach, for example having a camera aimed from above at an oblique angle, to allow better imaging of the dynamics within the lens to provide further insight.

7.4 Future Work: Impact and Splashing Threshold of Rotating Droplets on Liquid Pools

As part of previous work on droplet impact onto solid surfaces, tangential components of velocity relative to the surface and their effect on the impact dynamics and thus the splashing threshold have been considered [57–59]. The usual way to

introduce such a tangential component is to impact the surface at an oblique angle [57, 58] or to have the surface itself moving [59]. Another, and less well explored, way is to have the droplet itself be rotating prior to impact. Considering a case where the droplet is rotating about an axis parallel to the flat surface (as if the droplet rolled off of a surface before falling down) one side of the droplet will have a greater impact speed (the one rolling into the surface) than the other, resulting in non-axisymmetric motion. Figure 7.1 shows an example of this, where a 3.4 mm water droplet is impacting onto a deep water pool at $1.9\,\mathrm{ms}^{-1}$ with zero rotational speed in panel (a) and whilst rotating at a speed of 10 Hz clockwise in panel (b). We note that at this rotational speed the resulting linear speed at the edge of the droplet is $0.11\,\mathrm{ms}^{-1}$, or approximately 5.6% the falling speed of the droplet.

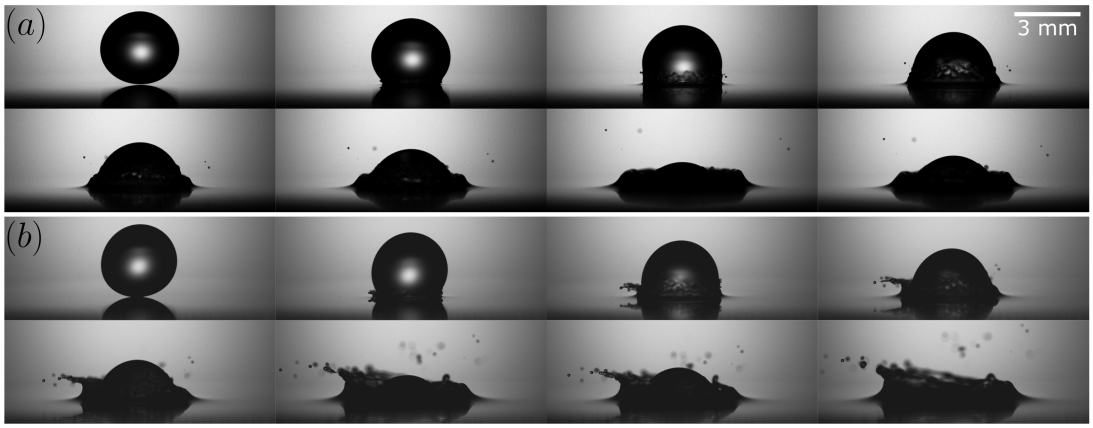

Figure 7.1: Time sequence of a 3.4 mm water droplet impacting onto a water pool at $1.9\,\mathrm{ms}^{-1}$ (a) With no rotation and (b) With a rotational speed of 10 Hz clockwise. The scale bar in the top right image applies throughout and each frame is $40\,\mu$s apart.

From this there is a clear difference introduced by the, relatively minor, rotational speed. For the non-rotating case in panel (a) we can observe that there is a largely axisymmetric lamella ejected at the point of impact which rapidly breaks up into many smaller droplets whilst the bulk of the pool smoothly moves upwards forming a crown. The rotating case in panel (b) however displays remarkably different dynamics, with the left hand side where the droplet is rotating away from the pool exhibiting a strongly formed and almost horizontal lamella that disintegrates into many droplets. On the right hand side where the droplet is rotating into the pool,

there is a much less prominent lamella formed with it only slightly appearing on the side of the droplet. This is to be expected however, as the flow field caused by the rotation will transport fluid from the inwards rotating direction to the outwards direction. This is however somewhat contradictory with the results discussed above for impact onto inclined surfaces where splashing is enhanced in the downwards (and thus faster direction). Here instead, the rotation of the droplet actually decreases the vertical component of the speed in the upwards direction and yet this is where there is enhanced splashing. One potential explanation for this is the bulk transfer of fluid along the underside of the droplet mentioned above causing a stronger (and more horizontal) jet in this direction. We can also notice a significant change in the shape of the crown of fluid produced at later times with it being higher on the outwards direction and much more irregular and breaking up into smaller droplets unlike in the non-rotating case.

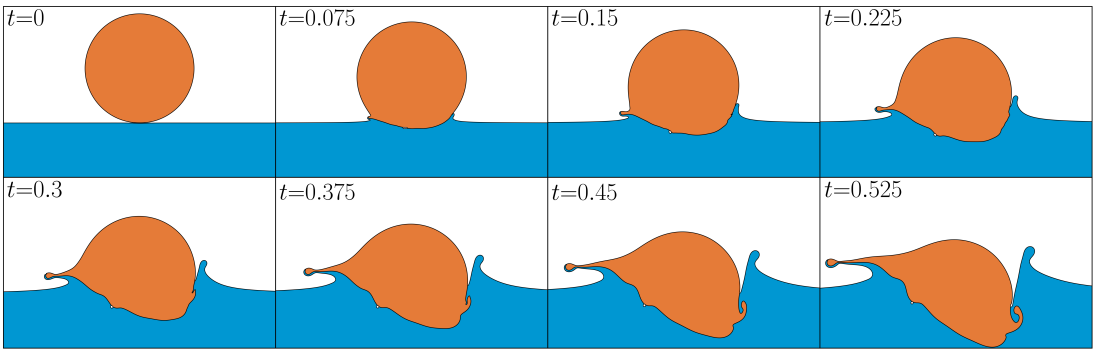

Figure 7.2: Example 2D simulation of a rotating droplet impacting an immiscible pool at Re=1000, We=200 and Fr=10 and non-dimensional rotational speed of 0.5 clockwise with pool to droplet density and viscosity ratios of 0.52 and 1.33 respectively. Note that t=0 corresponds to the theoretical time of impact if neither the droplet or pool deformed. The small white dot between the droplet and pool is an entrapped air bubble.

Furthermore we have conducted preliminary numerical simulations of rotating droplets confirming the features observed in these experiments. In Fig. 7.2 we present the result of a 2D simulation of a rotating droplet impacting an immiscible pool with parameters Re=1000, We=200 and Fr=10 rotating clockwise at a dimensionless speed of 0.5. We also note that this combination of parameters did not result in splashing unlike those seen in the experiments in Fig. 7.1. Whilst the simulation is not fully 3D due to the additional computational complexity and corresponding

cost to run, it highlights some important common features when compared with the experiments. Most notable is the clear difference between the lamellae either side of the droplet. On the left hand side where the droplet is rotating out of the pool the lamella is more strongly formed and largely horizontal, whereas in contrast the right hand lamella is much smaller and oriented more to the vertical. Both of these are phenomenological very similar to what is seen in the experiments and therefore numerical simulations, potentially even just 2D ones, could provide meaningful insights into the dynamics of rotating droplets.

From these early results we therefore find that even relatively small rotational speeds, compared to the impact speed of the droplet, can significantly affect the resulting post-impact dynamics. We observed a spatial variation in the tendency to splash where splashing can be enhanced or suppressed depending on the side of the drop and its corresponding direction of rotation. Future work in this area could be conducted in order to systematically investigate how this effect varies with the rotational speed, in addition to understanding the underlying mechanism for this.

7.5 Closing Remarks

As part of this thesis we have investigated droplet impact problems experimentally, computationally, and mathematically in order to explain the effects of different parameters on the impact outcome. We have shown how differing properties between the impacting droplet and impacted substrate, be it solid or liquid, can influence the motion of a common droplet-pool interface or the tendency to splash. One area of investigation was how the splashing threshold varies for impact onto both concave and convex curved surfaces. We found a single mechanism explaining the trend observed for both surfaces, and the subsequent results proved to be consistent with theoretical arguments proposed in the literature. Furthermore we also explored the effect of asymmetry on the impact, an additional factor not applicable for impact onto flat surfaces.

For the case of impact onto a liquid pool, we derived a model for the common droplet-pool interface depending on differences in density and viscosity between the

droplet and pool. We verified it both experimentally and computationally across a wide range of density and viscosity ratios finding excellent agreement between the results and theory. We also extended this setup to the case of a thin film floating on a deep pool, finding an additional dependence on the film thickness up until a limit where it behaves as if a deep pool. Whilst the result for the penetration velocity is significant in itself, we then proceeded to show how knowledge of the motion of the drop and pool post impact can be used to explain the variation in the transition to splashing as a droplet impacts onto a pool of varying viscosity. The deformation of the pool cushions the impacting droplet reducing the pressure in the pool and thus the likely hood of splashing similar to that observed in impacts onto soft solids. Knowledge of whether a droplet impact results in a splash can be of great importance in many applications such as disease control or inkjet printing, so the predictive capabilities derived as part of this thesis can be used to improve these processes and thus achieve better and more controllable results. Furthermore whilst here we have used the result for the penetration velocity to derive the splashing threshold on viscous pools, it remains to be seen what further phenomena could be explained through understanding the motion of the common droplet-pool interface or the underlying droplet dynamics leading to splashing.

References

[1] S Kim et al. “Vortex-induced dispersal of a plant pathogen by raindrop impact”. In: *Proc. Natl. Acad. Sci. U.S.A.* 116.11 (2019), pp. 4917–4922.

[2] S Lejeune and T Gilet. “Drop impact close to the edge of an inclined substrate: Liquid sheet formation and breakup”. In: *Phys. Rev. Fluids* 4.5 (2019), p. 053601.

[3] L Bourouiba. “Turbulent gas clouds and respiratory pathogen emissions: Potential implications for reducing transmission of COVID-19”. In: *Jama* 323.18 (2020), pp. 1837–1838.

[4] D Lohse. “Fundamental fluid dynamics challenges in inkjet printing”. In: *Annu. Rev. Fluid Mech.* 54 (2022), pp. 349–382.

[5] SD Hoath. *Fundamentals of inkjet printing: the science of inkjet and droplets*. John Wiley & Sons, 2016.

[6] C Josserand and ST Thoroddsen. “Drop impact on a solid surface”. In: *Annu. Rev. Fluid Mech.* 48 (2016), pp. 365–391.

[7] DW Murphy et al. “Splash behaviour and oily marine aerosol production by raindrops impacting oil slicks”. In: *J. Fluid Mech.* 780 (2015), pp. 536–577.

[8] D Attinger et al. “Fluid dynamics topics in bloodstain pattern analysis: comparative review and research opportunities”. In: *Forensic Sci. Int.* 231.1-3 (2013), pp. 375–396.

[9] AM Worthington. “XXVIII. On the forms assumed by drops of liquids falling vertically on a horizontal plate”. In: *Proc. R. Soc. Lond.* 25.171-178 (1877), pp. 261–272.

[10] HE Edgerton and JR Killian. *Flash!: Seeing the unseen by ultra high-speed photography*. CT Branford Company, 1954.

[11] ST Thoroddsen, TG Etoh, and K Takehara. “High-speed imaging of drops and bubbles”. In: *Annu. Rev. Fluid Mech.* 40 (2008), pp. 257–285.

[12] CD Stow and MG Hadfield. “An experimental investigation of fluid flow resulting from the impact of a water drop with an unyielding dry surface”. In: *Proc. R. Soc. Lond.* 373.1755 (1981), pp. 419–441.

[13] CHR Mundo, M Sommerfeld, and C Tropea. "Droplet-wall collisions: experimental studies of the deformation and breakup process". In: *Int. J. Multiph. Flow* 21.2 (1995), pp. 151–173.

[14] S Gart et al. "Droplet impacting a cantilever: A leaf-raindrop system". In: *Phys. Rev. Appl.* 3.4 (2015), p. 044019.

[15] PB Weisensee et al. "Water droplet impact on elastic superhydrophobic surfaces". In: *Sci. Rep.* 6 (2016), p. 30328.

[16] X. Huang et al. "Droplet impact induced large deflection of a cantilever". In: *Phys. Fluids* 31.6 (2019), p. 062106.

[17] MJ Negus et al. "Droplet impact onto a spring-supported plate: analysis and simulations". In: *J. Eng. Math.* 128.1 (2021), pp. 1–27.

[18] JC Bird, SSH Tsai, and HA Stone. "Inclined to splash: triggering and inhibiting a splash with tangential velocity". In: *New J. Phys.* 11.6 (2009), p. 063017.

[19] J Hao et al. "Droplet splashing on an inclined surface". In: *Phys. Rev. Lett.* 122.5 (2019), p. 054501.

[20] P García-Geijo, G Riboux, and JM Gordillo. "Inclined impact of drops". In: *J. Fluid Mech.* 897 (2020).

[21] Y Hardalupas, AMKP Taylor, and JH Wilkins. "Experimental investigation of sub-millimetre droplet impingement on to spherical surfaces". In: *Int. J. Heat Fluid Flow* 20.5 (1999), pp. 477–485.

[22] SA Banitabaei and A Amirfazli. "Droplet impact onto a solid sphere: Effect of wettability and impact velocity". In: *Phys. Fluids* 29.6 (2017), p. 062111.

[23] G Khurana, N Sahoo, and P Dhar. "Phenomenology of droplet collision hydrodynamics on wetting and non-wetting spheres". In: *Phys. Fluids* 31.7 (2019), p. 072003.

[24] G Charalampous and Y Hardalupas. "Collisions of droplets on spherical particles". In: *Phys. Fluids* 29.10 (2017), p. 103305.

[25] J Hendriks et al. "Optimizing cell viability in droplet-based cell deposition". In: *Sci. Rep.* 5.1 (2015), pp. 1–10.

[26] KR Langley and ST Thoroddsen. "Gliding on a layer of air: impact of a large-viscosity drop on a liquid film". In: *J. Fluid Mech.* 878 (2019).

[27] CJ Howland et al. "It's harder to splash on soft solids". In: *Phys. Rev. Lett.* 117.18 (2016), p. 184502.

[28] E Castillo-Orozco et al. "Droplet impact on deep liquid pools: Rayleigh jet to formation of secondary droplets". In: *Phys. Rev. E* 92.5 (2015), p. 053022.

[29] SK Das et al. “Evolution of jets during drop impact on a deep liquid pool”. In: *Phys. Fluids* 34.2 (2022), p. 022110.

[30] Z Che and OK Matar. “Impact of droplets on immiscible liquid films”. In: *Soft Matter* 14.9 (2018), pp. 1540–1551.

[31] U Jain et al. “Deep pool water-impacts of viscous oil droplets”. In: *Soft Matter* 15.23 (2019), pp. 4629–4638.

[32] H Lhuissier et al. “Drop fragmentation at impact onto a bath of an immiscible liquid”. In: *Phys. Rev. Lett.* 110.26 (2013), p. 264503.

[33] G Michon, C Josserand, and T Séon. “Jet dynamics post drop impact on a deep pool”. In: *Phys. Rev. Fluids* 2.2 (2017), p. 023601.

[34] V Lherm et al. “Rayleigh–Taylor instability in impact cratering experiments”. In: *J. Fluid Mech.* 937 (2022).

[35] C Josserand and S Zaleski. “Droplet splashing on a thin liquid film”. In: *Phys. Fluids* 15.6 (2003), pp. 1650–1657.

[36] HM Kittel, IV Roisman, and C Tropea. “Splash of a drop impacting onto a solid substrate wetted by a thin film of another liquidT”. In: *Phys. Rev. Fluids* 3.7 (2018), p. 073601.

[37] W Wang et al. “Formation of water in oil in water particles by drop impact on an oil layer”. In: *Phys. Fluids* 31.3 (2019), p. 037107.

[38] D Kim et al. “The impact of an oil droplet on an oil layer on water”. In: *J. Fluid Mech.* 906 (2021).

[39] X Zhang, C Wang, and S Rui. “Phenomena of single water droplet impacting a heptane layer on water pool”. In: *Eur. J. Mech. B/* 92 (2022), pp. 65–74.

[40] HM Kittel, IV Roisman, and C Tropea. “Splash of a drop impacting onto a solid substrate wetted by a thin film of another liquid”. In: *Phys. Rev. Fluids* 3.7 (2018), p. 073601.

[41] F Marcotte et al. “Ejecta, corolla, and splashes from drop impacts on viscous fluids”. In: *Phys. Rev. Lett.* 122.1 (2019), p. 014501.

[42] S Shaikh et al. “Immiscible impact dynamics of droplets onto millimetric films”. In: *Exp. Fluids* 59.1 (2018), pp. 1–12.

[43] F Yeganehdoust et al. “A numerical analysis of air entrapment during droplet impact on an immiscible liquid film”. In: *Int. J. Multiph. Flow* 124 (2020), p. 103175.

[44] YA Semenov, GX Wu, and AA Korobkin. “Impact of liquids with different densities”. In: *J. Fluid Mech.* 766 (2015), pp. 5–27.

[45] M-J Thoraval et al. “Drop impact entrapment of bubble rings”. In: *J. Fluid Mech.* 724 (2013), pp. 234–258.

[46] T Tran et al. “Air entrainment during impact of droplets on liquid surfaces”. In: *J. Fluid Mech.* 726 (2013).

[47] Z Jian et al. “To Split or Not to Split: Dynamics of an Air Disk Formed under a Drop Impacting on a Pool”. In: *Phys. Rev. Lett.* 124.18 (2020), p. 184501.

[48] D Roy, SS Rao, and S Basu. “Droplet impact on immiscible liquid pool: Multi-scale dynamics of entrapped air cushion at short timescales”. In: *Phy. Fluids* 34.5 (2022), p. 052004.

[49] M-J Thoraval et al. “von Kármán vortex street within an impacting drop”. In: *Phys. Rev. Lett.* 108.26 (2012), p. 264506.

[50] AA Castrejón-Pita, JR Castrejón-Pita, and IM Hutchings. “Experimental observation of von Kármán vortices during drop impact”. In: *Phys. Rev. E.* 86.4 (2012), p. 045301.

[51] X Tang et al. “Bouncing-to-merging transition in drop impact on liquid film: Role of liquid viscosity”. In: *Langmuir* 34.8 (2018), pp. 2654–2662.

[52] MHW Hendrix et al. “Universal mechanism for air entrainment during liquid impact”. In: *J. Fluid Mech.* 789 (2016), pp. 708–725.

[53] KR Langley, AA Castrejón-Pita, and ST Thoroddsen. “Droplet impacts onto soft solids entrap more air”. In: *Soft Matter* 16.24 (2020), pp. 5702–5710.

[54] G Riboux and JM Gordillo. “Experiments of drops impacting a smooth solid surface: a model of the critical impact speed for drop splashing”. In: *Phys. Rev. Lett.* 113.2 (2014), p. 024507.

[55] ST Thoroddsen et al. “Droplet splashing by a slingshot mechanism”. In: *Phys. Rev. Lett.* 106.3 (2011), p. 034501.

[56] AL Yarin et al. “Drop impact dynamics: splashing, spreading, receding, bouncing”. In: *Annu. Rev. Fluid Mech.* 38.1 (2006), pp. 159–192.

[57] JC Bird, SSH Tsai, and HA Stone. “Inclined to splash: triggering and inhibiting a splash with tangential velocity”. In: *New J. Phys.* 11.6 (2009), p. 063017.

[58] J Hao et al. “Droplet splashing on an inclined surface”. In: *Phys. Rev. Lett.* 122.5 (2019), p. 054501.

[59] CHR Mundo, M Sommerfeld, and C Tropea. “Droplet-wall collisions: experimental studies of the deformation and breakup process”. In: *Int. J. Multiph. Flow* 21.2 (1995), pp. 151–173.

[60] F Gao et al. “Weakly charged droplets fundamentally change impact dynamics on flat surfaces”. In: *Soft Matter* 15.28 (2019), pp. 5548–5553.

[61] EJ Vega and AA Castrejón-Pita. “Suppressing prompt splash with polymer additives”. In: *Exp. Fluids* 58.5 (2017), pp. 1–8.

[62] MA Quetzeri-Santiago et al. “Role of the dynamic contact angle on splashing”. In: *Phys. Rev. Lett.* 122.22 (2019), p. 228001.

[63] S Bakshi, IV Roisman, and C Tropea. “Investigations on the impact of a drop onto a small spherical target”. In: *Phys. Fluids* 19.3 (2007), p. 032102.

[64] A Bordbar et al. “Maximum spreading and rebound of a droplet impacting onto a spherical surface at low Weber numbers”. In: *Langmuir* 34.17 (2018), pp. 5149–5158.

[65] D Khojasteh et al. “Curvature effect on droplet impacting onto hydrophobic and superhydrophobic spheres”. In: *Int. J. Comput. Fluid Dyn.* 31.6-8 (2017), pp. 310–323.

[66] X Liu, X Zhang, and J Min. “Maximum spreading of droplets impacting spherical surfaces”. In: *Phys. Fluids* 31.9 (2019), p. 092102.

[67] S Chen and V Bertola. “Drop impact on spherical soft surfaces”. In: *Phys. Fluids* 29.8 (2017), p. 082106.

[68] L Xu, WW Zhang, and SR Nagel. “Drop splashing on a dry smooth surface”. In: *Phys. Rev. Lett.* 94.18 (2005), p. 184505.

[69] C Josserand, P Ray, and S Zaleski. “Droplet impact on a thin liquid film: anatomy of the splash”. In: *J. Fluid Mech.* 802 (2016), pp. 775–805.

[70] S Mirjalili and A Mani. “Transitional stages of thin air film entrapment in drop-pool impact events”. In: *J. Fluid Mech.* 901 (2020).

[71] EQ Li, D Beilharz, and ST Thoroddsen. “Vortex-induced buckling of a viscous drop impacting a pool”. In: *Phys. Rev. Fluids* 2.7 (2017), p. 073602.

[72] M-J Thoraval et al. “von Kármán vortex street within an impacting drop”. In: *Phys. Rev. Lett.* 108.26 (2012), p. 264506.

[73] G Michon, C Josserand, and T Séon. “Jet dynamics post drop impact on a deep pool”. In: *Phys. Rev. Fluids* 2.2 (2017), p. 023601.

[74] E Nowak et al. “Bulk advection and interfacial flows in the binary coalescence of surfactant-laden and surfactant-free drops”. In: *Soft Matter* 13.26 (2017), pp. 4616–4628.

[75] ÁM Soto et al. “Coalescence of diffusively growing gas bubbles”. In: *J. Fluid Mech.* 846 (2018), pp. 143–165.

[76] C Lai, J Eggers, and L Deike. "Bubble bursting: Universal cavity and jet profiles". In: *Phys. Rev. Lett.* 121.14 (2018), p. 144501.

[77] AM Gañán-Calvo et al. "The natural breakup length of a steady capillary jet: Application to serial femtosecond crystallography". In: *Crystals* 11.8 (2021), p. 990.

[78] D Fuster et al. "Numerical simulation of droplets, bubbles and waves: state of the art". In: *Fluid Dyn. Res.* 41.6 (2009), p. 065001.

[79] R Scardovelli and S Zaleski. "Direct numerical simulation of free-surface and interfacial flow". In: *Annu. Rev. Fluid Mech.* 31.1 (1999), pp. 567–603.

[80] G Tryggvason, R Scardovelli, and S Zaleski. *Direct numerical simulations of gas–liquid multiphase flows*. Cambridge university press, 2011.

[81] X Yin et al. "Direct simulations of two-phase flow experiments of different geometry complexities using Volume-of-Fluid (VOF) method". In: *Chem. Eng. Sci.* 195 (2019), pp. 820–827.

[82] M Pietropaoli, F Montomoli, and A Gaymann. "Three-dimensional fluid topology optimization for heat transfer". In: *Struct. Multidiscip. Optim.* 59.3 (2019), pp. 801–812.

[83] FH Harlow and JE Welch. "Numerical calculation of time-dependent viscous incompressible flow of fluid with free surface". In: *Phys. Fluids* 8.12 (1965), pp. 2182–2189.

[84] S Popinet and S Zaleski. "A front-tracking algorithm for accurate representation of surface tension". In: *Int. J. Numer. Methods Fluids* 30.6 (1999), pp. 775–793.

[85] S Osher and JA Sethian. "Fronts propagating with curvature-dependent speed: Algorithms based on Hamilton-Jacobi formulations". In: *J. Comput. Phys.* 79.1 (1988), pp. 12–49.

[86] F Gibou, R Fedkiw, and S Osher. "A review of level-set methods and some recent applications". In: *J. Comput. Phys.* 353 (2018), pp. 82–109.

[87] S Mirjalili, SS Jain, and M Dodd. "Interface-capturing methods for two-phase flows: An overview and recent developments". In: *Center for Turbulence Research Annual Research Briefs* 2017.117-135 (2017), p. 13.

[88] S Popinet. *Basilisk*. `http://basilisk.fr`. Accessed: 2019-02-25. 2019.

[89] S Popinet. "Gerris: a tree-based adaptive solver for the incompressible Euler equations in complex geometries". In: *J. Comput. Phys.* 190.2 (2003), pp. 572–600.

[90] S Popinet. "An accurate adaptive solver for surface-tension-driven interfacial flows". In: *J. Comput. Phys.* 228.16 (2009), pp. 5838–5866.

[91] S Popinet. *Basilisk*. `http://basilisk.fr/Bibliography`. Accessed: 2023-01-05. 2023.

[92] S Popinet. "Numerical models of surface tension". In: *Annu. Rev. Fluid Mech.* 50 (2018), pp. 49–75.

[93] E Aulisa et al. "Interface reconstruction with least-squares fit and split advection in three-dimensional Cartesian geometry". In: *J. Comput. Phys.* 225.2 (2007), pp. 2301–2319.

[94] R Scardovelli and S Zaleski. "Analytical relations connecting linear interfaces and volume fractions in rectangular grids". In: *J. Comput. Phys.* 164.1 (2000), pp. 228–237.

[95] JA van Hooft et al. "Towards adaptive grids for atmospheric boundary-layer simulations". In: *Bound.-Layer Meteorol.* 167.3 (2018), pp. 421–443.

[96] JA Van Hooft. *The_Tree-Grid_Structure_in_Basilisk*. `http://basilisk.fr/sandbox/Antoonvh/The_Tree-Grid_Structure_in_Basilisk`. Accessed: 2023-01-04. 2023.

[97] JA Van Hooft. *The_adaptive_wavelet_algirthm*. `http://basilisk.fr/sandbox/Antoonvh/The_adaptive_wavelet_algirthm`. Accessed: 2023-01-04. 2023.

[98] JA van Hooft. "Modeling the atmospheric diurnal cycle". In: (2020).

[99] C Pairetti. *adapt_wavelet_limited.h*. `http://basilisk.fr/sandbox/pairetti/bag_mode/adapt_wavelet_limited.h`. Accessed: 2019-07-21. 2023.

[100] H Chizari. *Basilisk Three Phase*. `http://basilisk.fr/sandbox/chizari/threephase/`. Accessed: 2022-12-21. 2022.

[101] P-A Maës. *Basilisk Three-Phase*. `http://basilisk.fr/sandbox/maes/Three-Phase/`. Accessed: 2022-12-21. 2022.

[102] V Sanjay. *Basilisk Three Phase*. `http://basilisk.fr/sandbox/vatsal/ThreePhase/`. Accessed: 2022-12-21. 2022.

[103] B Wang et al. "Spreading and penetration of a micro-sized water droplet impacting onto oil layers". In: *Phys. Fluids* 32.1 (2020), p. 012003.

[104] CG Lyons. "LXXXIII.—The angles of floating lenses". In: *J. Chem. Soc.* (1930), pp. 623–634.

[105] PD Ravazzoli et al. "Buoyancy and capillary effects on floating liquid lenses". In: *Phys. Rev. Fluids* 5.7 (2020), p. 073604.

[106] S Popinet. *Basilisk sessile.c*. `http://basilisk.fr/src/test/sessile.c`. Accessed: 2022-12-22. 2022.

[107] SG Jennings. "The mean free path in air". In: *Journal of Aerosol Science* 19.2 (1988), pp. 159–166.

[108] J de Ruiter et al. "Dynamics of collapse of air films in drop impact". In: *Physical review letters* 108.7 (2012), p. 074505.

[109] MV Chubynsky et al. "Bouncing off the walls: the influence of gas-kinetic and van der Waals effects in drop impact". In: *Physical Review Letters* 124.8 (2020), p. 084501.